ANALYSIS OF HYPERSONIC VEHICLE WAKES

THESIS

Matthew A. Kania, Lieutenant, USN
AFIT-ENY-15-S-063

DEPARTMENT OF THE AIR FORCE
AIR UNIVERSITY

AIR FORCE INSTITUTE OF TECHNOLOGY

Wright-Patterson Air Force Base, Ohio

AFIT-ENY-15-S-063

ANALYSIS OF HYPERSONIC VEHICLE WAKES

THESIS

Presented to the Faculty

Department of Aeronautics and Astronautics

Graduate School of Engineering and Management

Air Force Institute of Technology

Air University

Air Education and Training Command

In Partial Fulfillment of the Requirements for the

Degree of Master of Science in Aeronautical Engineering

Matthew A. Kania, BS

Lieutenant, USN

September 2015

AFIT-ENY-15-S-063

ANALYSIS OF HYPERSONIC VEHICLE WAKES

Matthew A. Kania, BS
Lieutenant, USN

Committee Membership:

Dr. Robert Greendyke, PhD
Chair

Lt Col Richard Huffman, PhD
Member

Capt Brook Bentley, PhD
Member

AFIT-ENY-15-S-063

Abstract

As advancements are made with ballistic missiles, particularly in the area of hypersonic bodies, there is a growing need to advance the methods of detecting these new ballistic weapons. As a result, the National Air and Space Intelligence Center has asked the Air Force Institute of Technology to examine the wake region behind hypersonic bodies. A thorough understanding of the aerothermal phenomena and the chemical reactions occurring in the wake region will enable an advancement of tracking hypersonic bodies. This research examined the wake region behind a hypersonic body using computational fluid dynamics.

This study used Pointwise® to develop a three-dimensional grid of the flowfield around a conic hypersonic body and extending into the wake region. The Langley Aerothermodynamic Upwind Relaxation Algorithm was used to solve the flowfield, including the wake, and all surface properties. The results from the simulation were used to characterize the wake region behind the hypersonic body and compare that to the flowfield surrounding the body.

Although no flight test data was available and no published results could be found in this area of interest, the results had good agreement with expected results. Along with that, several interesting phenomena were discovered dealing with the aerothermal environment and chemical species present in the wake that could lead to advancements in the efforts of tracking hypersonic bodies.

Acknowledgments

Table of Contents

List of Figures

List of Tables

List of Abbreviations

BMD	Ballistic Missile Defenses
CFD	Computational Fluid Dynamics
ICBM	Intercontinental Ballistic Missile
LAURA	Langley Aerothermodynamic Upwind Relaxation Algorithm
MaRV	Maneuvering Re-entry Vehicle
MIRV	Multiple Independently-Targetable Re-entry Vehicle
NASA	National Aeronautics and Space Agency
RV	Re-Entry Vehicle
WMD	Weapon of Mass Destruction

Nomenclature

a_l', b_l'	geometric weighting parameters
A	Jacobian matrix of $\mathbf{f}$ with respect to $\mathbf{q}$
B	Jacobian matrix of $\vec{h}$ with respect to $\vec{q}$
c_p	specific heat, constant pressure
c_v	specific heat, constant volume
c	speed of sound
E	total energy per unit mass of mixture
D_s	effective diffusion coefficient for species s
e_V	mixture vibrational-electron energy per unit mass
f	frequency
$\vec{f}$	vector of conserved variables
$\vec{g}$	inviscid component of flux vector relative to cell face
$\vec{h}$	viscous component of flux vector relative to cell face
h_s	enthalpy per unit mass of species s
$h_{v,s}$	vibrational-electronic energy per unit mass of species s
H	total enthalpy per unit mass of mixture
I	Identity matrix
Kn	Knudsen number
L	characteristic length
M	mach number
M_L	point-implicit Jacobian of flux terms
$M_{L,INV}$	point-implicit Jacobian of inviscid terms
$M_{L,SRC}$	point-implicit Jacobian of source terms
$M_{L,VIS}$	point-implicit Jacobian of viscous terms
N	iteration index level
$\vec{n}$	unit normal vector
n_x, n_y, n_z	components of $\vec{n}$ in x, y, z directions respectively
P	pressure
$\vec{q}$	vector of conserved variables
Q_{rad}	radiative energy transfer rate
$\vec{r}$	right-hand-side of residual vector
rf_{inv}	relaxation factor used with inviscid Jacobian
rf_{vis}	relaxation factor used with viscous Jacobian
R_l	matrix of left eigenvectors for A
R	specific gas constant
Re	Reynolds number
Re_{cell}	cell Reynolds number
$\dot{s}$	dummy variable for u, v, w corresponding to s= x, y, z
s_n, s_l, s_m	arc lengths in n, l, m directions
$\vec{s_l}$	approximation to gradient of characteristic variables across cell face
$\vec{s}_l^{min}$	approximation to gradient of characteristic variables across cell face
S	dummy variable for x, y, z

St	Strouhal number
T	temperature
T_v	vibrational-electron-electronic excitation temperature
t	time
u,v,w	velocity component in x, y, z direction
U, V, W	velocity component in n, l, m direction
Vel	velocity
$\dot{w}_s$	mass production rate of species s per unit volume
$\dot{w}_v$	vibrational-electronic energy source term
y_s	mole fraction of species s
Δn	radial cell spacing
γ	specific heat ratio
δ	deflection angle
η	frozen thermal conductivity for translational and rotational heavy particles
η_s	frozen thermal conductivity for vibrational and electronic energy
θ	shock wave angle
θ_f	0 for first-order, 1 for second-order approximation to inviscid flux
λ	mean free path
λ	kinematic viscosity
Λ_l	diagonal matrix of eigenvalues for A
$\boldsymbol{\mu}$	dynamic viscosity
ξ, η, ζ	computational coordinates in the longitudinal, circumferential, and normal directions
ρ	density
σ	cell face area
τ	shear stress
χ	dummy variable for $\xi, \eta,$ or ζ
$\vec{\omega}$	vector of source terms
Ω	cell volume

Subscripts

i, j, k	indices of cell walls in the ξ, η, ζ directions
I, J, K	indices of cell centers in the ξ, η, ζ directions
l	dummy index for a cell wall
L	dummy index for a cell center
s	species s
V	vibrational-electronic
w	Value at the wall surface
x, y, z	x, y, z direction
∞	Value at freestream conditions

Superscript

*	latest available value at neighbor cell L-1

ANALYSIS OF HYPERSONIC VEHICLE WAKE

I.   Introduction

1.1. Chapter Overview

The following chapter will review the history of ballistic missiles along with touch on the current state of them throughout the world. Ballistic missile flight characteristics and their importance to tracking and engaging them will also be addressed. Finally, recent advancements in missile technology, how these advancements affect traditional defenses and the goals of this research will be addressed.

1.2. History of Ballistic Missiles

Powered missile flight for warfare was first recorded at the siege of Kaifeng in 1232 when rockets were used to set fire to tents and fortifications. The advancement of ballistic missiles was a slow process, but in 1807 the British Navy developed and deployed iron rockets. These iron rockets were used to decimate Copenhagen and a large French fleet during a British naval attack in the Battle of Copenhagen. Even the United States' national anthem makes reference to use of missiles when Francis Scott Key wrote the lyrics "by the rocket's red glare," which was in reference to how he was able to see the American flag [1].

While these are all examples of early ballistic missiles they are not true representations of a ballistic missile. Oxford Dictionaries defines a ballistic missile as "A missile with a high, arching trajectory, that is initially powered and guided but falls under gravity onto its target [2]." Using this definition the first development of ballistic missiles was in the 1930s by the Germans and research efforts increased during World War II. This German research led to the production of the Vergeltsungswaffe Ein and Zwei

(Revenge Weapons One and Two) or more commonly known as V-1 and V-2. The V-2 was the more technologically advanced of the two missiles and flew a more traditional ballistic profile. The V-2 was capable of reaching an altitude of 50-60 miles, had a maximum range of 200 miles, and could carry a one-ton warhead with an accuracy of 2.5 miles [3].

As advancements in technology were made, the cost of ballistic missiles was reduced while the capability increased. This reduction in cost made these weapon systems more attractive to countries around the world. In the last thirty years, ballistic missiles have been used in various conflicts including the Iran-Iraq war, Afghan civil war, the war in Yemen, both Persian Gulf conflicts, and the Russian military action in Chechnya and Georgia [4]. Ballistic missiles enable countries to attack adversaries with robust air defenses without the risk of using manned aircraft. Other advantages include lower maintenance, training, and logistic requirements than manned aircraft. These advantages, coupled with the reduced cost, made these weapons a shocking threat particularly when paired with warheads of mass destruction; chemical, biological, and nuclear. There are now over twenty countries that have ballistic missile systems that continue to evolve and may prove to be a threat to the United States [4].

1.3. Traditional Ballistic Missile Characteristics

Ballistic missiles are deployed throughout the world using a variety of methods including silos, submarines, and on land-mobile launchers. These missiles can range from ten to thirty meters tall and are powered by either a liquid or solid propellant. Using either of these propellants, ballistic missiles can reach top speeds of 24,000 kilometers per hour, altitudes of 1,300 kilometers, and ranges of over 5,500 kilometers [5]. Modern

ballistic missiles with inertial guidance systems are capable of delivering a warhead within a few hundred meters of a target after a flight of over 5,500 kilometers. These warheads, which include a standard explosive and weapons of mass destruction (WMDs), can be installed in two different re-entry vehicles (RVs). These RVs are multiple independently-targetable re-entry vehicles (MIRVs) and maneuvering re-entry vehicles (MaRVs). A MIRV can release its payload at different points during the missiles flight, engaging multiples targets separated by over 1,500 kilometers. MaRVs are able to alter their flight path using terminal sensors to increase the accuracy of the RV [4].

For these RVs to be successful, a traditional ballistic missile must fly a specific flight path. This flight path consists of a boost phase, midcourse phase, and a terminal phase. The total flight time for an Intercontinental Ballistic Missile (ICBM) is about thirty minutes with only five to ten of those minutes being powered flight. Immediately after takeoff the missile enters into a vertical climb. After a short vertical climb the missile is rolled to the target azimuth and pitched toward the target. During this time the missile is accelerated and given all required corrections along its axes by varying which engines are ignited and terminated [3]. This boost phase will propel the missile until it is about 320 kilometers above the earth's surface. At this point the missile is almost out of the earth's atmosphere and continues to accelerate, which concludes the boost phase. The midcourse phase lasts up to twenty minutes in which the missile continues to climb to an altitude of almost 1,300 kilometers and accelerates to 24,000 kilometers per hour, under the affects of gravity alone. During this phase, if the RV is an MIRV, it will begin to dispense its warheads. Additionally, if the RV is equipped with decoys they will be employed. At the point when the missile begins to encounter the earth's atmosphere the

midcourse phase ends and the terminal phase begins. This phase lasts roughly five minutes [5]. During the terminal phase the RV is subject to atmospheric drag and aerodynamic heating. Traditional ballistic missiles have no flight control surfaces to change their trajectory during re-entry. This trajectory is determined by three main factors, the range of the target, desired accuracy of the missile and how the RV will dissipate the heat developed from the atmospheric drag. Traditional ballistic missiles improve their accuracy by increasing the angle of their terminal approach. However, increasing the angle of the terminal approach decreases the range and increases the heat developed from drag. These flight parameters cause a three-way tradeoff between range, accuracy, and survivability. The RV can experience speeds upwards of Mach 20 and temperatures in excess of 8,000 degrees Celsius during this phase of flight. As the RV approaches its target, the arming sequence begins. Once the warhead is armed it will either detonate at a predetermined altitude or impact its ground based target. Figure 1 depicts the typical flight path of a ballistic missile.
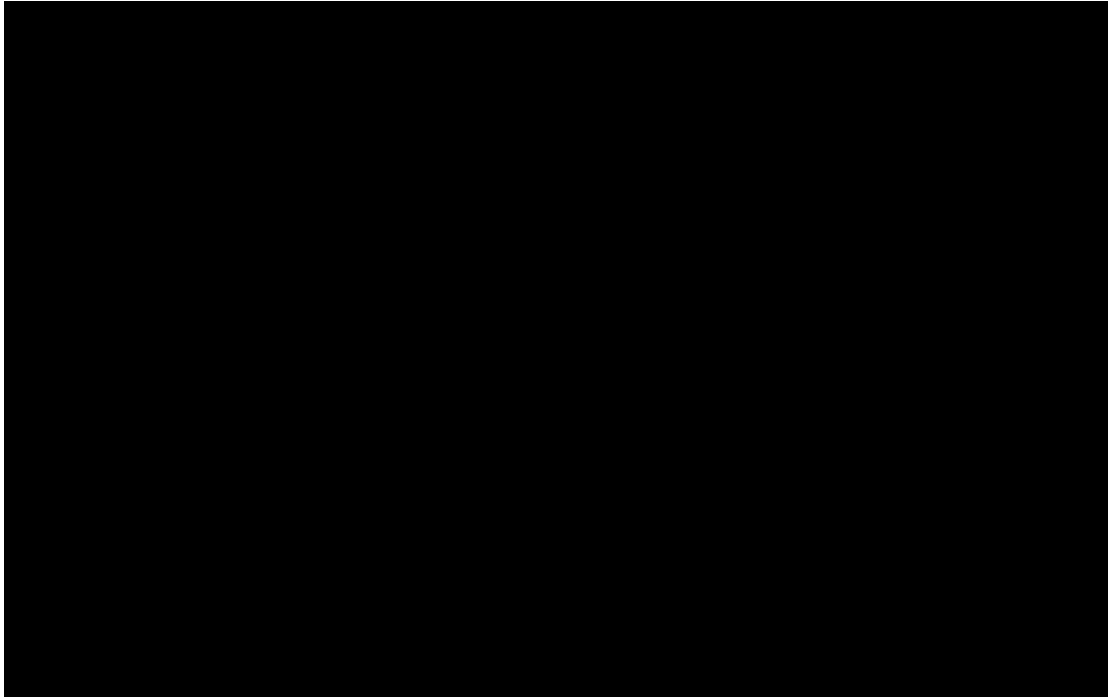
Figure 1. Typical Ballistic Missile Flight Path (based on Gibson)

1.4. Traditional Ballistic Missile Defenses

Ballistic missile defenses (BMDs) have been in development since World War II but their first combat test was during the 1991 Gulf War. The United States BMDs, at the time and currently in development, are designed to strike a ballistic missile after thrust termination, during the midcourse or re-entry phases, between 40-100 kilometers above the earth's surface. These exoatmospheric BMDs can engage any missile that leaves the earth's atmosphere, which is how all long range ballistic missiles are designed to operate. BMDs search for and detect the targets using radar systems, once the target is detected a flight path for the missile is determined and the ballistic missile is engaged [6].

The radar systems that detect ballistic missiles are required to be able to detect the targets at an incredibly far distance. Radar systems must be able to search for, track, and illuminate targets very quickly to ensure that targets are not missed between area scans.

To accomplish this, a search must be conducted in all directions from which a missile could approach and must be repeated often. After a target is detected, the radar system will track and illuminate the target. This radar system allows the BMD to increase its certainty of the targets trajectory. Due to the large amount of space that BMD radars must search, all defense systems use external sensors to aid the radar. These sensors help with the detection of ballistic missiles by determining a launch location and are known as cueing sensors. Cueing sensors can include forward deployed radar systems or early warning satellites [6]. Determining a launch location helps to narrow the search area for the missile and assists in determining the azimuth that of missile arrival. Once the missile is being tracked, a firing solution is calculated so the BMDs will engage the missile during the exoatmospheric portion of its flight. The missiles are engaged during this portion of the flight for two reasons: the threat missile's flight path can be predicted; and the path is unchanging. Attacking the threat missile at this point gives the BMDs the greatest chance of success [6].

1.5. Research Objectives

In recent years there have been significant advances in technology that improved and changed ballistic missile performance. These changes in performance no longer allow accurate tracking with current ballistic missile defenses. Advancements in materials and missile design have been the primary factors in the changing performance. Ballistic missiles no longer need to follow a traditional re-entry flight path and can follow a boost-glide profile.

Boost-glide profiles allow for the missile to glide in an unpowered state, at hypersonic velocities, at significantly lower altitudes, and greater distances than

6

traditional ballistic missiles. These missiles accomplish the boost portion by using powered flight reaching the desired attitude then falling with a nearly straight down trajectory to build up a massive amount of kinetic energy. As the missile enters a relatively lower altitude it will execute a turn to level out its flight path. After the turn has been made, the missile is now in the glide portion of the flight profile where it uses the kinetic energy from the fall as well as lift produced from its lifting surfaces to travel towards its target.

Boost-glide missiles present a new challenge to our ballistic missile defenses since the defenses are based on tracking missile plumes through a typical ballistic missile flight path. Since boost-glide missiles do not have a plume in during the glide portion of the profile they are very difficult to track. Due to this issue, extensive research is being conducted in tracking hypersonic boost-glide missiles during the glide portion of the flight profile. Currently there is a strong focus on tracking these missiles by using wake phenomena and signatures. Unfortunately, there have not been any significant studies on wake region phenomena since the 1960's. These studies were conducted by the National Aeronautics and Space Agency (NASA) and were focused on the survivability of vehicles returning from outer space. While the NASA studies advanced the knowledge of wake region aerodynamics, they did not focus on any other phenomena or signatures that are present in the wake which could be used for tracking purposes.

This research will focus on characterizing the aerothermal environment in the wake region of a generic hypersonic conic body during the glide portion of a boost-glide flight profile. The first wake region phenomenon that could be used for tracking efforts is vortex shedding. It has been hypothesized that vortex shedding in the wake region could

cause an oscillating signature that could be tracked. In order to verify this hypothesis, a first order approximation of the vortex shedding frequency behind hypersonic cones was needed. The first step in obtaining the approximation was to calculate a Reynolds number for the flight data during the re-entry phase; this data can be seen in Table 1.

<div align="center">

Table 1. Characteristics and Flight Data

Length	3.5 m
Velocity	2,115 m/s
Altitude	30 km
Density	0.01841 kg/m^3
Dynamic Viscosity	1.475*10^{-5} N*s/m^2
Temperature	226.5 K

</div>

Using this data, a Reynolds number of 9.24*10^6 was calculated using Equation (1) where Re is the Reynolds number, ρ is density, Vel is velocity, L is characteristic length, and $\boldsymbol{\mu}$ is dynamic viscosity.

$$Re = \frac{\rho VelL}{\boldsymbol{\mu}}$$ (1)

Due to the lack of research in the area of hypersonic cones, an approximation of a cone was used. J. Novak found that the Strouhal number of a prism is almost independent of the Reynolds number, but is very sensitive to the number of prism edges, sides of the body, and the position in the flow. Novak also discovered that when prisms have ten or more edges, the number of edges became insignificant and they could be modeled as a circular cylinder. This approximation also applies to cones [7].

Knowing that vortex shedding from cones could be approximated with vortex shedding from circular cylinders, data on Strouhal numbers from circular cylinders was required. It was found that Strouhal numbers were relatively constant, 0.25-0.27, for

Reynolds from 10^6 to 10^7. For Reynolds numbers greater than $3.5*10^6$, definite vortex shedding occurs, with a Strouhal number of 0.27 [8]. Since the Reynolds number calculated earlier was above this range, an approximate Strouhal number 0.27 was used.

Armed with the Strouhal number, an approximation of the vortex shedding frequency could finally be calculated using Equation (2) where St is the Strouhal number, f is the frequency of vortex shedding. L and Vel are the same as previously defined.

$$St = \frac{fL}{Vel} \tag{2}$$

The vortex shedding frequency was calculated to be 163 Hz. Since the vortex shedding frequency was so high, it was determined that no significant information could be obtained from tracking this phenomenon.

With the determination that vortex shedding would not be useful in tracking efforts, focus was shifted to characterizing other wake phenomena. The aerothermal phenomena of interest in the wake include: gas properties, chemical species (particularly ionized species), and ablative species. Additionally, aerodynamic phenomena in the wake such as recirculating flow, neck stagnation point, and recompression shocks will be investigated. Gaining an understanding of each of these phenomena will highlight the wake region phenomena that could be used for tracking and concentrating the radiation spectrums where tracking efforts should be focused and is the focus of this research.

II. Literature Review

2.1. Chapter Overview

The following chapter will review hypersonic flow theories in order to gain a solid understanding of the phenomena occurring in this regime. Along, with hypersonic flow, computation fluid dynamics (CFD) and the Langley Aerothermodynamic Upwind Relaxation Algorithm (LAURA) must be understood since they will be the tools used to conduct this research. Finally, an investigation into the aerothermal phenomena occurring in the wake of a hypersonic body must be conducted to obtain the core knowledge needed to examine wake flow.

2.2. Hypersonic Flow

Hypersonic aerodynamics is conventionally defined by flow where the Mach number (M) is greater than 5. This conventional definition however is only a general rule of thumb as opposed to scientific fact. Hypersonic flow, defined by Anderson, is "The regime where certain physical flow phenomena become progressively more important as the Mach number is increased to higher values. [9]" Anderson's definition of hypersonic flow makes it clear that there is no set value for where hypersonic aerodynamics begins. The main reason for there being no set value for the beginning of hypersonic flow is that as M increases the conservation equations cannot be linearized. The flow properties must be modeled in a complex fashion and can no longer be modeled in a linear fashion. Since this can occur at varying Mach numbers, Anderson defines five properties to determine when hypersonic aerodynamics applies. These properties are: thin shock layers; entropy layer; viscous interaction; high-temperature flows; and, low-density flow [9].

In hypersonic flows, the distance between the shock layer and the body can be small. This small distance is due to the fact that density across a shock wave becomes progressively greater as M is increased. With the density of the flow being higher, the same flow must pass through a smaller area, keeping the mass flow rate the same to satisfy conservation equations. This area, between the body and the shock, is known as the shock layer. To estimate the shock layer thickness, standard oblique shock theory can be applied using Equation (3); where θ is the body deflection angle, β is the shock deflection angle, M_1 is the Mach number prior to the shock wave, and γ is the specific heat ratio [10].

$$tan\,\theta = 2\,cot\,\beta \left[\frac{M_1^2 sin^2\beta - 1}{M_1^2(\gamma + cos2\beta) + 2} \right] \tag{3}$$

For example, consider a calorically perfect gas with a specific heat equal to 1.4 with a Mach number of 15 flowing over a 15 degree wedge. Using Equation (3) the shock deflection angle is approximately 18 degrees and is depicted in Figure 2 [9].
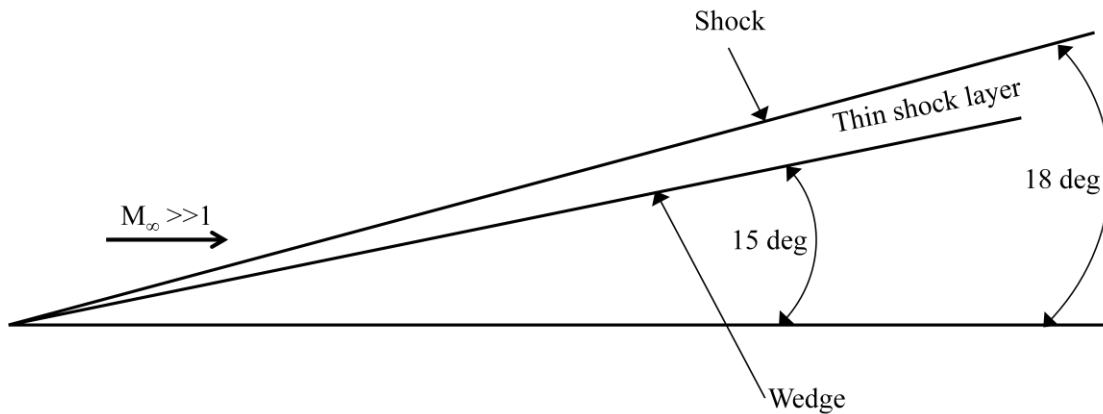
Figure 2. Thin Hypersonic Shock Layer (based on Anderson)

The shock layer will become even thinner when high-temperature, chemically-reacting flows are included. A thin shock layer can create some complications at low Reynolds

11

number flows. At low Reynolds numbers the shock layer and viscous boundary layer will merge. On the other hand, at high Reynolds numbers, the shock layer can be assumed to be inviscid, which leads to an analytic approach called shock-layer theory.

Entropy layers will be created when high Mach number flow passes over a blunt nose object. This entropy layer occurs because the shock over a blunt nose object becomes detached at the nose. The detached shock has a high curvature in the nose region which has carrying effects on the streamlines passing through the shocks. It is important to remember that as flow passes through a shock there is an entropy increase, therefore the stronger the shock the greater the entropy increase. Due to this phenomenon, a streamline that passes through the nearly normal part of the shock will experience a much greater entropy increase than the bordering streamlines. The varying entropies cause a strong entropy gradient to form in the nose region which travels down the entire length of the body. Figure 3 depicts an example of this [9]. Entropy layer are important because of Crocco's Theorem, which states that with a gradient in entropy vorticity will from. This entropy layer creates a problem when analyzing boundary layers due to the boundary layer growing inside of the entropy layer also depicted in Figure 3.
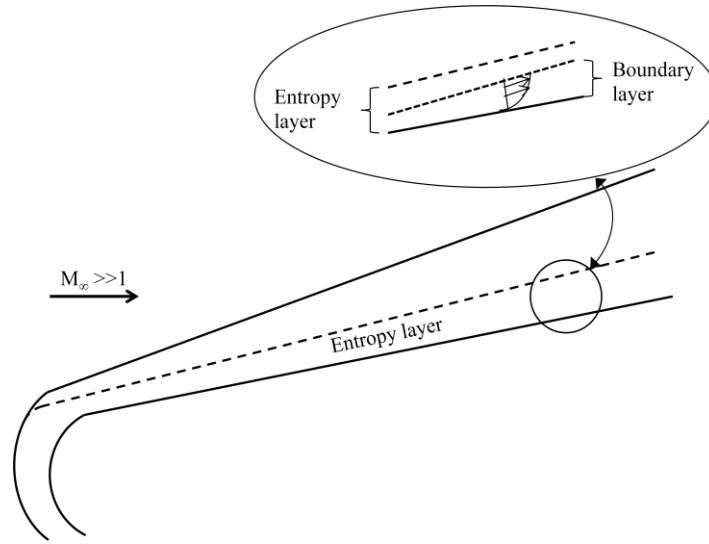
Figure 3. Entropy Layer (based on Anderson)

A body traveling at hypersonic speeds will have these effects on the boundary layer which will cause the inviscid flow outside of the boundary layer to be altered. The changes in the inviscid flow will affect the growth of the boundary layer which is known as viscous interaction. Viscous interactions will affect the lift, drag, stability, skin friction, and heat transfer of the hypersonic vehicle. When high-velocity flows are slowed by viscous effects within the boundary layer, part of the gas's kinetic energy is transformed into internal energy. This transformation of energy is known as viscous dissipation and causes the temperature within the boundary layer to increase. An example of the temperature profile is depicted in Figure 4 [9].
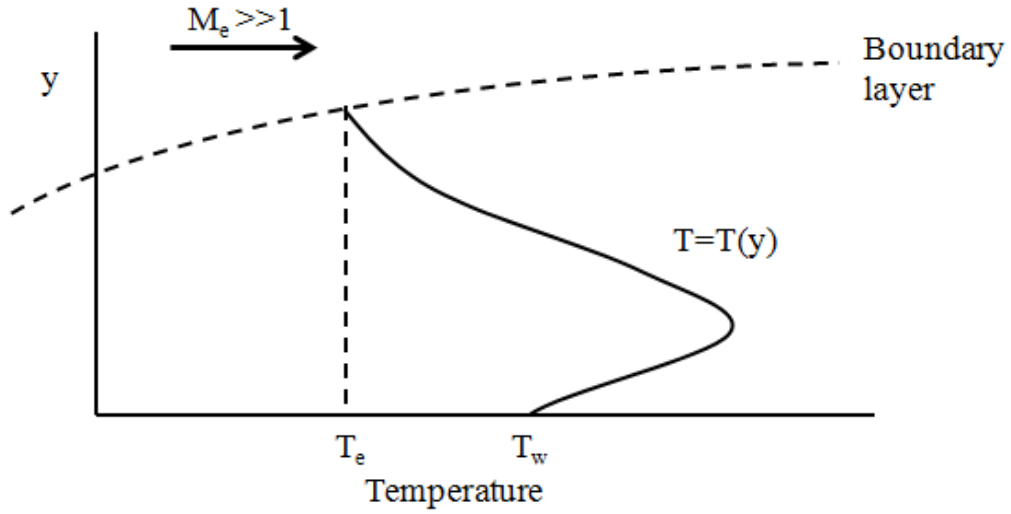
Figure 4. Temperature Profile in a Hypersonic Boundary Layer (based on Anderson)

The temperature increase of the gas drives boundary layer characteristics including the boundary layer thickness and the mass flow rate. Boundary layer thickness increases due to the direct correlation between temperature and viscosity. As the temperature of a gas increases the viscosity increases as well, thus causing the boundary layer thickness to increase. The mass flow rate will increase because of the equation of state, Equation (4), where P is the pressure, ρ is density, R is the specific gas constant, and T is temperature.

$$P = \rho RT \tag{4}$$

Due to the increase in temperature and R being constant, either P or ρ must change to satisfy the equation. Pressure is constant in the body normal direction causing density to decrease. To satisfy the mass flow rate constraints with the reduced density, the boundary layer must grow. Eventually the boundary layer will continue to grow and meet the shock, known as a merged shock layer. When the shock layer is merged, it is treated as fully viscous and conventional boundary layer theory cannot be used [9].

These viscous interactions, especially the viscous dissipation in the boundary layer, will give rise to extremely high temperatures. These high temperatures cause the gas to no longer behave in an ideal fashion. The non-ideal effects present are the vibrational energy of molecules becoming excited and the chemical reaction occurring; these non-ideal effects are known as high-temperature effects. When vibrational energy of molecules becomes excited, the c_p and c_v are no longer constants but functions of temperature. Since c_p and c_v are not constant, γ can no longer be considered a constant and becomes a function of temperature. With a continued increase in temperature, chemical reactions can occur causing gas dissociation and ionization. The chemical reactions cause γ to become a function of temperature and pressure. With an ablative heat shield present there would be products of ablation present to react with as well. These products of ablation, along with the dissociation and ionization of the gas, gives rise to complex hydrocarbon chemical reactions and can be present in the boundary layer or throughout the entire shock layer. If these effects take place very rapidly compared to the time it takes for a fluid element to move through the flowfield, vibrational and chemical equilibrium flow is present. Nonequilibrium flow is exactly the opposite and more information on both can be found in reference. Even though these effects have an influence on the aerodynamic principles of a hypersonic vehicle, the most prevailing effect is a high-heat-transfer rate. Aerodynamic heating occurs in two ways; convective and radiative heating. Convective heating occurs when heat is transferred from a hot boundary layer to the cooler surface. Radiative heating occurs when the temperature in the shock-layer is high enough to have thermal radiation emitted by the gas itself. These

two aspects of aerodynamic heating are so important that they direct the design of all hypersonic vehicles [9].

According to Anderson [9], the final characteristic of a hypersonic flow is low-density flow. However, low-density flows are not a characteristic of hypersonic flows but a possible characteristic of the environment in which a hypersonic vehicle is operating. The Knudsen number, Kn, was developed to determine what type of flow an object is operating in. Equation (5) shows the equation for the Knudsen number, where λ is the mean free path and L is the characteristic length of the object [9].

$$Kn = \lambda/L \tag{5}$$

Almost all aerodynamic applications occur when Kn < 0.1, where a continuum model can be used. In a continuum flow either the Euler or Navier-Stokes equations can be satisfied. When Kn > 0.03 slip effects of velocity and temperature must be taken into account. Velocity slip is when molecules at the surface are no longer at zero velocity but take on a finite value. Temperature slip, which is similar, is when the gas molecules at the surface of the object are no longer the same temperature as the surface itself. As mentioned earlier, both the Euler and Navier-Stokes equations can still be satisfied but the boundary conditions must be changed to reflect these conditions. The slip effects hold from 0.03 < Kn < 1.0, in the regime known as the transition regime. When Kn > 1.0, free molecule regime begins which means the air density is so low that only a few molecules impact the surface per unit time and after they return from the surface they do not interact with incoming molecules. In free molecule flow the conservation equations no longer form a

closed set and the collisionless Boltzmann equations can be used to sovle free molecule flow conditions.

Of the five characteristics discussed, the most important is high-temperature flows. High temperatures determine the gas species that must be analyzed in the flow along with several of the models that must be used including surface temperature and catalysis models. These models will have a direct effect on the aerothermal phenomena around the body and in the wake region.

Since hypersonic wind tunnels are not readily available to complete this research, another research tool needed to be utilized. CFD will provide the means to study the vortex shedding of a hypersonic cone and the recompression shock that forms in the body's wake.

2.3. Computational Fluid Dynamics

Computational fluid dynamics is a relatively new approach to studying fluid dynamics. CFD as defined by Peter Gnoffo is "The numerical simulation of flowfields through the approximate solution of the governing partial differential equations for mass, momentum, and energy conservation coupled with the appropriate relations for thermodynamic and transport properties [11]." Historically fluid dynamics was only studied through experimentation and a theoretical understanding of the fluid dynamics. As a result, most of the research that was conducted in the twentieth century was either pure theory or pure experimentation. This research, however, has been changed due to advancements in computers and the development of numerical algorithms for solving physical problems. These algorithms combined with the advancements in computers led to what is commonly known as CFD. CFD is a third approach to studying fluid dynamics

17

but it will never replace pure theory or experimentation; only act as a complement to them [12].

CFD applications are based in fluid dynamics theory and the results are directly analogous to experimental (wind tunnel, water channel, etc.) results. These CFD applications are essentially experiments themselves except they are not physical experiments but numerical experiments performed with a computer program. These numerical experiments allow the study of phenomena and details that are impossible to obtain in a traditional laboratory experiment. However, if a laboratory experiment can be carried out in parallel with a numerical experiment, the results from the numerical experiment can be used to help interpret the physical results [12].

As stated earlier, CFD is governed by three fundamental principles; conservation of mass, momentum, and energy. These fundamental principles can be expressed as mathematical equations that are partial differential equations [12]. In order to solve these equations the partial differential equations must be replaced with discretized algebraic forms. These algebraic equations are then solved to obtain numbers for the flowfield at discrete points-in-time and/or space. These calculated numbers define the flowfield. This process is in contrast to a closed-form analytical solution obtained from a pure theory approach. At first glance, this may seem to be less desirable than obtaining a closed-form solution. However, Anderson points out that "the objective of most engineering analyses, closed form or otherwise, is a quantitative description of the problem, i.e., numbers" [12].

Not all CFD programs can handle the high computational demand of running a simulation with hypersonic flows. Due to this issue, a program that has developed

accurate results in the past was necessary. LAURA, a program developed by NASA, was chosen as the CFD program for all aerothermodynamic flowfield analysis.

2.4. Hypersonic Applications of Computational Fluid Dynamics and LAURA

Aerothermodynamics is a branch of fluid dynamics that concentrates on aerodynamics and heating; specifically from the effects of thermodynamics and transport models. Aerothermodynamics focuses on the study of hypersonic velocities where calorically perfect gas assumptions are no longer valid. Computational aerothermodynamics is a branch of CFD that focuses specifically on high temperature gas effects on pressure, skin friction, and heat transfer [11].

In order for a solution of the flowfield to be found, the flowfield must be divided into many smaller domains called control volumes. The size and orientation of these control volumes has a direct correlation to the accuracy of the solution. In an ideal situation, the smaller the control volume the more accurate the solution will be. However, since truncation and round-off errors can occur, this is not always the case. The control volume boundaries need to be correctly oriented to various flow features, including but not limited to shocks, boundary layers, shear layers, and expansions. Having a CFD program that will orient a grid with an evolving flowfield is extremely helpful in developing an accurate solution but significantly complicates the program and algorithms needed to solve the flowfield. For example, programs that can adapt control volumes for a shock layer and a boundary layer will be able to accurately solve the entropy across a shock, which will feed the conditions to the boundary layer edge. If there are any inaccuracies in the shock, these will propagate through the rest of the flowfield resulting in a highly inaccurate solution. One program that has been proven to have significant

accuracy in computational aerothermodynamics with grid adaptation is the Langley Aerothermodynamic Upwind Relaxation Algorithm (LAURA).

"The LAURA code is a three-dimensional, finite volume, thin-layer Navier-Stokes solver developed by Gnoffo [13]." Upwind differencing of the discredited equations is used in a second-order-accurate symmetric total variation diminishing scheme and Roe's averaging is utilized to define variables at the cell walls. Global sweeps through the computational domain relax the discretized equations. These relaxed equations allow the dependent variables at a cell's center to be taken care of implicitly. The adjacent cell variables are treated explicitly using the most up to date information. The LAURA code focuses on external hypersonic flow simulations and is entirely based on the object's geometry. Focusing on an object's geometry allows the code to be applied to a variety of shapes and applications [13]. LAURA has provided aerothermodynamic analysis on a variety of aerospace vehicles including the Aeroassist Flight Experiment, the HL-20, the Shuttle Orbiter, the Mars Pathfinder, the Single-Stage-to-Orbit vehicle, the X-33 and the X-34 [14]. Since LAURA has proven itself as a reliable tool for analyzing external hypersonic flows, it is an ideal choice for the scope of this research.

One of the features that make LAURA ideal for this research is its inherent structured grid adaptation tool. LAURA moves a structured grid in a quasi-one-dimension adaptation to capture the bow shock, control boundary layer grid size, and grid stretching factors to obtain grid-converged heating rates [11]. The grid adaptation is done in the body normal direction and performed during the relation sweeps. Simulations are usually started with one-fourth of the desired final number of cells in the normal direction. Cell doubling in the normal direction is performed by LAURA during

relaxation sweeps. By following this practice, stability of the solution and probability of convergence are increased [13]. Thompson and Gnoffo found that the accuracy of the LAURA solution was relative to the Reynolds number of the cells at the wall, see Equation (6).

$$Re_{cell} = \frac{\rho_w c_w \Delta n}{\mu_w} \tag{6}$$

They conducted a study on a fifteen degree sphere cone, using two different nose radii. Three different grid spacings were used that corresponded to a Re_{cell}=2, 20, and 200 and there were 64 cells in the normal direction with a grid stretching factor of 1.2 for each case. All three cases were compared to experimental data. As expected, the largest grid spacing of Re_{cell}=200 produced the worst results with Re_{cell}=20 producing significantly better results. Re_{cell}=2 produced the best results that very closely agreed with the experimental data. The refinement to Re_{cell}=2 had only a slight increase in accuracy in heating differences over Re_{cell}=20 [13]. From this research it was shown that a Re_{cell} at the surface of a hypersonic body should be on the order of magnitude of ten to produce accurate heating results in the boundary layer.

LAURA solves the flowfield and thus each individual cell by using an upwind-biased, point-implicit relaxation algorithm. This algorithm achieves the solution to the governing equations for viscous, hypersonic flows in chemical and thermal non-equilibrium. The LAURA algorithm was derived using a finite-volume formulation where modified Roe's averaging and Harten's entropy fix, with second-order corrections, are used for the inviscid components of flux across a cell boundary. The algorithm remains stable for large Courant numbers due to the point-implicit relaxation. Stability is

maintained by the relaxation factors along with the inviscid contribution to the flux Jacobian, which enhances stability for the second-order-accurate implementation of the algorithm [15].

To solve the conservation laws for an individual cell, LAURA uses a finite-volume approach. Equation (7) is the integral form of the conservation laws for a single cell in the flowfield. The first term represents the time rate of change of a conserved quantity through the control volume, the second term represents the flux through cell walls, and the third term is for all the sources and sinks of the conserved quantities throughout the control volume. For a rectangularly ordered structured grid, the finite-volume approximation of Equation (7) is shown by Equation (8). All equations for the rest of this section will be for rectangularly ordered, structured grids. In Equations (7) and (8) $\vec{q}$ represents vector of conserved variables, t is time, Ω is the cell volume, $\vec{f}$ is the convective and dissipative flux through cells walls, $\vec{n}$ is the unit vector normal to computational cell wall, σ is the cell face area and $\vec{\omega}$ is the vector of source terms. The uppercase I, J, K, and L variables represent computational coordinates at cell centers and the lower case i, j, k, and l represent cell faces and cell corners [15].

$$\iiint \frac{\partial \vec{q}}{\partial t} d\Omega + \iint \vec{f} * \vec{n} d\sigma = \iiint \vec{\omega} \partial\Omega \tag{7}$$

$$\begin{aligned}
\left[\frac{\delta\vec{q}\Omega}{\delta t}\right]_{I,J,K} &+ \left[\vec{f}_{i+1} * \vec{n}_{i+1}\sigma_{i+1} - \vec{f}_i * \vec{n}_i\sigma_i\right]_{J,K} \\
&+ \left[\vec{f}_{j+1} * \vec{n}_{j+1}\sigma_{j+1} - \vec{f}_j * \vec{n}_j\sigma_j\right]_{I,K} \\
+ \left[\vec{f}_{k+1} * \vec{n}_{k+1}\sigma_{k+1} - \vec{f}_k * \vec{n}_k\sigma_k\right]_{I,J} &= \left[\vec{\omega}\partial\Omega\right]_{I,J,K}
\end{aligned} \tag{8}$$

With the conservation equation defined for a finite volume it is convenient to separate the inviscid, viscous, and source terms. Separating the inviscid and viscous terms is shown by Equation (9) where $\vec{g}_l$ and $\vec{h}_l$ are the inviscid and viscous terms respectively.

$$\vec{f}_l * \vec{n}_l = \vec{g}_l + \vec{h}_l \tag{9}$$

Combining a shorthand notation of Equation (8) with (9) yields Equation (10). The vectors $\vec{q}$, $\vec{g}, \vec{h},$ and $\dot{\vec{\omega}}$, for a two-temperature model are defined in Equation (11) through Equation (14).

$$\left[\frac{\delta \vec{q}\Omega}{\delta t}\right]_L + \sum_{l=i,j,k} [\vec{g}_{l+1}\sigma_{l+1} - \vec{g}_l\sigma_l] + \sum_{l=i,j,k} [\vec{h}_{l+1}\sigma_{l+1} - \vec{h}_l\sigma_l] = [\dot{\vec{\omega}}\partial\Omega]_L \tag{10}$$

$$\vec{q} = \begin{bmatrix} \rho_s \\ \rho u \\ \rho v \\ \rho w \\ \rho E \\ \rho e_V \end{bmatrix} \tag{11}$$

$$\vec{g} = \begin{bmatrix} \rho_s U \\ \rho U u + p n_x \\ \rho U v + p n_y \\ \rho U w + p n_z \\ \rho U H \\ \rho U e_V \end{bmatrix} \tag{12}$$

$$\vec{h} = \begin{bmatrix} -\rho D_s \dfrac{\partial y_s}{\partial s_n} \\ -\tau_{nx} \\ -\tau_{ny} \\ -\tau_{nz} \\ -u\tau_{nx} - v\tau_{ny} - w\tau_{nz} - \eta \dfrac{\partial T}{\partial s_n} - \eta_V \dfrac{\partial T_V}{\partial s_n} - \rho \sum_{s=1}^{11} h_s D_s \dfrac{\partial y_s}{\partial s_n} \\ -\eta_V \dfrac{\partial T_V}{\partial s_n} - \rho \sum_{s=1}^{11} h_{v,s} D_s \dfrac{\partial y_s}{\partial s_n} \end{bmatrix} \tag{13}$$

$$\vec{\omega} = \begin{bmatrix} \dot{w}_s \\ 0 \\ 0 \\ 0 \\ Q_{rad} \\ \dot{w}_v \end{bmatrix} \tag{14}$$

In Equations (11) through (14) the first element of the vector defines the species that is being conserved. Elements two through four describe conservation of x, y, and z momentum. Total energy conservation and vibrational/electric energy conservation are described by the fifth and sixth elements respectively. The equations shown are for an 11 species model that includes components of air consisting of N, O, N_2, O_2, NO, all of the corresponding ions, and the free electrons. The translational and rotational energy modes for all heavy particles are assumed to be fully excited and vibrational, bound electronic and free electron modes can be described by two temperature terms, T and T_V respectively [15].

Having the inviscid and viscous terms separated allows a point-implicit discretization of each set of terms to be accomplished. However, this is not a direct process and requires several intermediate steps to get to the end result. Breaking down $\vec{g}_l$ is the first step in the process and can be seen in Equation (15). The terms a_l' and b_l' are geometric weighting functions, R_l and Λ_l are related to the Jacobian of the inviscid flux

vector. The elements of these matrices are averages of the quantities at adjacent cell centers and are required for each cell face.

$$\vec{g}_l = \{a_l' \vec{g}_{L,l} + b_l' \vec{g}_{L-1,l}\} - \left\{\frac{1}{2(\chi n)_l} R_l |\Lambda_l| [\vec{s_l} - \theta_f \vec{s}_l^{min}]\right\} \tag{15}$$

With this term defined there are several sequential steps including nondimensionalization, the use of limiters, scaling and approximate linearization that are required. The nondimensionalization is accomplished by using the freestream velocity and is problem dependent. The limiters use gradients of symmetric functions in the neighborhood of the cell face along with algorithms based on the limiters, this is referred to as symmetric total variation diminishing. Scaling reduces the effect of grid stretching and is eventually removed by numerical dissipation. Finally, the approximate linearization is accomplished with respect to $\delta \vec{q}_L$. After these steps have been completed with several substitutions, the point-implicit discretization of the inviscid portion of Equation (10) can now be accomplished. An application of Stokes' theorem and a simplification will result in well defined inviscid equations, Equations (16) and (17) [15].

$$\sum_{l=i,j,k} [\vec{g}_{l+1,L}^* \sigma_{l+1} - \vec{g}_{l,L}^* \sigma_l] =$$
$$\sum_{l=i,j,k} [\vec{g}_{l+1} \sigma_{l+1} - \vec{g}_l \sigma_l] + M_{L,INV} \delta \vec{q}_L \tag{16}$$

$$M_{L,INV} = \frac{1}{2} \sum_{l=i,j,k} [|A_{l+1}|\sigma_{l+1} + |A_l|\sigma_l] \tag{17}$$

LAURA handles the viscous stresses by defining the shear stresses on cell faces with a unit normal and all three orthogonal directions. After a substitution and simplifying equations according to geometric identities, Equation (18) is derived.

$$\tau_{ns} = \mu_l(\frac{\partial \dot{s}}{\partial \xi} \xi n + \frac{\delta \dot{s}}{\delta \eta} \eta n + \frac{\delta \dot{s}}{\delta \zeta} \tag{18}$$

25

$$+\frac{\partial U}{\partial \xi}\frac{\partial \xi}{\partial s}+\frac{\partial U}{\partial \eta}\frac{\partial \eta}{\partial s}+\frac{\partial U}{\partial \zeta}\frac{\partial \zeta}{\partial s})$$
$$+\lambda_l(\frac{\partial \vec{u}}{\partial \xi}\cdot \vec{\nabla}\xi+\frac{\partial \vec{u}}{\partial \eta}\cdot \vec{\nabla}\eta+\frac{\partial \vec{u}}{\partial \zeta}\cdot \vec{\nabla}\zeta)n_s$$

With the viscous stresses defined in Equation (18), a thin-layer approximation in the computational coordinate directions, Stokes' relation, and geometric identities are used to simplify the equation. The thin-layer approximation only uses one computational direction, ignoring the other two. This approximation is a valid assumption because the overall momentum and energy balance contribution is small. These approximations remain true in the boundary layer as long as the boundary layer is thin and the computational direction chosen is approximately normal to the high gradient region. Contributions from mass diffusion and energy conduction are now accounted for in the viscous terms. With all the contributing terms accounted for, derivatives in the computational directions are taken. These derivatives have no dependence on the cell center and set up the linearization of the viscous terms. Finally, a point-implicit implementation of viscous terms is performed resulting in Equations (19) and (20) [15].

$$\sum_{l=i,j,k}[\vec{h}^*_{l+1,L}\sigma_{l+1}-\vec{h}^*_{l,L}\sigma_l]=$$
$$\sum_{l=i,j,k}[\vec{h}_{l+1}\sigma_{l+1}-\vec{h}_l\sigma_l]+M_{L,VIS}\delta \vec{q}_L \tag{19}$$

$$M_{L,VIS}=\sum_{l=i,j,k}[B_{l+1}\sigma_{l+1}+B_l\sigma_l] \tag{20}$$

The final term from Equation (10) that needs to be defined is the source term. Only an approximate linearization needs to be performed to put the final term into a point-implicit relaxation form. Equations (21) and (22) depict the point-implicit linearization for the source terms.

$$\dot{\vec{\omega}}_L^{n+1} = \dot{\vec{\omega}}_L^n + M_{L,SRC}\delta\vec{q}_L \qquad (21)$$

$$M_{L,SRC} = \frac{\partial\dot{\vec{\omega}}_L}{\partial\vec{q}_L} \qquad (22)$$

Finally, with all of the point-implicit terms defined, the governing relaxation equation can be obtained by combining Equations (10), (16), (19), and (21). Combining these equations results in Equations (23), (24), and (25).

$$M_L\delta\vec{q}_L = \delta t\vec{r}_L \qquad (23)$$

$$M_L = I + \frac{\delta t}{\Omega_L}\left[rf_{inv}M_{L,INV} + rf_{vis}M_{L,VIS} - \Omega_L M_{L,SRC}\right] \qquad (24)$$

$$\vec{r}_L = -\frac{1}{\Omega_L}\sum_{l=i,j,k}\left[(\vec{g}_{l+1} + \vec{h}_{l+1})\sigma_{l+1} - (\vec{g}_l + \vec{h}_l)\sigma_l\right] + \dot{\vec{\omega}}_L \qquad (25)$$

The relaxation factors introduced in Equation (24) are used to enhance the stability and convergence of the flowfield. Several tests have shown the underrelaxation between $2.0 \geq rf_{inv} \geq 1.5$ is appropriate for the inviscid terms and overrelaxation between $1.0 \geq rf_{vis} \geq 0.5$ is appropriate for the viscous terms. The lower limits lead to faster convergence but can also lead to a diverging solution, if the solution is not close to convergence when applied [15]. More information on the formulation of the equations for finite-volumes, conservation, inviscid terms, viscous terms, total energy, vibrational/electronic energy, point-implicit relaxation, and the relaxation algorithm can be found in reference [15].

In order for LAURA to handle the high computational demands that have been discussed, LAURA was designed with distributed-memory computing. LAURA accomplishes this by using parallelism through macrotasking. Macrotasking means

that large sections of code are being processed in parallel on multiple processors. Since LAURA uses a point-implicit relaxation method, as discussed above, each cell is able to use the latest available data from neighboring cells. Being able to use the latest available data and not having to store all of the data results is an efficient use of the multitasking capabilities of a computer. In the current version of LAURA, LAURA 5.5, macrotasking is accomplished by using a message-passing strategy. The domain is subdivided into blocks along the i, j, k coordinate directions and each block has at least one processor assigned to it [14]. Therefore to use this process, the number of processors must be equal to, or a multiple of, the number of blocks present in the domain. Each processor, or group of processors, works only on their own block and transfers boundary information when specified by the user. Since processors use distributed memory, each iteration only requires the storage of information of the block and the boundary data for the block. Riley and Cheatwood found that, LAURA's message-passing ability has increased the convergence and decreased the computational time for several different geometric shapes. This study proves LAURA's effectiveness in distributed-memory parallel system simulations for realistic configurations [14].

LAURA has a strong history of returning very accurate results on external hypersonic flows with domains that are modeled using a structured grid. Since this simulation is a three-dimensional, finite volume, non-equilibrium, full Navier-Stokes simulation with ablation and radiation, LAURA is the clear choice as the solver for the flowfield, particularly the wake.

2.5. Hypersonic Wakes

Unlike most external hypersonic flow studies, this paper will focus on the wake region behind the hypersonic body. This area is generally in a state of thermochemical non-equilibrium and is of interest for four reasons. Of these, only three are applicable to this research and they are: radiative heating of the base region, electron density in the wake, and optical radiation in the wake [16].

The wake region flow behind a hypersonic body is characterized by five phenomena which are depicted in Figure 5 [16]. The first phenomenon encountered is a flow expansion region. This expanding region occurs when flow passes over the shoulder of the body causing a rapid supersonic expansion where most of the chemical reactions are frozen. The second phenomenon is characterized by recirculating flow occurring in the base region of the body, inside of the expanding region. The recirculating flow is subsonic and is almost as hot as the stagnation point at the front of the body. Due to the high temperatures, low velocity, and large body dimensions, the recirculating region flow approaches equilibrium. The expanding region is separated from the circulating region by a thin turbulent shear layer. Moving downstream the third phenomenon encountered is the neck-stagnation point where the flow in the wake reaches the same velocity as the body. The recirculating flow behind the body will have an increased velocity and the flow downstream of the recompression shock will be traveling slower than the body. Due to these variances in speed there is a point that the velocity of the flow in the wake matches the velocity of the body which causes a stagnation region. This neck-stagnation point is normally located about two to three body diameters downstream of the shoulder. The static temperature at the neck-stagnation point is about the same as the temperature

29

of the stagnation point in the front of the body. The pressure at the neck-stagnation point can be on the order of 10% of the stagnation point in the front of the body. The neck-stagnation point is the highest temperature and pressure encountered in the wake region. However, this stagnation point does not always exist in this region due to increasingly complex bodies. The high pressure causes a flow expansion and divergence from the neck which is the fourth phenomenon of interest. Finally, the fifth phenomenon is a weak neck recompression shock that is created by the flow diverging from the neck, which causes flow acceleration and the shock. The hot wake flow in this region will begin to mix with the cooler ambient air but will not become relatively cool until roughly ten body diameters. Even further downstream at 100 body diameters, at a point known as the breakthrough point, the flow is almost the same temperature as the ambient air [16].
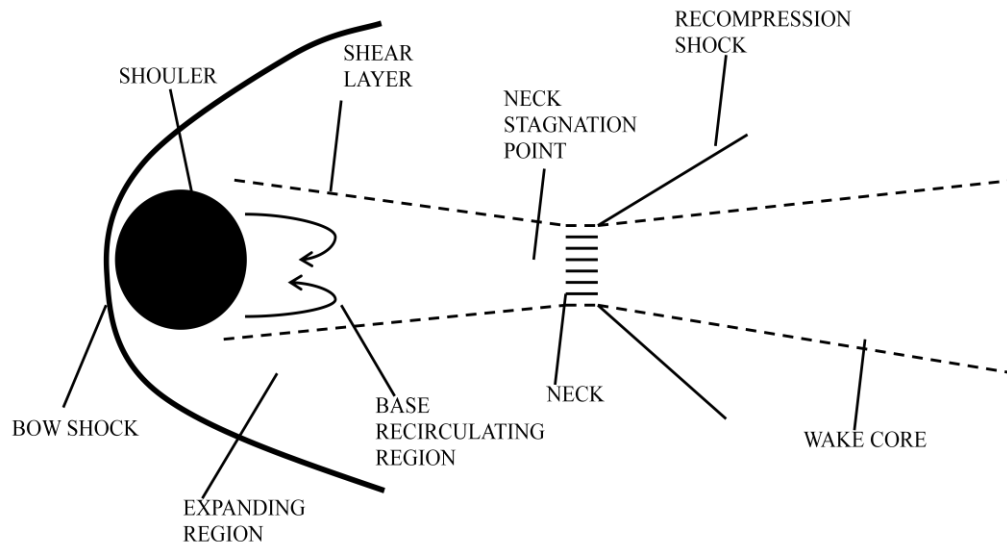

Figure 5. Near-wake Flowfield (based on Park)

These phenomena lead to several reasons of interest to study wake region flow. The first reason of interest in hypersonic wakes is radiative heating in the base region which is caused by the high temperature and the low velocity of the recirculating flow in the base

region. Due to this high temperature, strong radiation can emanate from this region [16]. This region is a possible source of detectable radiation. Electron density in the wake of a hypersonic body is the next reason for interest. In the shock layer over a body there will be ionized species present and these species will recombine in the expanding region. But due to the high temperatures in the base recirculating region, ions will form again. The neck region boasts the highest electron density because of the high temperature and pressure at this point in the wake. This high electron density offers another possible source of detection via remote microwave beams. Optical radiation in the wake is the third reason to study at the wake region of a hypersonic body. The optical radiation, or luminosity, here can be related to the luminosity of meteors entering the atmosphere. This luminosity is caused by the NO chemiluminescense phenomenon. NO chemiluminescense is caused by the recombination of NO and O to form NO_2 in an electronically excited state [16]. This molecule returns to its ground state by emitting optical radiation. The optical radiation in this region has a strong inverse relationship with temperature, meaning that as the temperature increases the optical radiation decreases. Due to this relationship, the NO chemiluminescense is only seen in the far wake downstream of ten body diameters. Clearly this optical radiation is a source of detection of hypersonic bodies. These reasons of interest are all possible sources of detection and will be the focus of the research to follow.

III. Methodology and Procedures

3.1. Chapter Overview

The following chapter will address the methodology used in this research. This research began with selecting proper conditions for the simulation. Once conditions were determined, the grid for the body and flowfield were created and the simulation was run to convergence. With a converged body flowfield, the wake flowfield was generated and the simulation was run to convergence.

3.2. Case Selection

As mentioned earlier the goal of this research is to characterize the phenomena in the wake region of a hypersonic body during the glide portion of a boost-glide flight profile. A wingless-smooth surface blunted cone was used as the body for the simulations. A wingless conic body could be used because the purpose of this study is to characterize the wake region not to analyze a specific body. The smoothed surfaces removed all surface imperfections that were present in a real body under the assumption that these imperfections would not change the overall solution in any significant manner. Arbitrary flight data from reentry was used; this data can be seen in Table 2. Finally, the model was simplified by only using half the body. Since the model was symmetric and there was only pitching, no yawing, only half the body needed to be analyzed.

Table 2. Flight Characteristics

Altitude	30 km
Density	0.01841 kg/m^3
Temperature	226.5 K
Velocity	2115 m/s
Angle of Attack	5°
Yaw	0°

3.3. Body and Grid Generation

Since a blunted cone was going to be the body used for analysis, the LAURA self-start utility was utilized to create the geometry of the body. The LAURA self-start utility is an interactive LAURA utility that "generates a single-block structured grid for families of 2D, axisymmetric and 3D blunt bodies" [17]. The inputs to the LAURA *self-start* utility used to the create geometry can be seen in Table 3.

Table 3. LAURA Self-start Utility Inputs

Dimensionality	3D
Shape	Conic
Unit of Measure	Meters
Cells on Symmetry Plane	64
Cells on Circumferential	45
Cone Shape	Blunted Cone
Cells on Cap	10
Conic Half Angle	6°
Nose Shape	Sphere
Horizontal Nose Radius	0.025
Vertical Nose Radius	0.025
Length	3.5
Cells Prior to Doubling	16

The output from the LAURA *self-start* utility can be seen in Figure 6. Figure 7 and Figure 8 give detailed views of the nose and the tail of the LAURA *self-start* utility geometry. The nose of the body has the highest concentration of cells due to the fact that the flow will be changing the most in this area. It can be seen that the cell size increases down the body. Larger cells were used down the body because the flow is not going through as many changes, therefore a coarser grid can be used. Additionally, the tail end of the body does not have a grid on it because the flowfield does not currently extend into

that region. To make viewing the body easier, a SolidWorks® model of the full body was

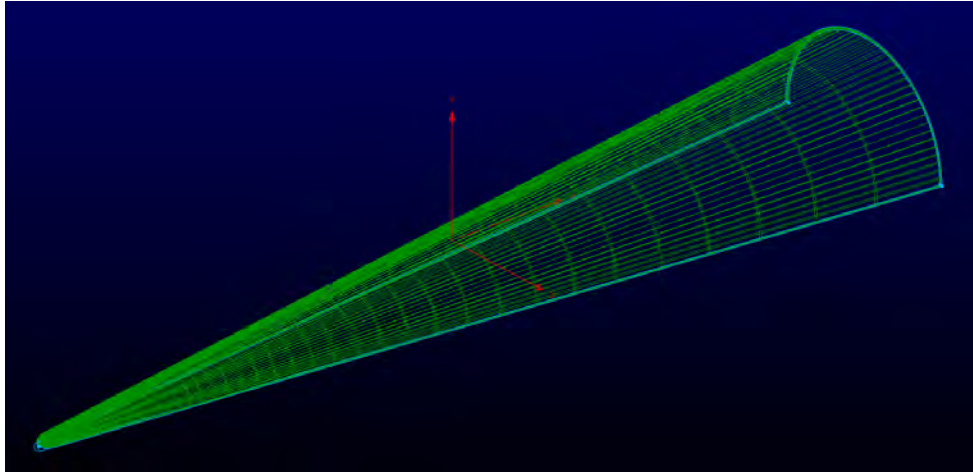created which is depicted in Figure 9.
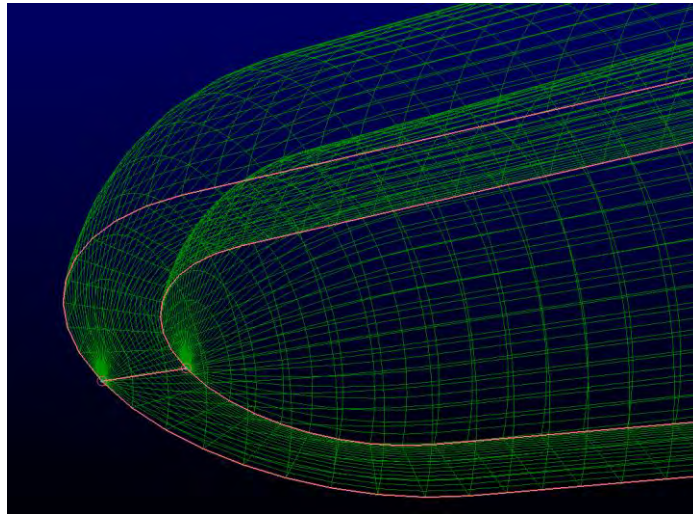

Figure 6. LAURA Self-start Utility Output
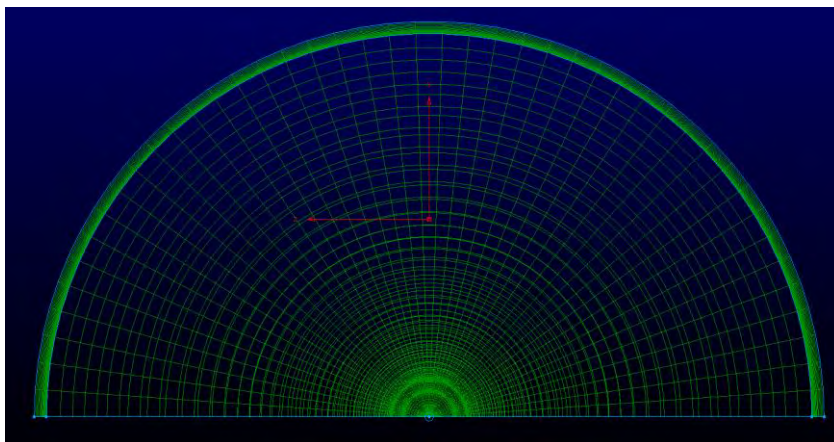

Figure 7. LAURA Self-start Utility Output Nose
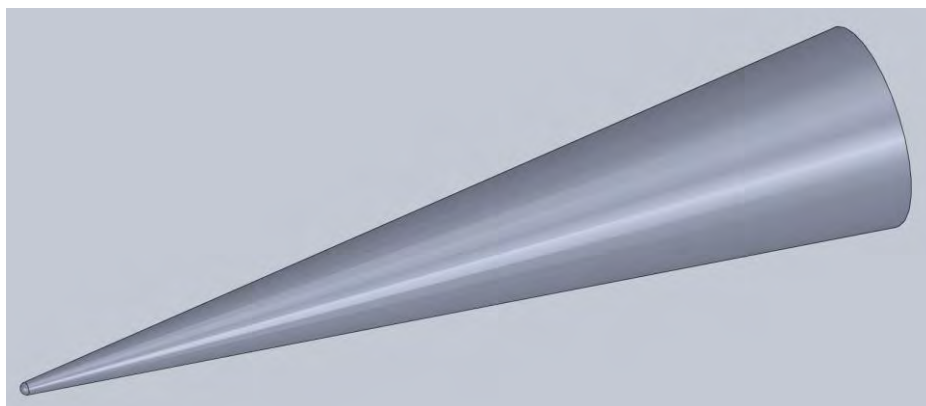
Figure 8. LAURA Self-start Utility Output Tail

Figure 9. Full Body Representation of LAURA Self-start Utility Output

As seen in the figures above, LAURA creates a structured grid with pole boundaries. If this research was interested in the stagnation region at the nose then a new grid would need to be generated to remove the pole boundaries to provide a more accurate solution. A small inaccuracy at the nose of the body, due to the pole, was deemed to have a negligible effect on the wake flow. For this reason the LAURA self-start utility grid was utilized to analyze the flow over the body.

3.4. LAURA Analysis of Body

With the grid completed, the first step in LAURA was to assign the boundary conditions for all the sides of the blocks. Each block consists of 6 faces; i_{min}, i_{max}, j_{min}, j_{max}, k_{min}, and k_{max}. The faces within each block were assigned a numeric value between 0 and 3 in the *laura_bound_data* file. The numeric values represented a solid surface, an outflow boundary, a symmetry boundary across y=constant, or a farfield/freestream boundary for the values between 0 and 3, respectively. These boundary conditions defined how LAURA would interact with each of the faces of the blocks thus defining the flowfield for the simulation.

The next step in preparing for LAURA simulations was to setup the *laura_namelist_data* file. This file defines all the operating parameters for the simulation; from environmental conditions to the exchange of information with LAURA. An initial *laura_namelist_data* file was created with the LAURA self-start geometry. While this file created a working *laura_namelist_data* file, there were several parameters that needed to be addressed or changed for this particular simulation. These parameters fall into two different categories: parameters that were permanent through all simulations; and, parameters that were incrementally changed through the simulation. While not all parameters will be addressed, the major ones will be addressed in the following two paragraphs. Samples of several of the *laura_namelist_data* files can be found in Appendix A: LAURA Namelist for Simulations.

Since the *laura_namelist_data* file was created from the LAURA self-start utility, the moments of center, xmc, ymc, and zmc for the X, Y, and Z directions respectively were determined by LAURA. Since LAURA calculated the moments of center, this

allowed for moments of center to be the rotation point for when an angle of attack was added to the simulation. The first three parameters that were changed were all environmental parameters; velocity (*velocity_ref*), density (*density_ref*), and temperature (*tref*). All of these values were changed to the flight conditions that were mentioned earlier in Section 3.1. The following parameters defined how LAURA handled the flowfield and what physical parameters LAURA could use. Chemical sourcing (*chem_flag*) and thermal sourcing (*therm_flag*) were both turned on since the flow did not meet the criteria to be frozen. Since the full set of Navier-Stokes equations were desired to produce a more accurate solution, the default of Thin-layer Navier-Stokes needed to be changed with the *navier_stokes* flag. The final flowfield property to be set was whether the fluid was viscous or inviscid using the *ivisc* flag. The *ivisc* flag was set to viscous to better represent a real world flowfield. With the characteristics of the flowfield defined, the surface of the body needed to be defined. Defining the surface was accomplished with setting the surface boundary conditions with the catalysis model (*catalysis_model_0*) and the surface temperature model (*surface_temperature_0*). The catalysis model was set to "equilibrium-catalytic" which references the cell above the surface for elemental mass fractions and sets the species concentrations to equilibrium for the temperature and pressure at the surface. The surface temperature model was set to "radiative equilibrium" which forces the radiation heat flux to be in equilibrium with the heat flux to the wall. The final parameters that were not changed were grid clustering around the shock (*ep0_grd*), fraction of k-cells in the boundary layer (*fstr*), and the sensing parameter for detecting the shock (*jumpflag*). The grid clustering around the shock was set to a value of "5" which resulted from similar research that had success

37

using this value [18] [19] [20]. The fraction of k-cells in the boundary layer was left as the LAURA default, 0.75. This fraction ensured there were enough cells in the boundary layer to produce an accurate solution. The final grid parameter was the sensing parameter for detecting the shock. This parameter was also kept at the LAURA default which used density as the sensing parameter. Density was chosen because it is the most stable option which is needed early in the simulation when temperature and pressure have significant fluctuations. All of the previously mentioned parameters were set at the beginning of the first simulation and were not changed throughout all of simulations [17].

The parameters that were incrementally changed had to be handled in such a manner to increase the stability of the simulation and give LAURA a better chance to converge on the correct solution. The first step in setting up the simulation was to increase the relaxation factors for inviscid flows (*rf_inv*), viscous flows (*rf_vis*), and radiative equilibrium wall temperature (*ept*) to "9", "3", and "0.01" respectively. The inviscid and viscous relaxation factors act as filters to what data is usable to develop a solution. When first starting a simulation, these values are set to a higher level to allow more data to be used. While these higher values do cause the simulation to take longer to converge on the correct solution, it creates a more stable operating environment. This stable environment is important at the beginning when the simulation is more susceptible to crashing or diverging. The relaxation parameter for radiative equilibrium wall temperature is a multiplicative value that controls how much the wall temperature can change between iterations. A value of "0.01" was used at the beginning of the simulation to decrease the number of iterations that it will take LAURA to converge on the actual surface temperature. As the solution began to converge the relaxation factors were slowly

brought down to their final values of "3" and "1". However, once the solution is close to convergence the relaxation parameter for radiative equilibrium wall temperature was reduced to "0.001" to allow for fine tuning. All of these relaxation factors could also be adjusted based on where LAURA was seeing the greatest error. If most of the error was in the region outside of the boundary layer then the relaxation factors for inviscid flows could be increased to allow more data to be used to start converging on the correct solution [4].

With LAURA's operating conditions set, the chemical species for the simulation needed to be identified. The chemical species were set using the *tdata* file and the inputs can be seen in Table 4. Finally, the simulations were ready to start running. However,

Table 4. LAURA Chemical Species List without Ablation

Species	Concentration
N	6.217E-20
O	7.758E-09
N_2	0.737795
O_2	0.262205
NO	1.00E-09
NO+	4.567E-24
e-	8.352E-29

when LAURA starts a fresh simulation everything is at rest. For the simulation to go from an object at rest to an object traveling at hypersonic speeds with an angle of attack and operating in a turbulent environment would cause the model to be highly unstable and fail. For that reason the complexity of the simulation was incrementally increased. All simulations were conducted at the previously mentioned velocity, reference density, and reference temperature. The first set of simulations was conducted with shock alignment (*movegrd*) being called every 200 iterations, the maximum number of cells in

the normal direction (*kmax_final*) set to 16, angle of attack (*alpha*) of 0, and turbulence set to off (*turb_model_type*). The shock alignment subroutine was called often due to the large changes the flowfield was going through from being at rest to moving at 2,115 m/s. As more iterations were completed and the total error (L_{2norm}) of the simulation decreased, the shock alignment call frequency was increased to 1,000, 2,000, 5,000, and finally 10,000. Taking this approach allowed the grid to move more in the beginning when the environment was experiencing a significant amount of change in the gradients. It also let the grid settle and make small adjustments once the gradients were established. Starting with 16 cells in the normal direction was done for two reasons. The first was that it enabled the simulations to run faster since computational time exponentially grows with the number of cells present. For example, if the number of cells is doubled, the computational time is multiplied by a factor of four. Second, having only 16 cells in the normal direction, which is a quarter of the final desired number of cells, allowed the simulation to start in a more stable environment and have a better chance of converging (as discussed earlier) while being able to grow to arrive at a more accurate solution. Doubling the cells in the normal direction was accomplished using LAURA's doubling feature and was set to be done when the L_{2norm} was less than 10^{-3}. The grid results from the simulations with 16, 32, and 64 cells in the normal direction are depicted in Figure 10 through Figure 15.
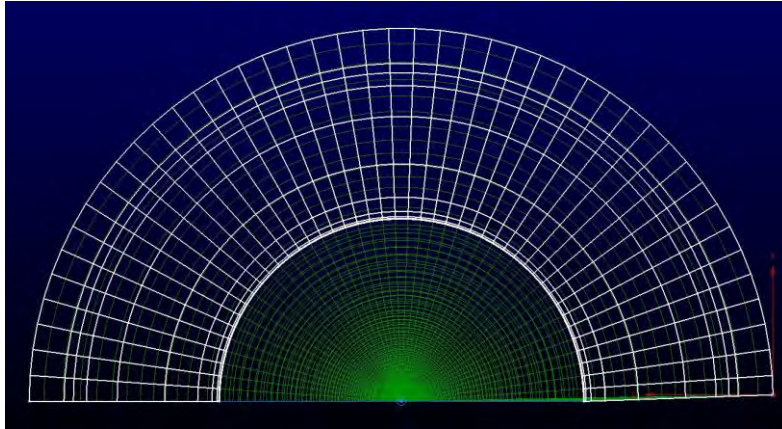
Figure 10. Aft End of Flowfield Grid after LAURA Simulation with 16 Cells in the Normal Direction
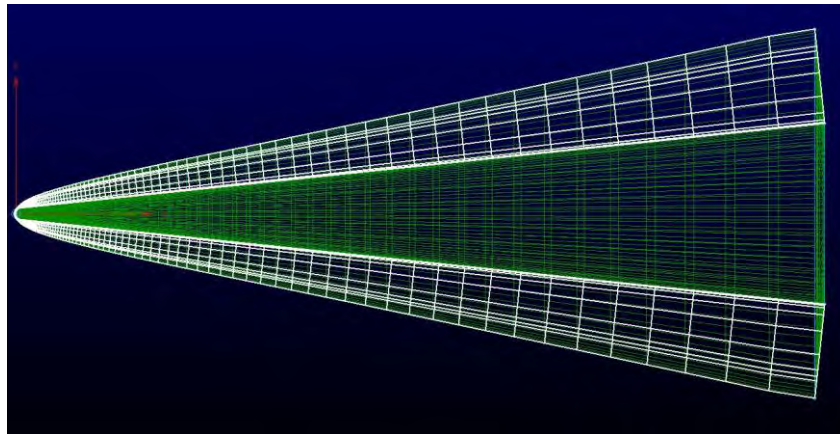

Figure 11. Symmetry Plane of Flowfield Grid after LAURA Simulation with 16 Cells in the Normal Direction
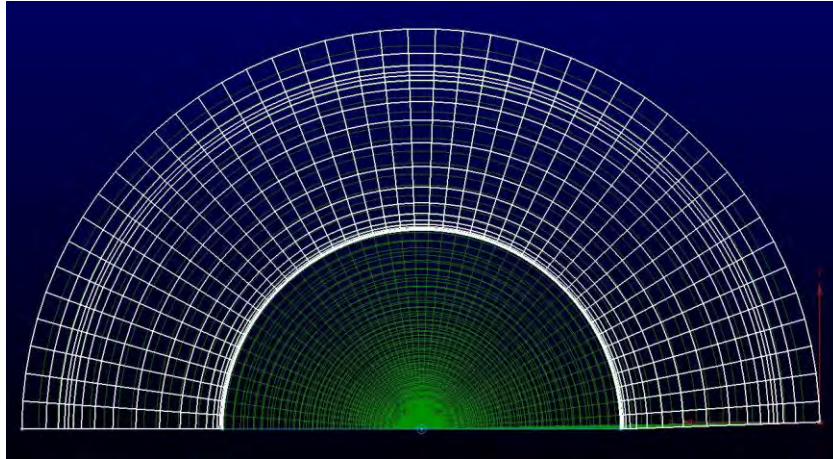
Figure 12. Aft End of Flowfield Grid after LAURA Simulation with 32 Cells in the Normal Direction
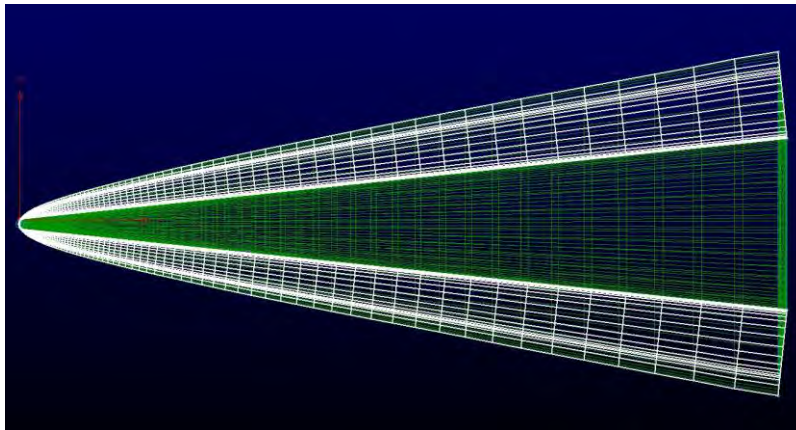

Figure 13. Symmetry Plane of Flowfield Grid after LAURA Simulation with 32 Cells in the Normal Direction
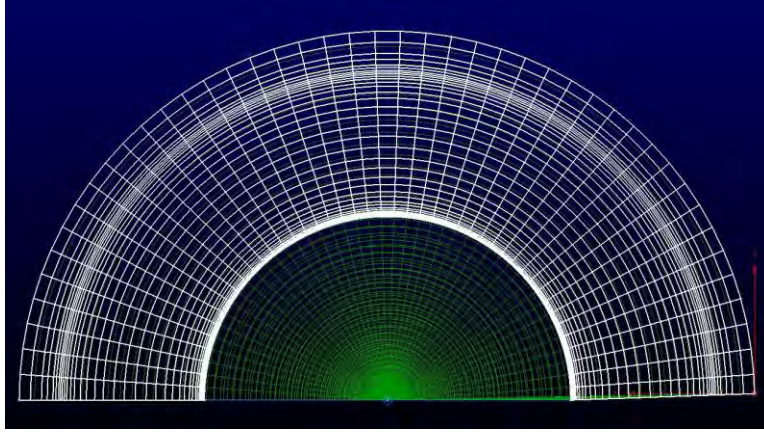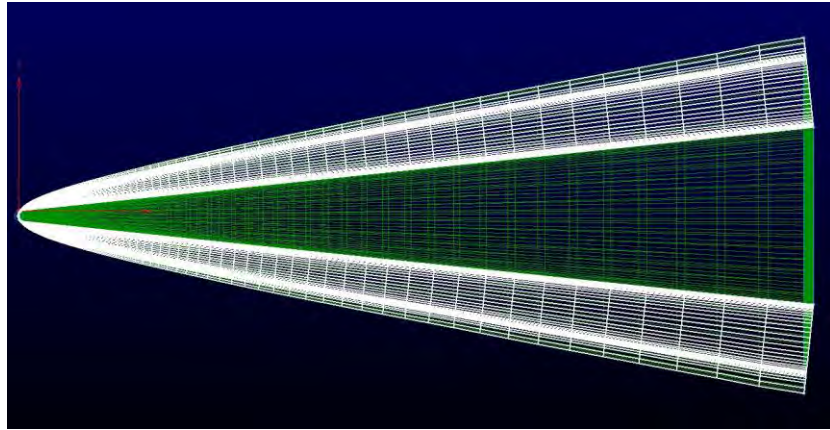
Figure 14. Aft End of Flowfield Grid after LAURA Simulation with 64 Cells in the Normal Direction

Figure 15. Symmetry Plane of Flowfield Grid after LAURA Simulation with 64 Cells in the Normal Direction

Once the simulation L_{2norm} was below 10^{-3} with 64 cells in the normal direction the simulation was ready to add an angle of attack. Following the strategy of incrementally increasing the complexity, the solution was not taken from 0° to 5° angle of attack, but slowly increased. The first simulation was run with an angle of attack of 1° which was increased to 2.5° after the L_{2norm} was below 10^{-3}, and finally set to 5° after the L_{2norm} was below 10^{-3}. After the solution converged to a L_{2norm} below 10^{-3}, the simulation was ready for the final step of adding turbulence. The Baldwin-Lomax algebraic

turbulence model was chosen since that model is less complicated than many other turbulence models, and it accurately solves turbulent flow over axisymmetric bodies. [21]. For the Baldwin-Lomax model to be used a developed shock and boundary layer is required. Needing a developed shock and boundary layer is the reason for running the simulation in the laminar case to this point. With turning on the turbulence model there was a significant jump in the L_{2norm} which is expected since the governing equations to the flow have changed. As with the simulations prior to this, the L_{2norm} will begin to decrease as LAURA begins to solve the new governing equations. Although the L_{2norm} started to decease, it was at a much slower rate due to the higher viscosity for the turbulent flow acting as damping for the solution. To help decrease the amount of time that was required for the solution to converge more, processors were used to run the simulation. The addition of more processors, with turbulence models turned on, has been tested and verified to still produce accurate solutions [21]. The results from the increase to an angle of attack of 5° and turning on the turbulence model are depicted in Figure 16 through Figure 19. As can be seen in the figures, the grid is no longer symmetric about the body. This shift in the grid is due to the 5° angle of attack that the body is at causing there to be different gradients on the windward and leeward side of the body. Additionally, turning on the turbulence model did not significantly change the grid but it did alter the results from the simulation.
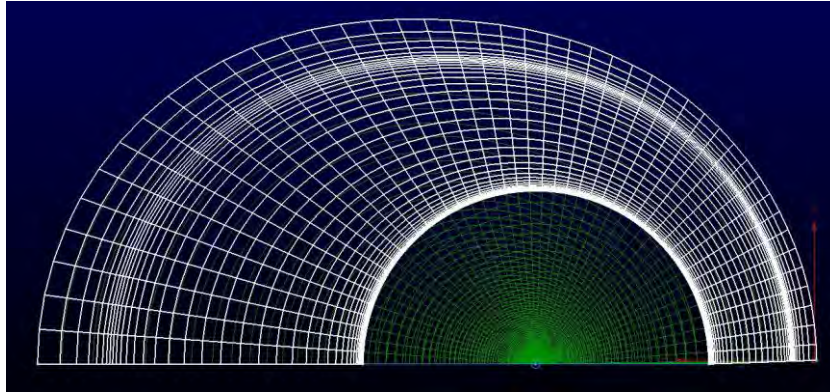
Figure 16. Aft End of Flowfield Grid after LAURA Simulation with 64 Cells in the Normal Direction with an Angle of Attack of 5°
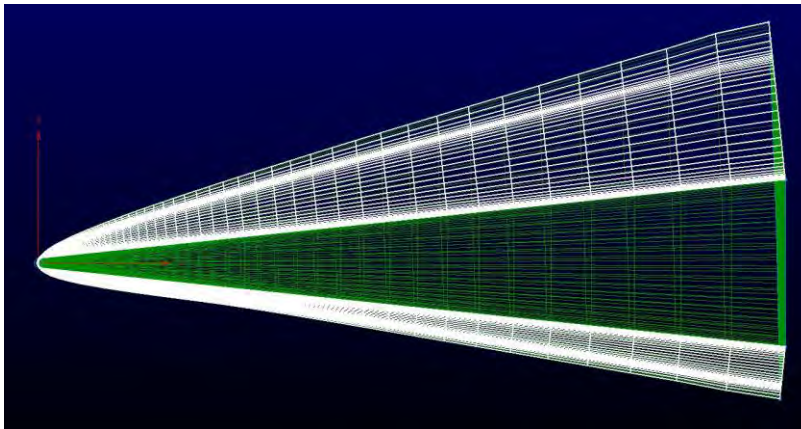

Figure 17. Symmetry Plane of Flowfield Grid after LAURA Simulation with 64 Cells in the Normal Direction with an Angle of Attack of 5°
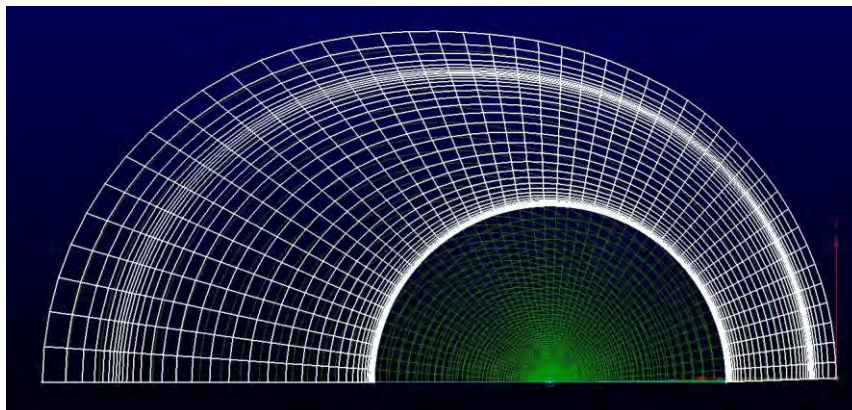

Figure 18. Aft End of Flowfield Grid after LAURA Simulation with 64 Cells in the Normal Direction with an Angle of Attack of 5° including Turbulence
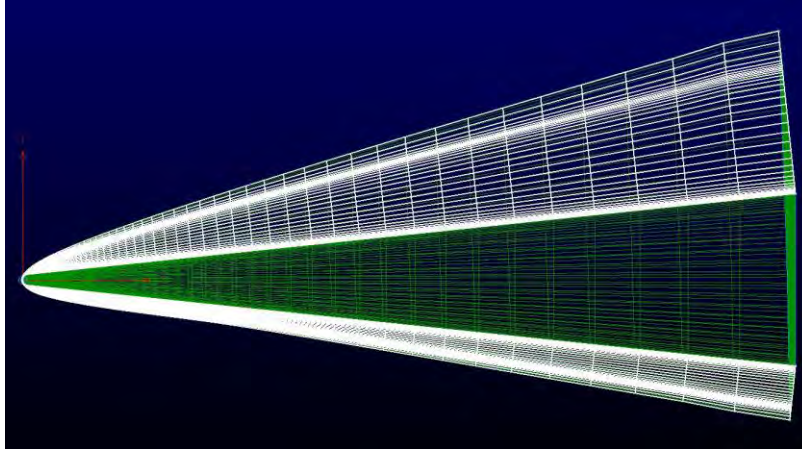
Figure 19. Symmetry Plane of Flowfield Grid after LAURA Simulation with 64 Cells in the Normal Direction with an Angle of Attack of 5° including Turbulence

Throughout this process the L_{2norm} of the simulation was monitored as a gauge of convergence. L_{2norm} represents the error between the simulation and what can be expected in a real world situation. In other words, the lower the L_{2norm} the more accurately the solution represents what would be happening in a real world situation. In similar studies it was found that a L_{2norm} of 10^{-4} was more than adequate for a converged solution and even a L_{2norm} of 10^{-2} still produced accurate results [19] [22] [18]. While monitoring L_{2norm} was acceptable for a first order measurement of convergence it did not necessarily mean that the solution was converged. To measure final convergence, convective heat transfer, or heat flux, was used. Convective heat transfer is a good measure of convergence because it is derived from several other variables and is the last quantity to change in the flowfield. Since L_{2norm} is a representation of error within the flowfield and convective heat transfer is the last value to converge, there is a direct correlation between the two within LAURA. It was found that there was little difference in convective heat transfer when monitoring L_{2norm} decreases from 10^{-2} to 10^{-3} and 10^{-3} to 10^{-4} [19] [22] [18].

46

For this reason a L_{2norm} of 10^{-3} was considered acceptable for this study and convective heat transfer was monitored for convergence.

Monitoring heat transfer was accomplished by checking the heat transfer from the body at different points during the simulation progression. Tracking heat transfer was done by pulling lengthwise data lines off of the body and plotting the heat transfer along those lines. Once there was little to no change between the plots, the simulation could be considered converged. Figure 20 and Figure 21 show heat transfer from a suspected converged model compared to a model that ran for an additional 10,000 iterations. As seen from the figures, the difference in the heat transfer between the 2 simulations is almost negligible with the maximum difference being roughly 5%. For this reason, this grid was considered converged and wake region grid generation could be started.
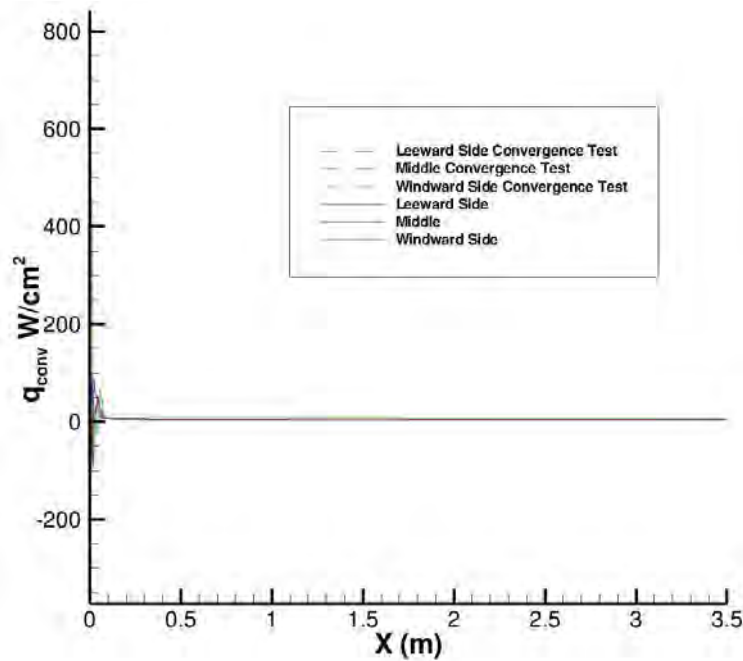

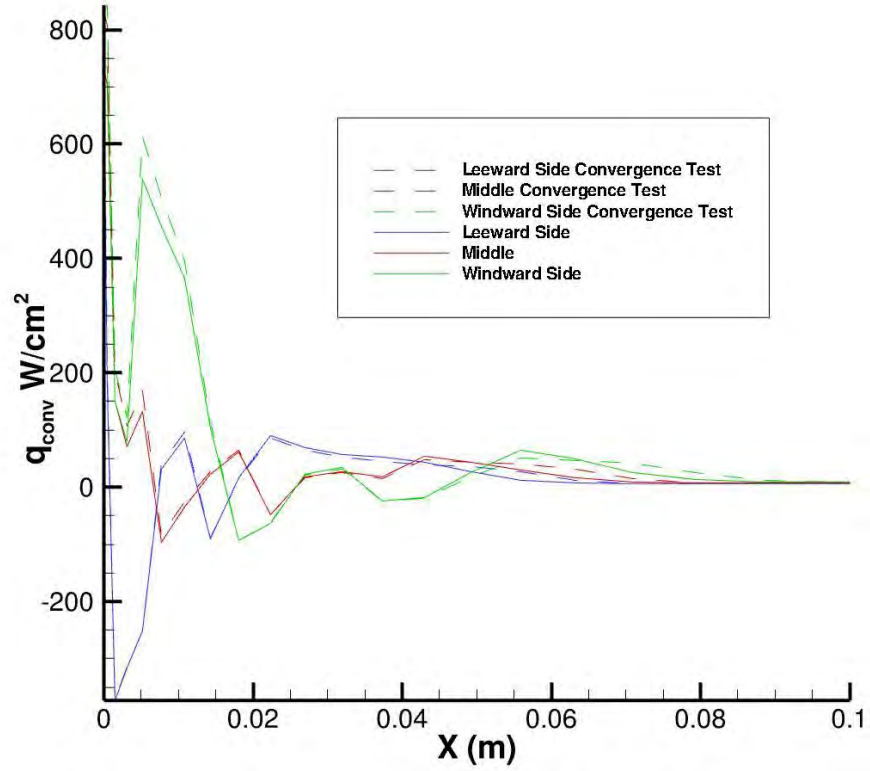Figure 20. Convective Heat Transfer Plot along the Complete Body Length

Figure 21. Convective Heat Transfer Plot along the Body Nose

3.5. Wake Region Grid Generation

The first step in generating a wake region grid was to create a grid for the tail end of the body. A pole grid had to be used on the tail end of the body due to the pole grid that was used on the body and the flowfield around the body. This grid is depicted in Figure 22. Once the end grid was completed, it was extruded to a distance equivalent to five body diameters. This distance was chosen because it would capture the neck stagnation point at two body diameters and end before the wake became far-wake at roughly ten body diameters, which is of no significance to this research [16]. The extruded wake core is depicted in Figure 23 and Figure 24. The extruded grid caused a pole grid to be present through the middle of the entire wake core. Additionally, a

48

significantly finer spacing was used in the area where the neck stagnation region and recompression shock were thought to be located.
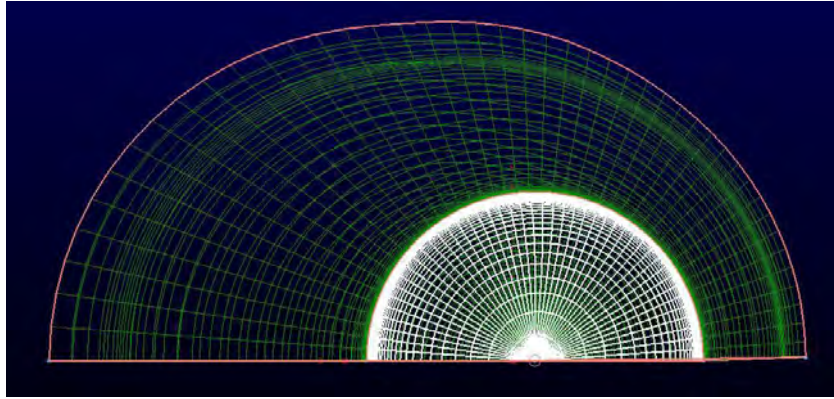

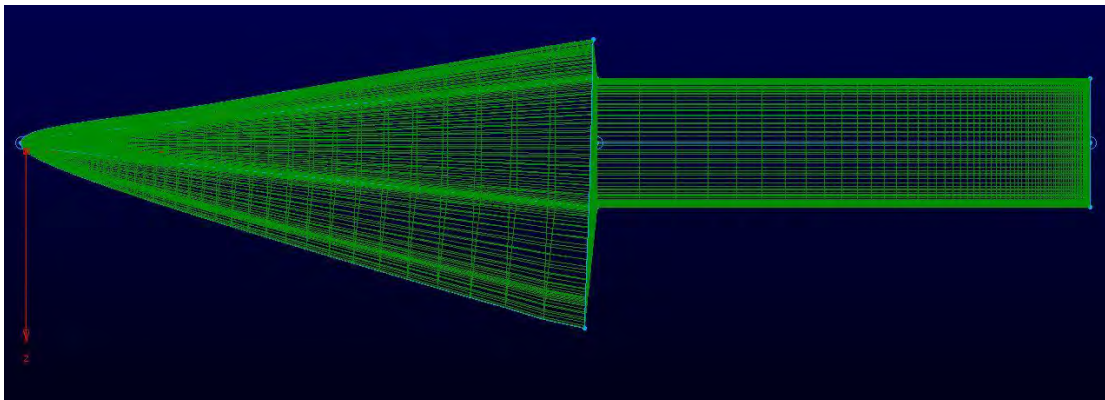Figure 22. Grid on Tail End of Body
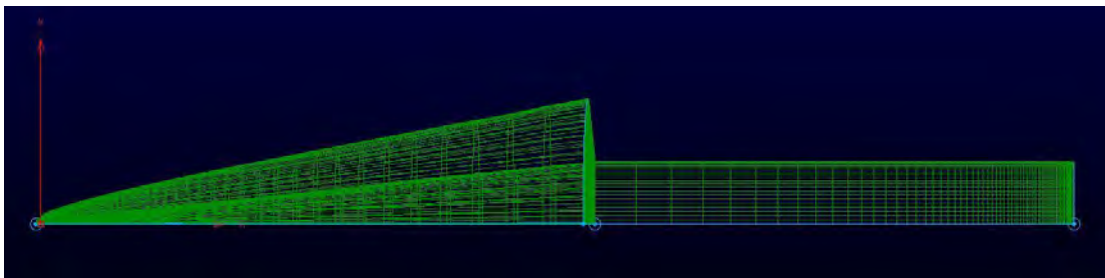

Figure 23. Body and Wake Region Core Top

Figure 24. Body and Wake Region Core Side

Unfortunately, the rest of the wake region could not be created using the same method because extruding the flowfield would have caused a dramatic change in the cells,

causing the cells to be highly skewed at the transition to the wake. For this reason the rest of the wake grid was developed by hand. The flowfield boundary lines were extended to match the end of the wake core on the same slope as the flowfield boundary lines. To complete the frame a semi-circle was used to connect the wake flowfield boundary lines. The resulting grid frame and grid is depicted in Figure 25 through Figure 28.
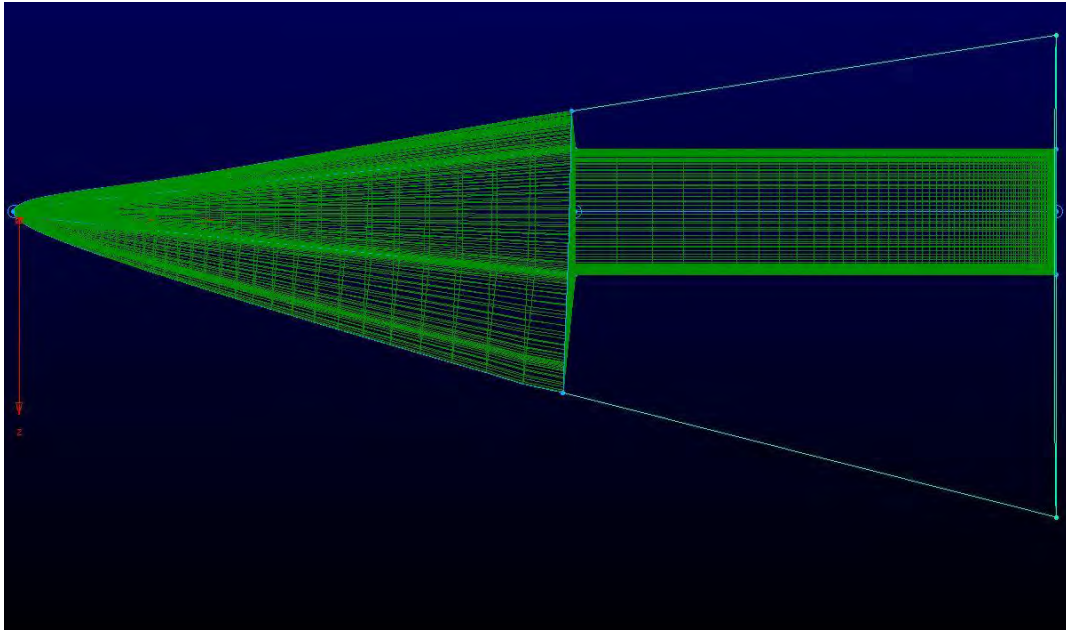

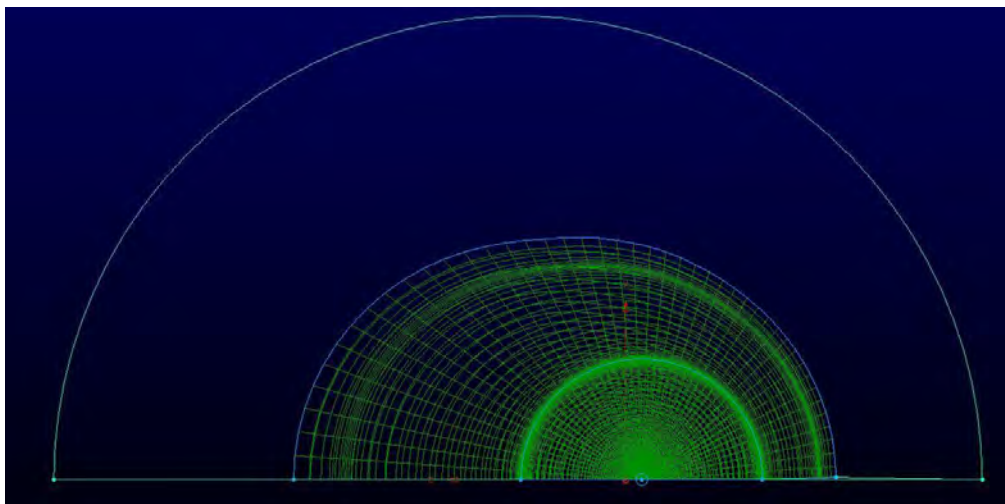Figure 25. Body and Wake Region Frame Top
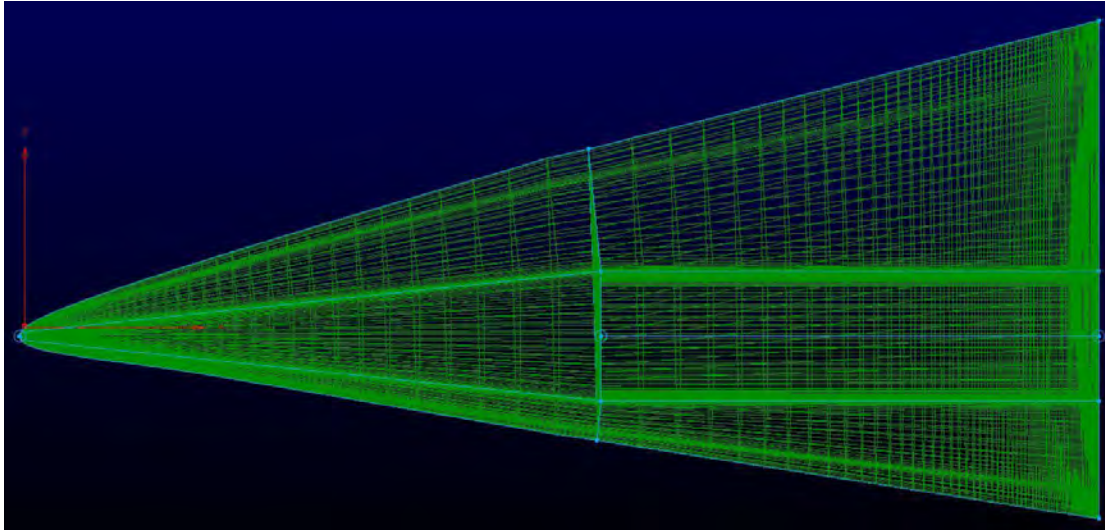

Figure 26. Body and Wake Region Frame End
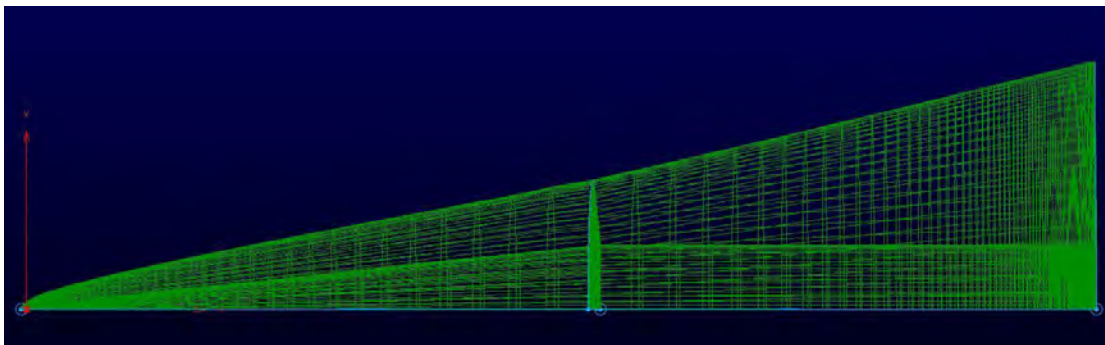
Figure 27. Body and Wake Region Symmetry Plane

Figure 28. Body and Wake Region Side

In order to use the multiprocessor point-implicit computing of LAURA with turbulence, blocks cannot be split in the k-direction, or body normal. To solve this issue, LAURA has a built-in command for the *laura_namelist_file* called *sweep_direction*. By changing *sweep_direction* to split the blocks in the i-direction, or lengthwise down the body, LAURA would switch how the blocks are divided allowing the simulation to still use the multiprocessor computing with turbulence [17]. However, there had been issues with getting this method to work in the past such as; the simulation solving for solutions that are not numbers or not initializing. Due to the past issues, this method was not used

and a second grid was developed to still allow for multiprocessor point-implicit computing. This second grid used the completed wake grid is depicted in Figure 27 and Figure 28. This grid was split it into 32 blocks lengthwise, keeping the computational block size as similar as possible. The similar block size would keep the computational time on each block roughly the same which causes the simulation to be more stable. The 32 block grid is depicted in Figure 29 and Figure 30. 32 blocks was chosen to allow LAURA to use multiprocessor point-implicit computing by assigning only one processor to each block, essentially forcing the blocks to be divided in a lengthwise sweep.
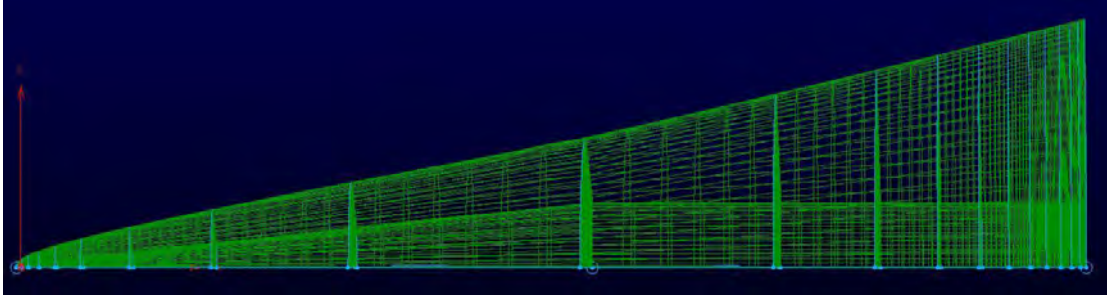
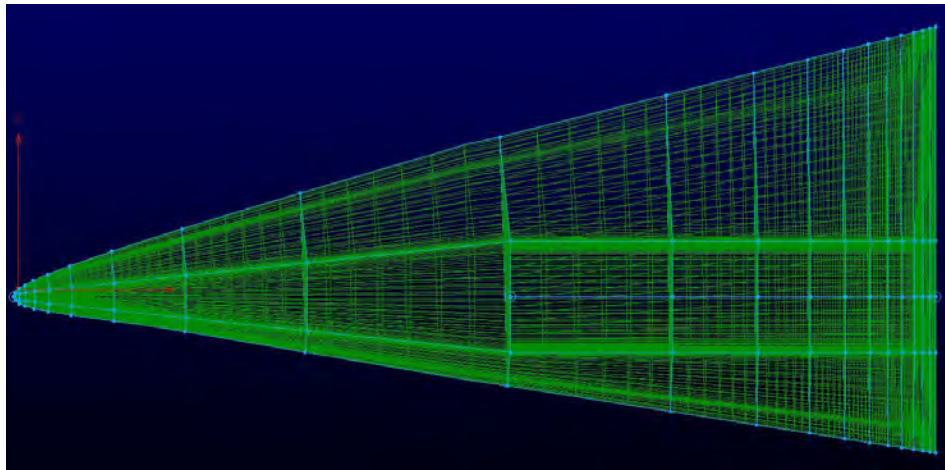

Figure 29. Body and Wake Region 32 Block Side

Figure 30. Body and Wake Region 32 Block Symmetry Plane

3.6. LAURA Analysis of Body and Wake Region

With the wake region grid completed, the LAURA simulations were now ready to be started. Unfortunately, since the wake region was added to the body original grid, the solution files from the body only simulation cannot be used. Due to this, the simulations needed to be started from scratch. The process for this set of simulations was similar to that used in the body simulations except for changing two parameters. The first change was disabling *movegrd*. LAURA could not run with *movegrd* enabled because LAURA moves the grid in the body normal direction. With the absence of a body in the wake region, the first call of *movegrd* would cause the simulation to fail. The second change was with the turbulence model, changing it from the Baldwin-Lomax to the Wilcox *k-ω* turbulence model. The turbulence model needed to be changed from the Baldwin-Lomax algebraic turbulence model, even though the model has good agreement with experimental data and other numerical results for slender bodies, because it does not model regions of detached flow successfully [21]. A new model needed to be used that was accurate in hypersonic flow, detached flows, and boundary layers, as well as one that could handle eddies. These requirements led to the selection of the Wilcox *k-ω* turbulence models.

The Wilcox *k-ω* 2006 turbulence model was selected, over the 1998 model, for two reasons. The first is the significant improvement to how the model handles both boundary layers and free shear flows over the Wilcox *k-ω* 1998 turbulence model. This improvement was accomplished by including one new closure coefficient and an adjustment to the dependence on eddy viscosity on turbulence properties. This new model has minimal sensitivity to the freestream boundary conditions on turbulence

53

properties. Secondly, the 2006 model was chosen for its ability to handle complicated separated flows. By adding cross diffusion to the specific dissipation rate and introducing a stress-limiter modification, the 2006 model was expanded to include over 100 different applications including free shear flows, boundary layer flows, and separated flows at Mach numbers ranging from incompressible through hypersonic. For these reasons the Wilcox k-ω 2006 turbulence model was used for all turbulence calculations for the body and wake region [20].

While the iterative process used for the LAURA simulations was the same, the L_{2norm} could not be used as a measure of convergence at any point due to the inherently unsteady nature of the flow in the wake region. To check convergence, flow properties such as temperature, pressure, and streamlines, were all monitored and would determine when to change the relaxation factors for inviscid flows and viscous flows and to turn on the turbulence model. Ultimately, convective heat transfer was once again used to check for model convergence. Once convergence with turbulence was obtained, the ablation model was activated.

Ablation needed to be added to the simulation due to the relatively low altitude and the high velocity of the body. At this speed and altitude there is a massive amount of convective heat transfer from the atmosphere to the body. This heat transfer would cause the body to burn up and have an enormous radiative signature. To avoid these problems, a thermal protection system is added to the body. The thermal protection system protects the body and reduces the radiative signature by burning and flaking away. This burning and flaking away helps to keep the surface relatively cooler therefore making the body survive the high heat transfer and reducing the radiative signature.

54

Thermal protection systems are primarily made of carbon because of its ability to reject heat by radiating the heat to space as well as its excellent surface emissivity. This research assumes that carbon is the only material that is ablating off the surface. To model this in LAURA, the default settings *CHNOSi_frac_char_0* and *CHNOSi_frac_pyrolysis_0* flags were used. The default settings for these flags set the thermal protection system material and glue to pure carbon. To account for the additional carbon in the flowfield and the possible chemical reactions that may occur due to ablation the *tdata* needed to be updated. The updated *tdata* inputs are shown in Table 5.

Table 5. LAURA Chemical Species List with Ablation

Species	Concentration
N	6.217E-20
O	7.758E-09
N_2	0.737795
O_2	0.262205
NO	1.00E-09
NO+	4.567E-24
e-	8.352E-29
C	1.00E-25
C_2	1.00E-25
C_3	1.00E-25
CO	1.00E-25
CO_2	1.00E-25
CN	1.00E-25

Setting the simulation for ablation was the final preparation step. This step was accomplished using 2 files; the *laura_namelist_data* and *surface_property_data*. The following flags were all added to the *laura_namelist_data* file. The first flag set was *ablation_option*. *Ablation_option* was set to a value of "0" which calculates the char ablation rate, the pyrolysis ablation rate, and the wall temperature. The second flag set was *blowing_model_0*. *Blowing_model_0* was set to "equil_char_quasi_steady" which

solves the equilibrium surface ablation problem. The "equil_char_quasi_steady" calculates the char ablation rate, wall temperature and elemental composition at the surface. These values are calculated by using an energy balance, elemental mass balance, and char equilibrium constraint, as well as pressure from the normal momentum equation. Char ablation rate, wall temperature and elemental composition at the surface define the equilibrium species at the surface of the body. This model does not currently calculate the pyrolysis ablation rate or the conductive heat flux into the solid material. These values are approximated by using steady-state ablation approximation. The steady-state ablation approximation sets a pyrolysis ablation rate that is proportional to the char ablation rate. The enthalpy at the surface is used to set the proportional in-depth conduction. In order to use the "equil_char_quasi_steady" option the *surface_temperature_type* flag must be set to "surface energy balance". The "surface energy balance" option is required because it uses the surface energy balance and surface chemistry kinetics to compute the surface wall temperature, which is appropriate for ablating surfaces [17]. The third flag used was the *bprime_flag*. The *bprime_flag* was left to the default value of "1" which sets simulation up for the Partially-Coupled approach. The Partially-Coupled approach applies an approximation for elemental diffusion mass flux, but handles the flowfield with coupled ablation. The Partially-Coupled approach differs from the Uncoupled and Fully-Coupled approaches by the approximations that are used. The Uncoupled approach uses an approximation for both the influence of mass flux on heat transfer and elemental diffusion mass flux at the surface. The Fully-Coupled approach does not use any approximations and is therefore the most accurate of the three options. Even though the Partially-Coupled approach is not the most accurate approach, it offers several

56

advantages over the other approaches. The Partially-Coupled approach only uses one approximation and is therefore more accurate than the Uncoupled approach. The Partially-Coupled approach also converges on a solution significantly faster than the Fully-Coupled approach. However, the Partially-Coupled solution does use an approximation for the elemental diffusion of mass flux at the surface. It is interesting to note that a converged Partially-Coupled solution is normally the initial condition for attempting a Fully-Coupled approach. For these reasons the Partially-Coupled approach was used and as Johnston, Gnoffo, and Mazaheri point out, "This procedure is very robust and converges for a wide range of ablation rates [23]." As mentioned, the ablation rates and wall temperatures are unknown and need to be calculated. To make LAURA calculate these values the *compute_mdot_initial* flag is used with a value of "1". Setting *compute_mdot_initial* to "1" causes LAURA calculate the wall temperature and the ablation rates prior to the first flowfield iteration [17]. With the *laura_namelist_data* file setup, the *surface_property_data* file needed to be setup. This file was used to turn off ablation, due to low temperatures, in all of the blocks other than the first two blocks by assigning a second surface in the *laura_bound_data* file. The only flags included in the *surface_property_data* file were *surface_temperature_type*, *catalysis_model*, and *blowing_model*. S*urface_temperature_type* was set to "radiative equilibrium' in keeping with the rest of the simulation. *Catalysis_model* was set to "fully-catalytic" since the surface temperatures were near 1,000K and the LAURA "fully-catalytic" model is more robust at these temperatures. Finally, *blowing_model* was set to "none" to ensure there was no ablation in these regions.

57

With both the *laura_namelist_data* and *surface_proprty_*data files setup the final set of simulations is ready to be run. These simulations are similar to previous simulations because they are iterative around *rf_vis*, *rf_invis*, and *ept*. Once again, L_{2norm} could not be tracked for convergence but convective heat transfer needs to be used. Since this is the final change to this research, the results can be seen in the following section.

IV. Results and Analysis

4.1. Chapter Overview

The following chapter examines the results from the previously discussed methodology. The chapter is split into two major sections presenting the results for both the surface of the body and the flowfield around the body including the wake.

Section 4.2 displays the results from the surface of the body. Included in this section is a study of the convective heat transfer, temperature, and several other thermophysical properties. Along with these results, the results from ablation with regard to the body are included.

Section 4.3 displays the results from the flowfield around the body as well as the wake region. Discussed in this section are the thermophysical properties of the flowfield and the results from ablation on the flowfield. This section will also compare the results found to the phenomena that were discussed in Section 2.5.

For reference, the windward side of the body is in the negative z-direction and the leeward side of the body is in the positive z-direction. The term "center" is referring to the point that is halfway between the leeward and windward side of the body. This point was a 90° rotation from both the leeward and windward sides. Additionally, at any point a concentration is displayed, it is in a mass fraction unless otherwise stated.

4.2. Surface Results

After many simulations had been run, a converged solution was suspected of being obtained. As mentioned earlier, L_{2norm} could not be tracked as an overall measure of convergence for the simulation, so convective heat transfer was used. The data from the suspected converged simulation was run for another 20,000 iterations to ensure

convergence. The convective heat transfer from the two sets of data was compared and is depicted in Figure 31 and Figure 32. The maximum difference between the two data sets was 15 W/cm^2 which correlates to a 5% difference. At this point the simulation was considered converged and analysis of the results began.
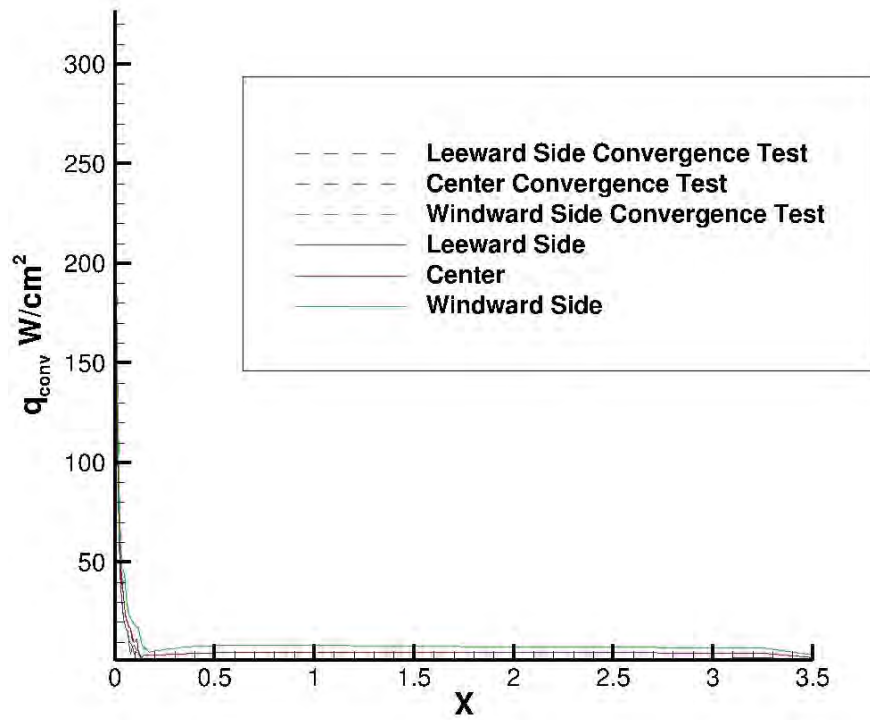

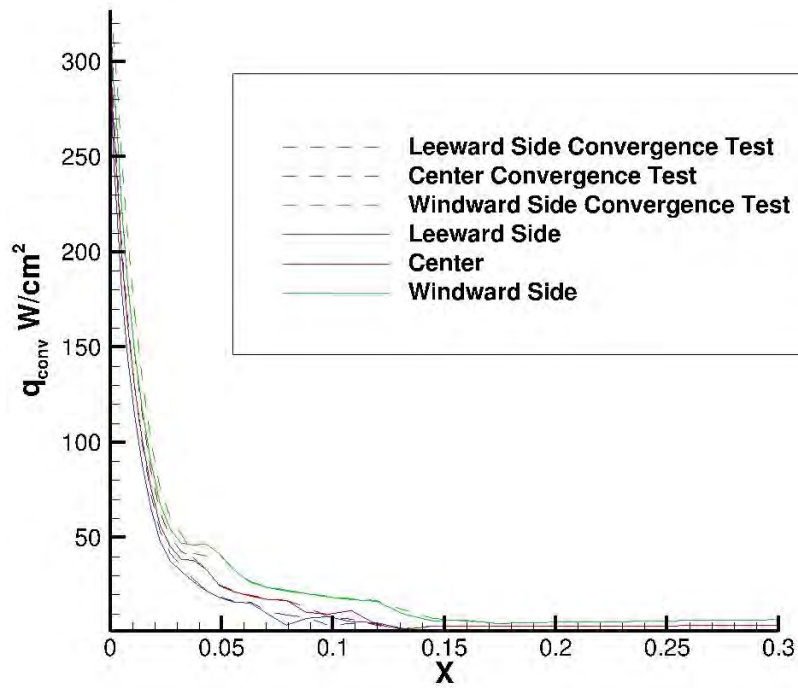Figure 31. Convective Heat Transfer Plot along the Complete Body Length

Figure 32. Convective Heat Transfer Plot along the Nose

The first set of properties analyzed were the thermodynamic properties of the surface of the body including convective heat transfer, temperature, and pressure. Figure 33 and Figure 34 depict the convective heat transfer over the whole surface, while Figure 35 and Figure 36 depict the heat transfer only at the nose. As expected, the highest heat transfer occurred at the nose of the body directly behind the normal shock in the stagnation region. Upon closer inspection, it was noticed that the convective heat transfer was slightly higher on the windward side of the body than the leeward side. This higher heat transfer was due to the slight angle of attack of 5°. The 5° angle of attack caused the leeward side of the body to receive less direct flow therefore causing less convective heat transfer to take place. Finally, it is important to note that the convective heat transfer for the ablating case was significantly lower than it was for the non-ablating case. This lower

61

heat transfer was due to the material ablating away from the surface of the body and shows that the thermal protection system was operating as designed, reducing the convective heat transfer to the body; which in turn increases the survivability and lowers the radiative signature of the body.
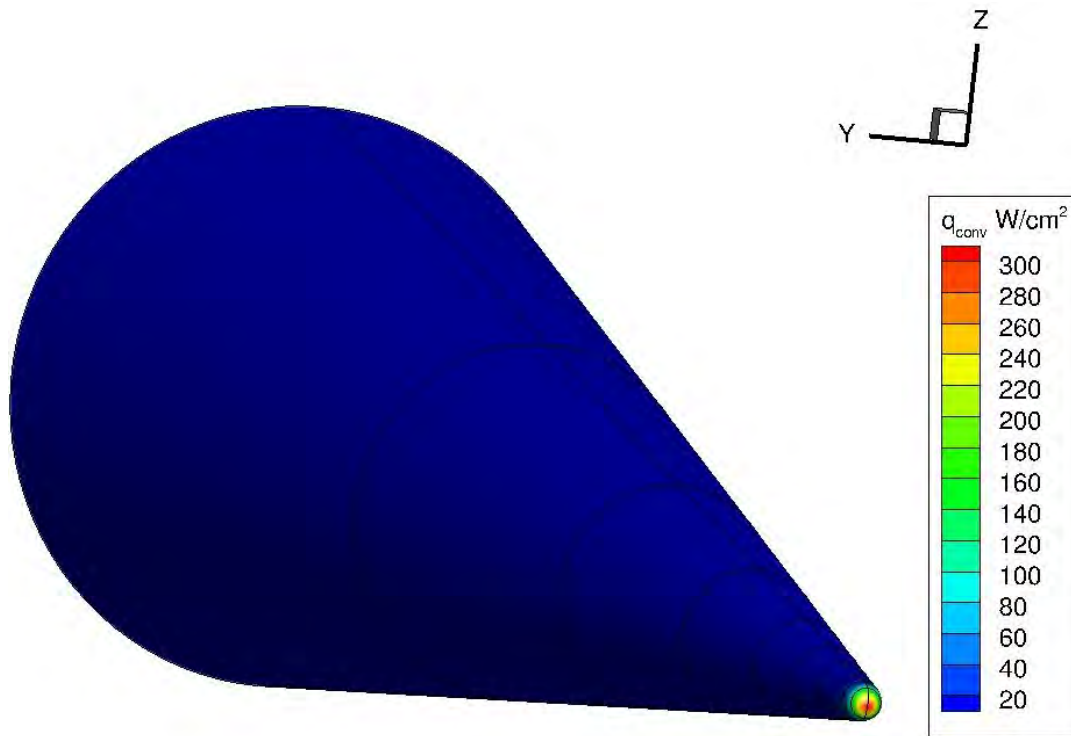
Figure 33. Convective Heat Transfer on the Surface of the Body
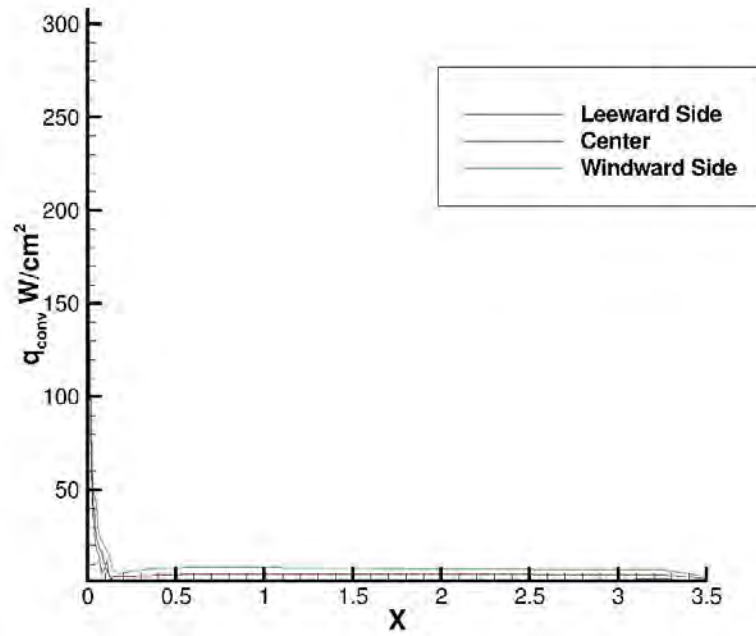
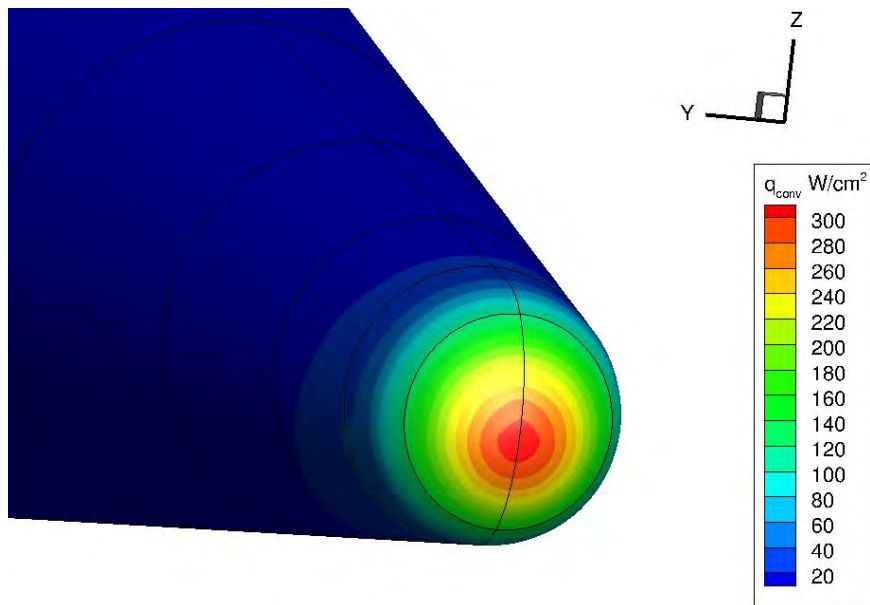Figure 34. Convective Heat Transfer Plot on the Surface of the Body
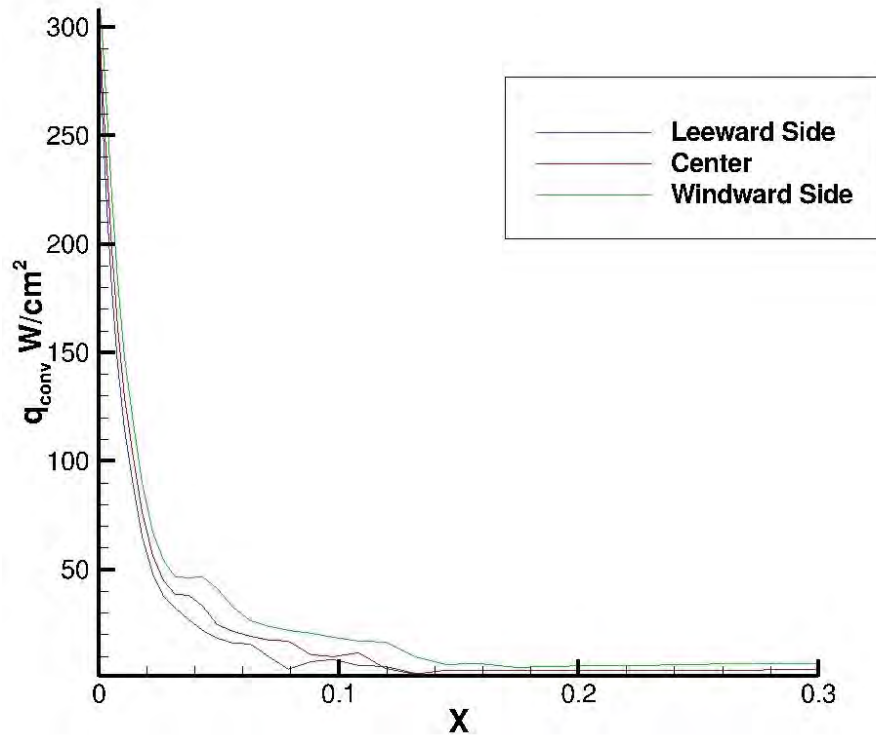

Figure 35. Convective Heat Transfer on the Nose of the Body

Figure 36. Convective Heat Transfer Plot on the Nose of the Body

The next property analyzed was temperature. The temperature profiles are depicted in Figure 37 through Figure 39 with a plot of the temperature profile depicted in Figure 40. The highest temperature was on the nose at the stagnation point. The high temperatures in this location are due to the flow stagnating at this point and also the presence of a normal shock. The angle of attack caused there to be higher temperatures on the windward side of the body when compared to the leeward side, as was previously discussed with convective heat transfer. For any X location on the body the temperature was highest on the windward, then the centerline, and finally coolest on the leeward side of the body. Also, the temperature generally decreases down the length of the body other than a significant drop in temperature right after the nose section. This drop, then a sudden rise in the temperature was caused by an expansion followed by a compression

while transitioning from the nose to the rest of the body. Another noted significant drop

in temperature was at the aft end of the body. This drop in temperature is also due to the

expansion of the flow entering the wake region.
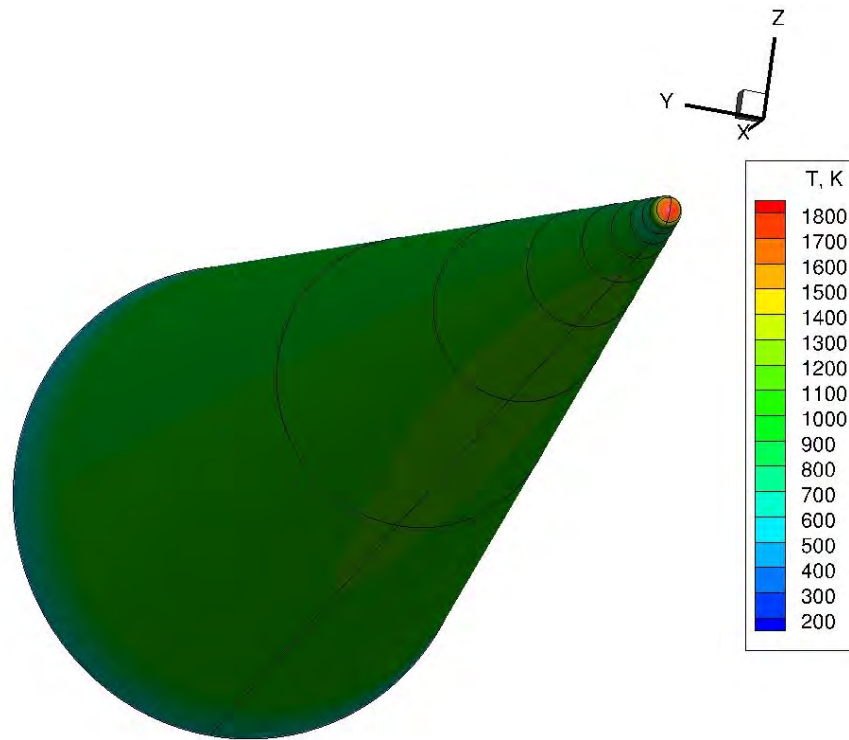
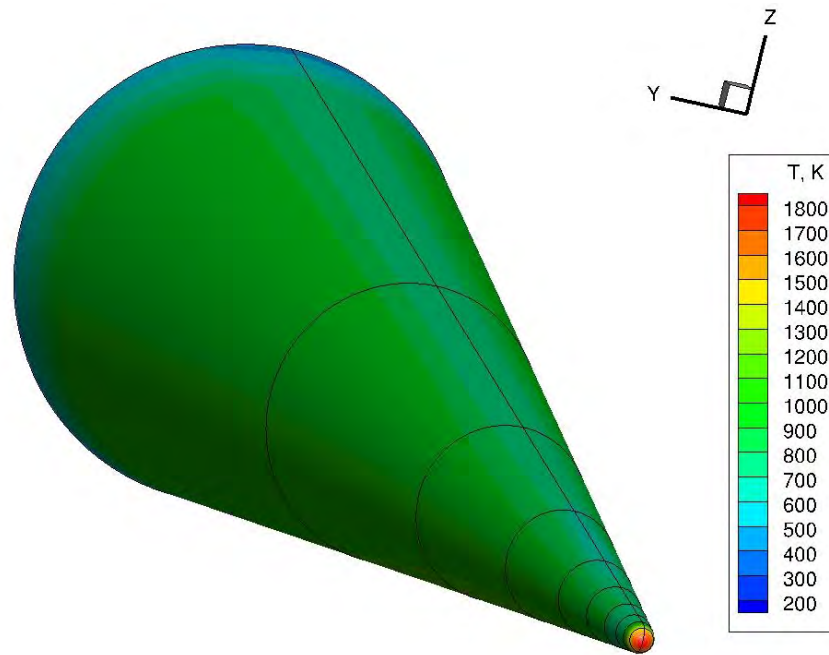Figure 37. Temperature on the Windward Surface of the Body

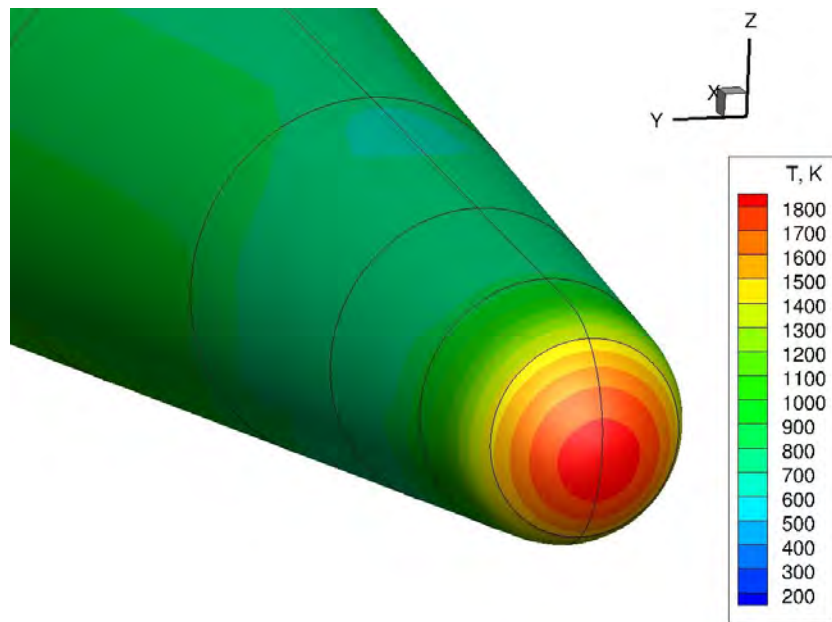Figure 38. Temperature on the Leeward Surface of the Body

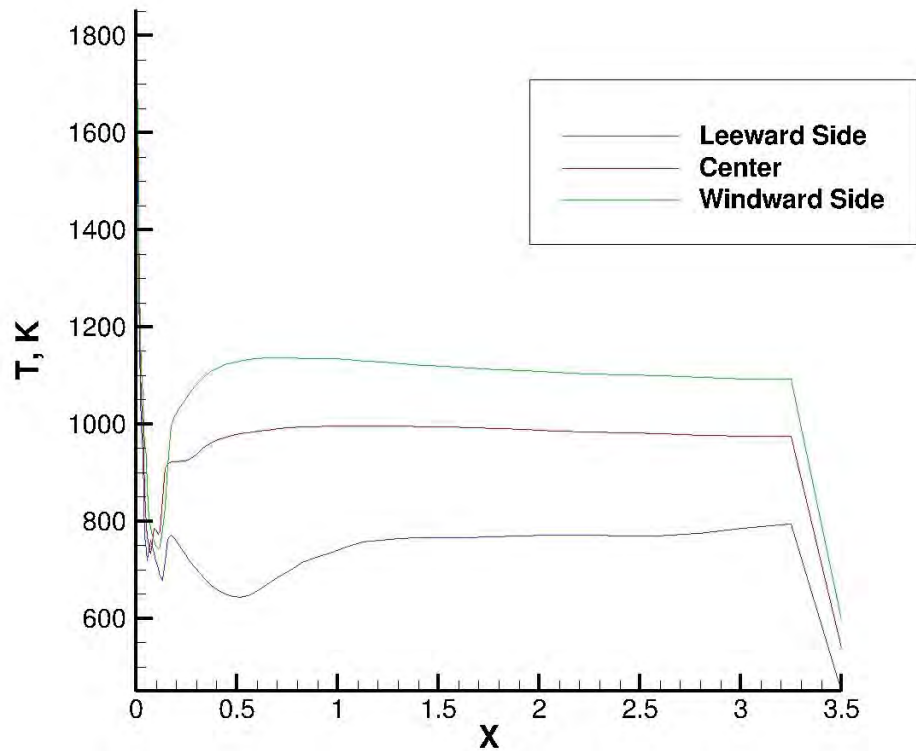Figure 39. Temperature on the Nose of the Body

Figure 40. Temperature Plot on the Surface of the Body

The final thermodynamic surface property analyzed was pressure. The pressure profile is depicted in Figure 41 and Figure 42 along with two plots in Figure 43 and Figure 44. Once again the profiles were as expected, with the highest pressure being at the nose in the stagnation region and decreasing from there. The windward side also had a higher pressure than the leeward side due to the 5° angle of attack and the previously discussed reasons. The pressure had a significant drop off at the end of the body due to a massive expansion as the body ended and the flow entered the wake region. Additionally, for any X location on the body the pressure was highest on the windward side and lowest on the leeward side due to the amount of direct flow the windward side was receiving. All of these results agree with the theories of aerodynamics and were expected.

67
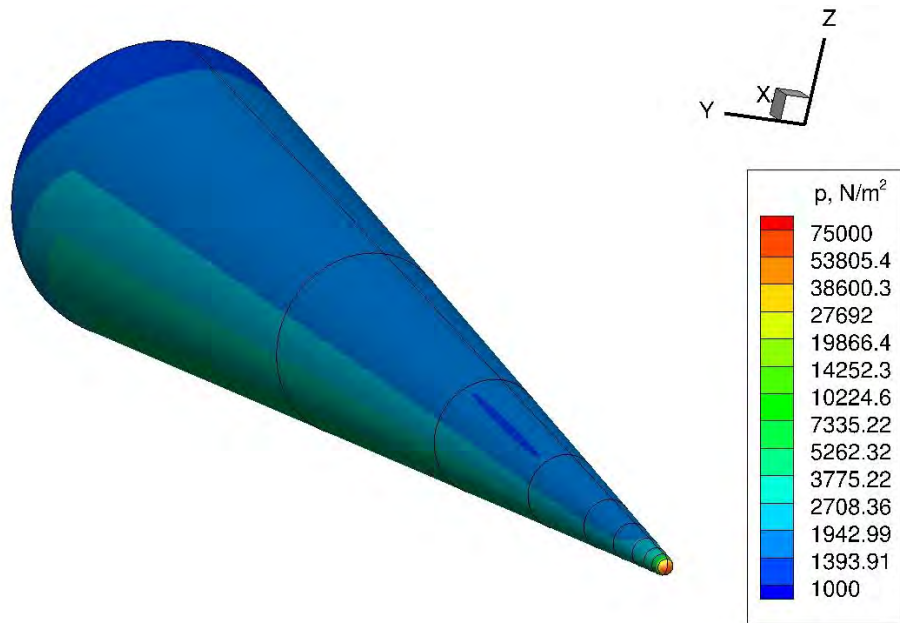
Figure 41. Pressure Profile on the Surface of the Body
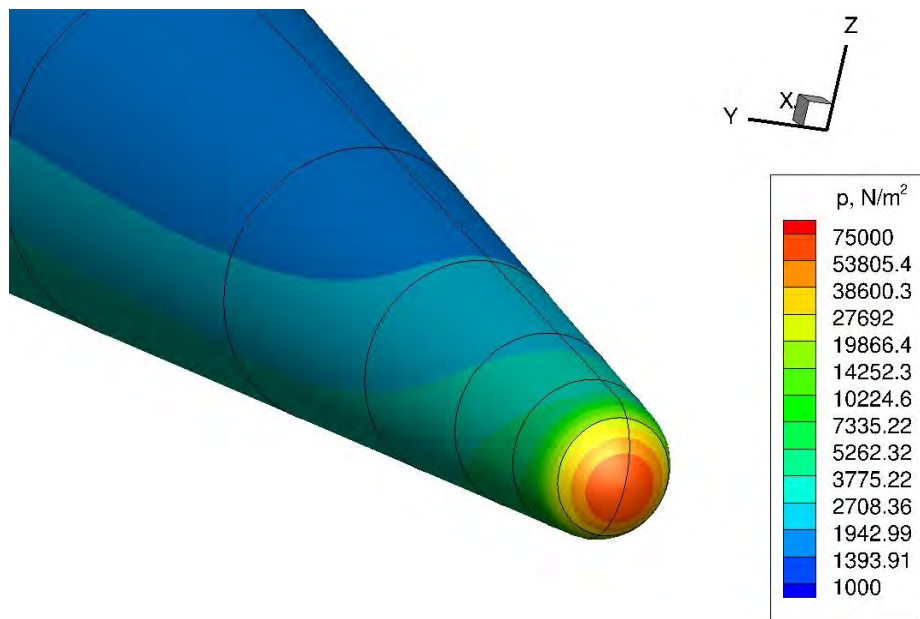

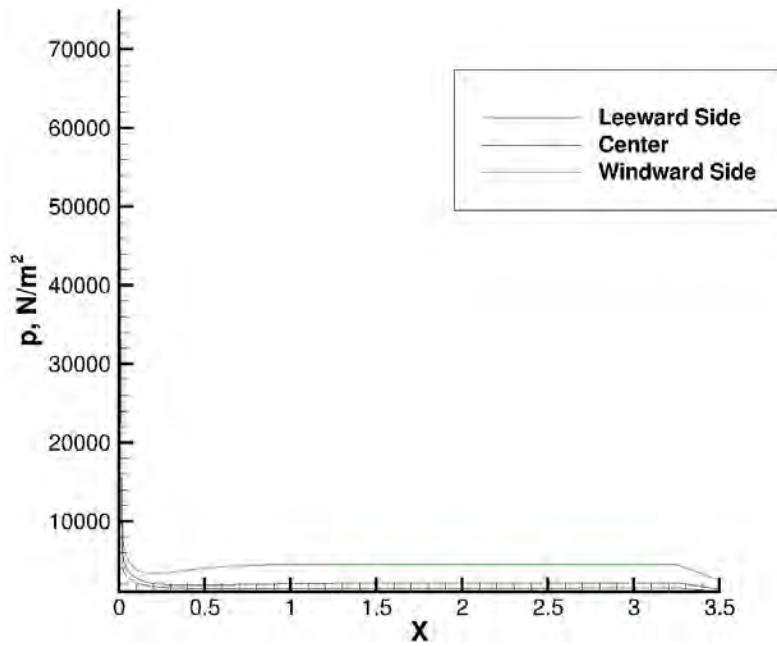Figure 42. Pressure Profile on the Nose of the Body

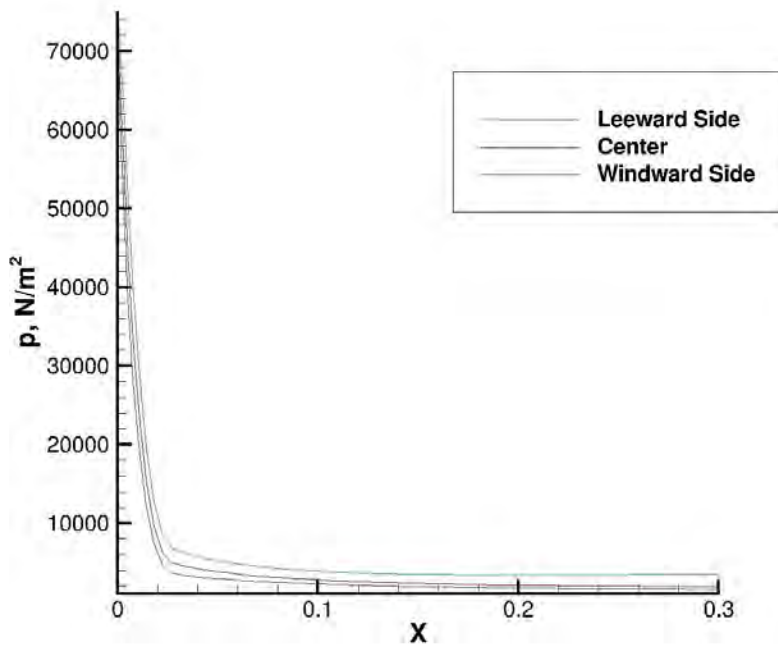Figure 43. Pressure Plot on the Surface of the Body

Figure 44. Pressure Plot on the Nose of Body

The first ablation result analyzed was the mass flow rate (mdot) off of the surface of the body. This value represents the rate that material is ablating from the body into the flowfield. The mass flow rate profile is depicted in Figure 45 and Figure 46, while Figure 47 depicts the plots of the mass flow rate. The highest ablation is occurring at nose because the highest surface temperatures were located there. The ablation was also slightly skewed toward the windward side due to the 5° angle of attack which caused higher temperatures. As expected the ablation for all X locations was highest on the windward side due to the 5° angle of attack. All of the ablation is occurring in the first two blocks of the body which was how the simulation was setup, as previously discussed in Section 3.6. This setup was chosen for the simulation because the surface temperatures outside of the first two blocks were around 1,000 K, which is not hot enough to cause any significant ablation of the carbon heat shield. Upon inspection it was seen that not all of block two was ablating, so the assumption that negligible ablation was occurring in all other of the blocks was valid. With a realistic ablation rate occurring, the chemical species present were ready to be analyzed.
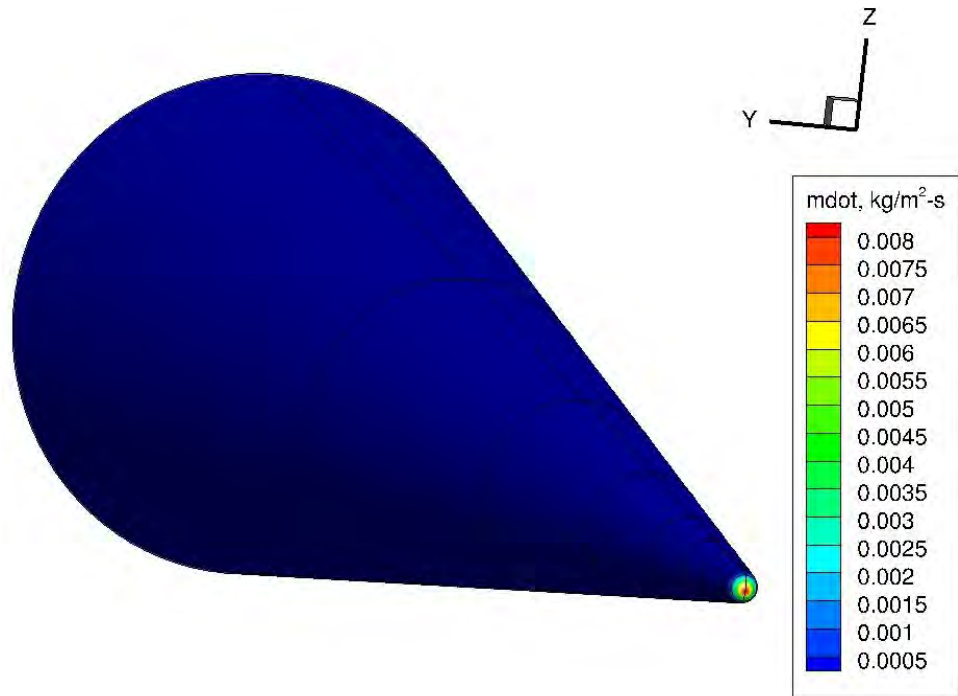
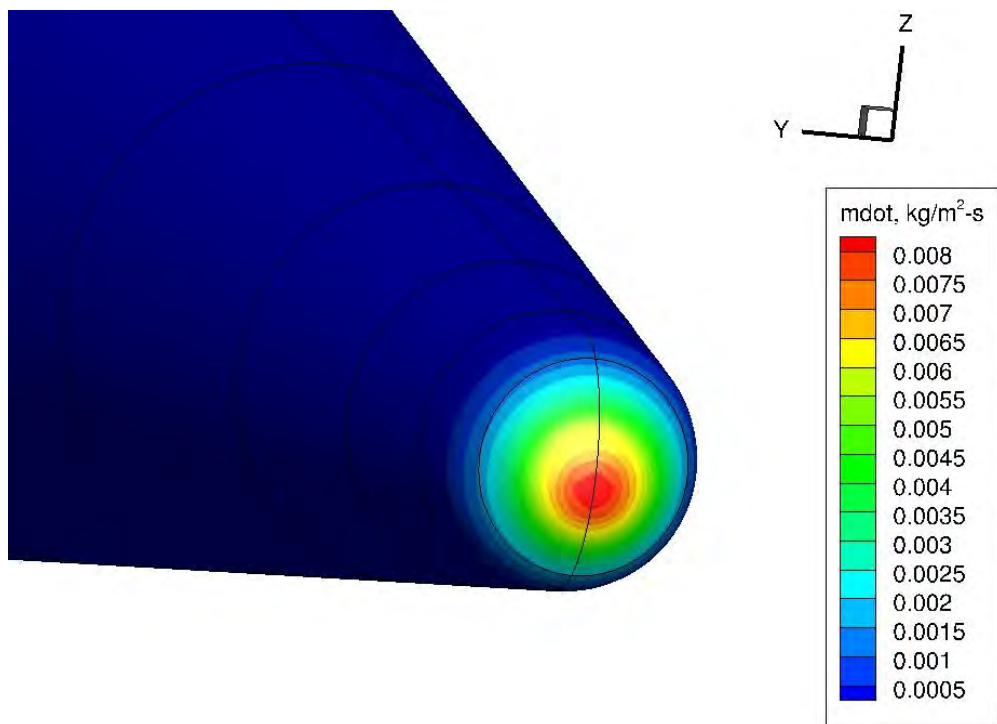Figure 45. Mass Flow Rate Profile of Ablating Material from the Surface of the Body

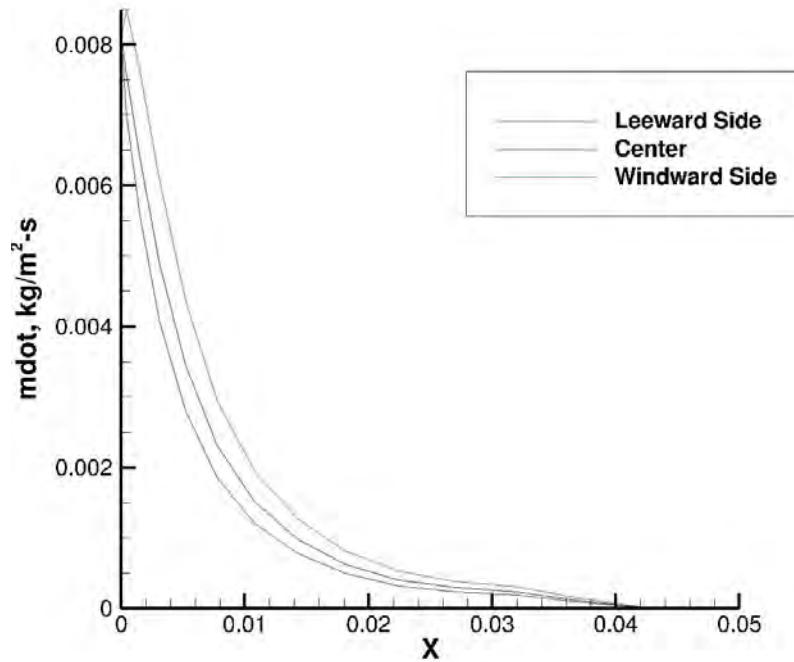Figure 46. Mass Flow Rate Profile of Ablating Material from the Nose of the Body

Figure 47. Mass Flow Rate Plot of Ablating Material from the Nose of the Body

Nitrogen and Oxygen were the first species to be analyzed. They were analyzed in the form of Diatomic Nitrogen (N_2), Diatomic Oxygen (O_2), Monatomic Nitrogen (N), and Monatomic Oxygen (O). Diatomic Nitrogen was seen at close to freestream air concentrations on the surface due to the relatively low temperatures and is depicted in Figure 48 and Figure 49. It is important to note that the concentration of Diatomic Nitrogen drops off dramatically after the first two blocks. This decrease in Diatomic Nitrogen is purely an artifact of ablation not occurring in the remaining blocks. The simulation does not take the air species into account at the surface of the remaining blocks because of this as well. The same result was seen for Diatomic Oxygen and these profiles can be seen in Appendix B: Supplemental Results. Monatomic Nitrogen was present in very small concentrations at the nose only, as depicted in Figure 50 and Figure 51. The nose region was the only place that temperatures were hot enough to dissociate

the Diatomic Nitrogen from the atmosphere into Monatomic Nitrogen. This meant that there would not be a significant amount of Monatomic Nitrogen to form complex molecules. Similar results were found with Monatomic Oxygen; only dissociating right at the nose of the body. For this reason the Monatomic Oxygen profiles are not included here but can be found in Appendix B.
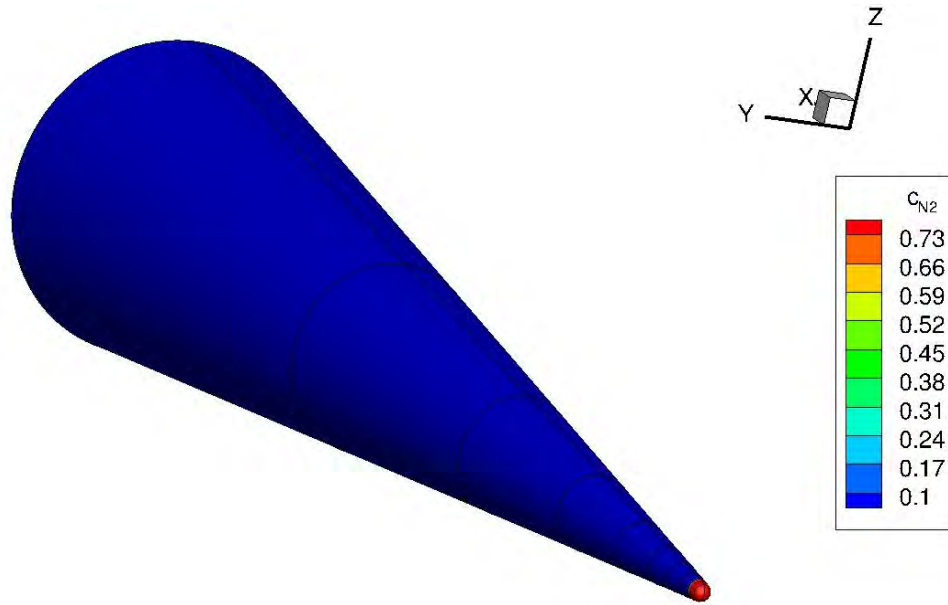

Figure 48. Mass Fraction of Diatomic Nitrogen on the Surface of the Body
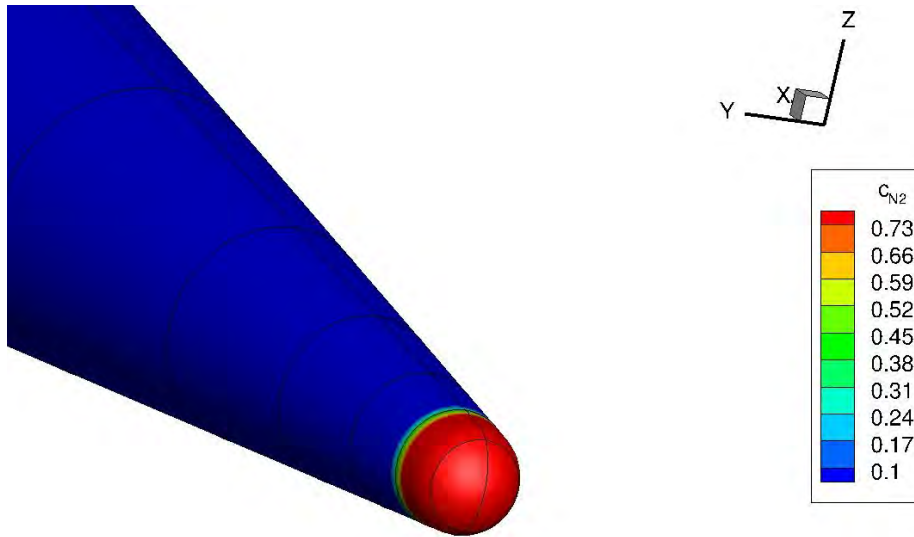
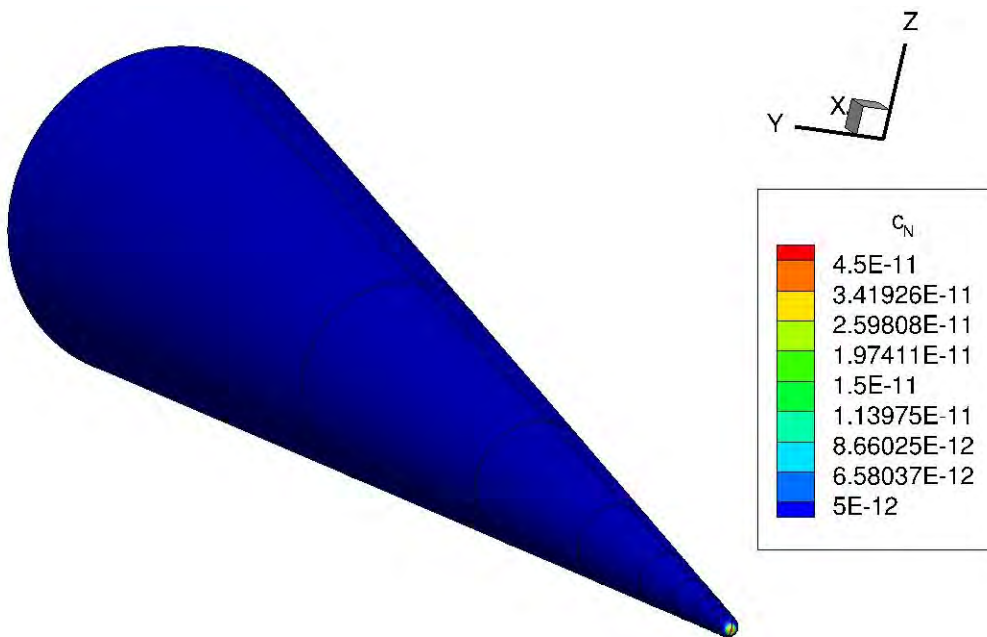Figure 49. Mass Fraction of Diatomic Nitrogen on the Nose of the Body

Figure 50. Mass Fraction of Monatomic Nitrogen on the Surface of the Body
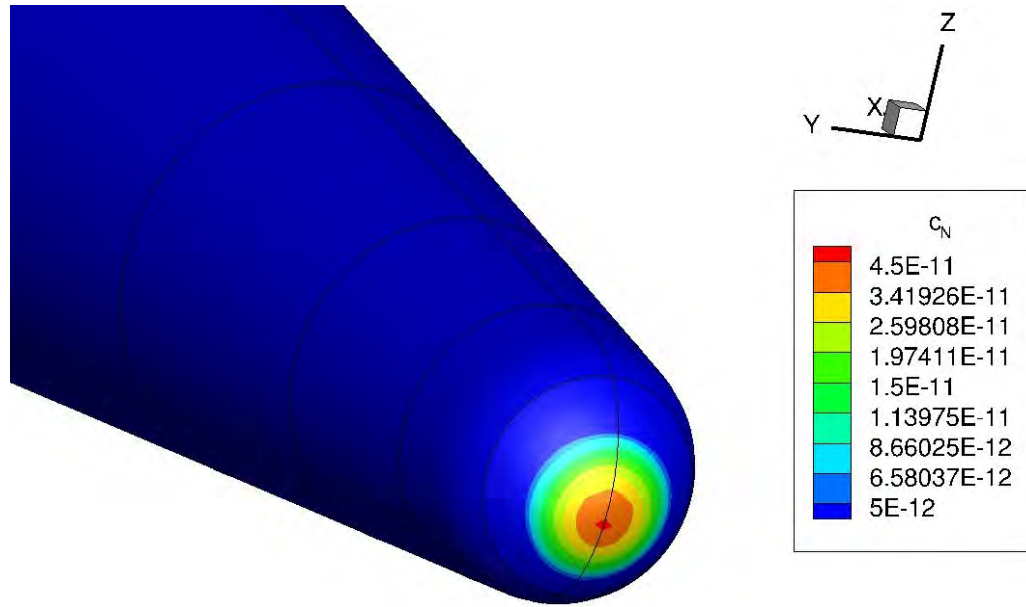
Figure 51. Mass Fraction of Monatomic Nitrogen on the Nose of the Body

Nitric Oxide (NO), Nitrosonium ion (NO+), and electrons (e-) were the next species analyzed. Nitric Oxide forms when Diatomic Nitrogen and Oxygen dissociate and high temperatures are present to facilitate the bonding of a Nitrogen atom and an Oxygen atom. All of the required conditions for the formation of Nitric Oxide are present at the nose of the body and is the only place that Nitric Oxide was formed. Even though Nitric Oxide was only form right at the tip of the nose it was the most common product present in the simulation and therefore was extremely important to track. The Nitric Oxide distribution is depicted in Figure 52 and Figure 53. Nitrosonium ions are formed when a Nitric Oxide molecule collides with another molecule; the Nitric Oxide molecule loses an electron therefore becoming a Nitrosonium ion. These free electrons collide with other Nitric Oxide molecules causing more Nitrosonium ions to be present with an exponential increase. Even though Nitrosonium ions are forming, they are in very small concentrations as depicted in Figure 54 and Figure 55. The electron number density is

exactly the same as the Nitrosonium ion number density since all of the electrons present were due to the formation of a Nitrosonium ion; for this reason the electron results are presented in Appendix B. Even though electrons are in a small concentration they can have a significant impact on radar cross sections when they are in a high density. Due to this effect electrons number density will be tracked when examining the wake.
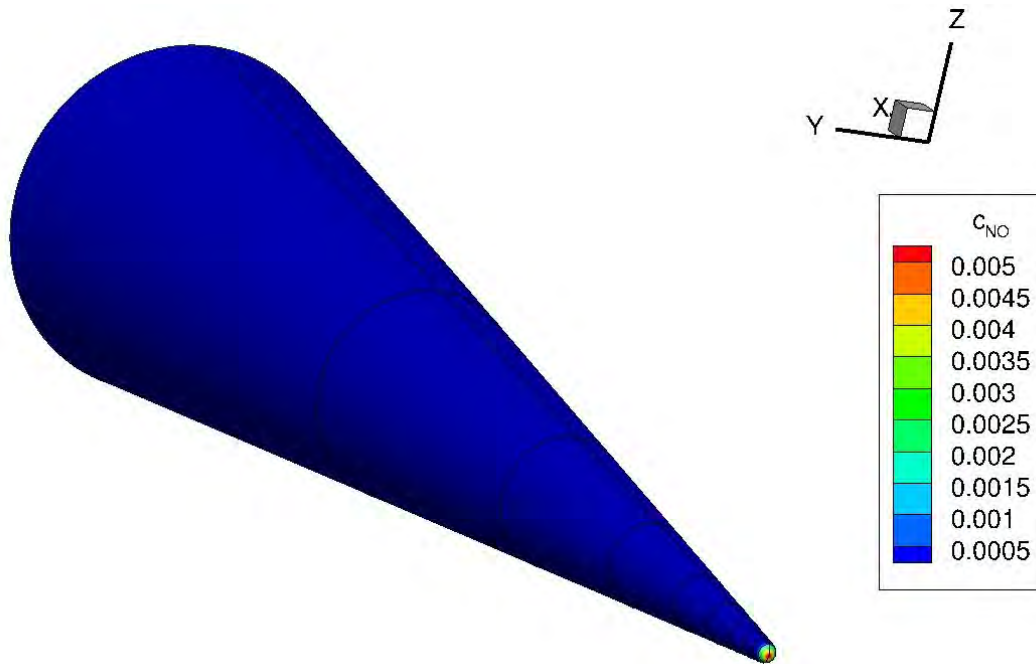

Figure 52. Mass Fraction of Nitric Oxide on the Surface of the Body
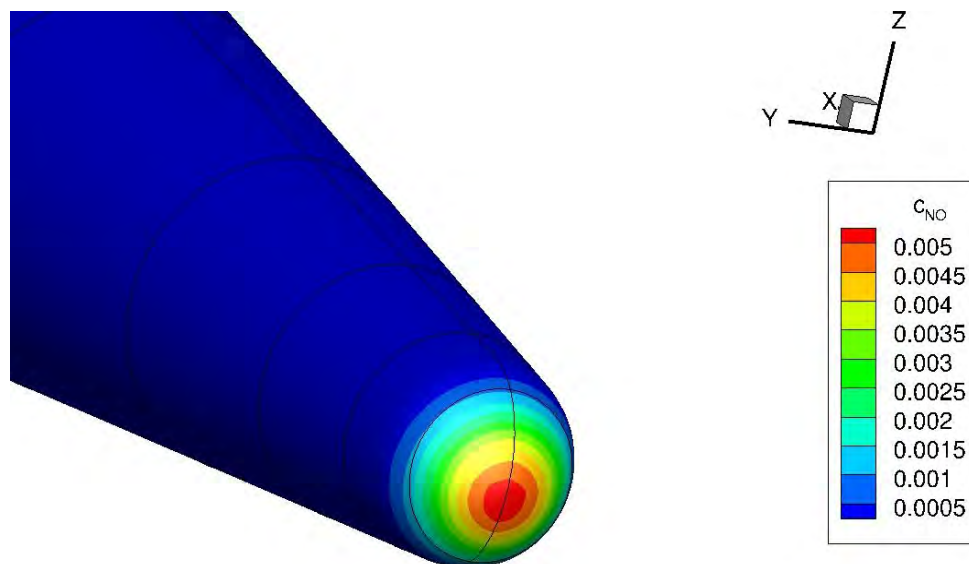
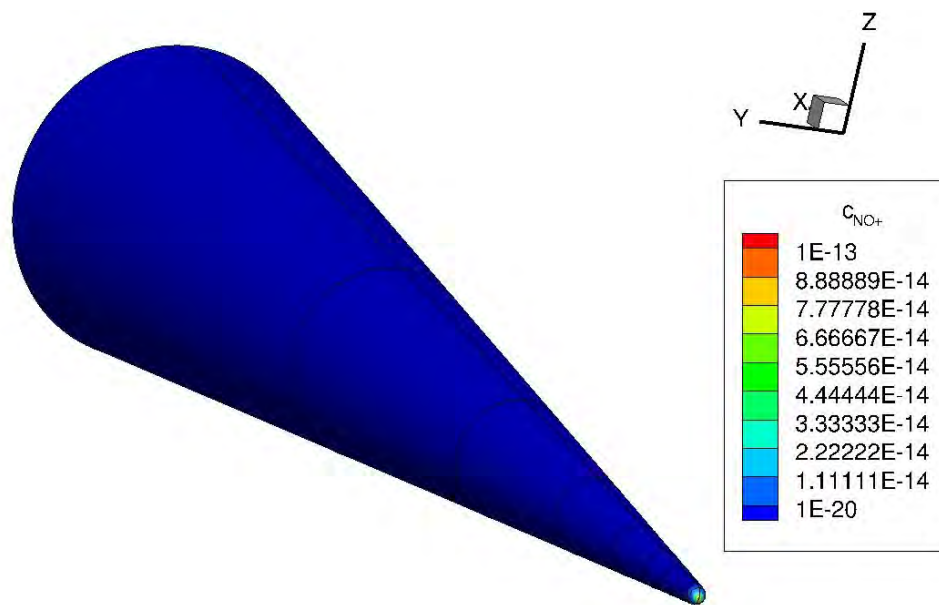Figure 53. Mass Fraction of Nitric Oxide on the Nose of the Body

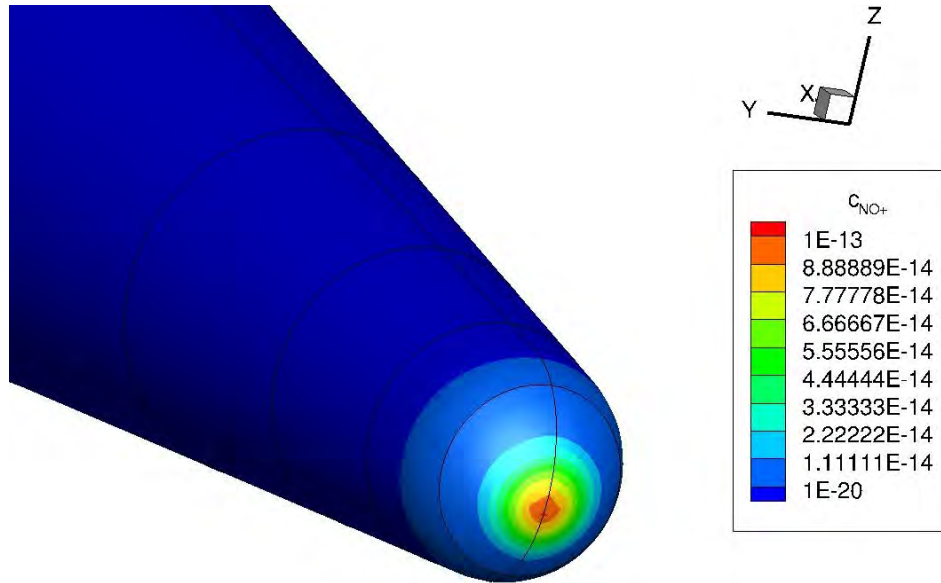Figure 54. Mass Fraction of Nitrosonium on the Surface of the Body

Figure 55. Mass Fraction of Nitrosonium on the Nose of the Body

The next species analyzed were carbons, including Carbon (C), Diatomic Carbon (C_2) and Triatomic Carbon (C_3), and Cyanide (CN). There was almost no pure carbon present in the simulation due to effectively no sublimation occurring because of the relatively low temperatures. Sublimation occurs at temperatures above 3,000 K and the maximum surface temperature in this simulation was 1,800 K. The profiles of Triatomic Carbon are depicted in Figure 56 and Figure 57. Profiles of Carbon and Diatomic Carbon show similar results that can be found in Appendix B. Cyanide was essentially not present at all in this simulation as depicted in Figure 58 and Figure 59. Temperatures and pressures were not high enough anywhere on the surface of the body, including the nose region, to cause the bonding of Carbon and Nitrogen.
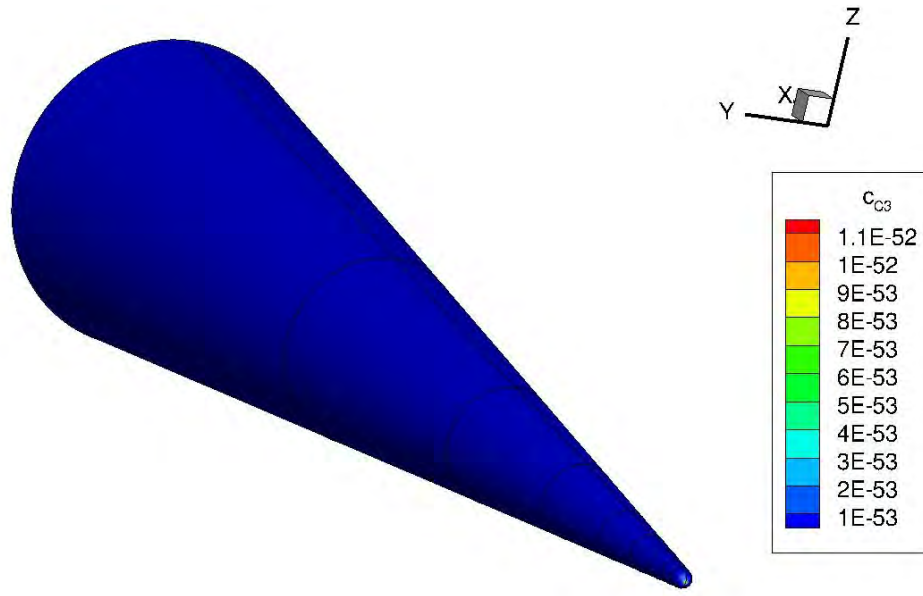
Figure 56. Mass Fraction of Triatomic Carbon on the Surface of the Body
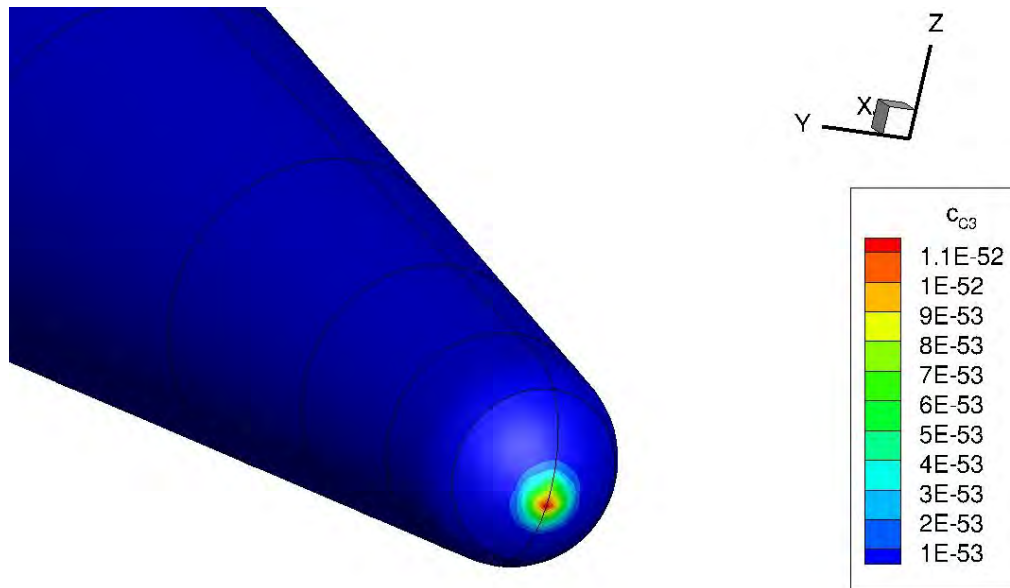

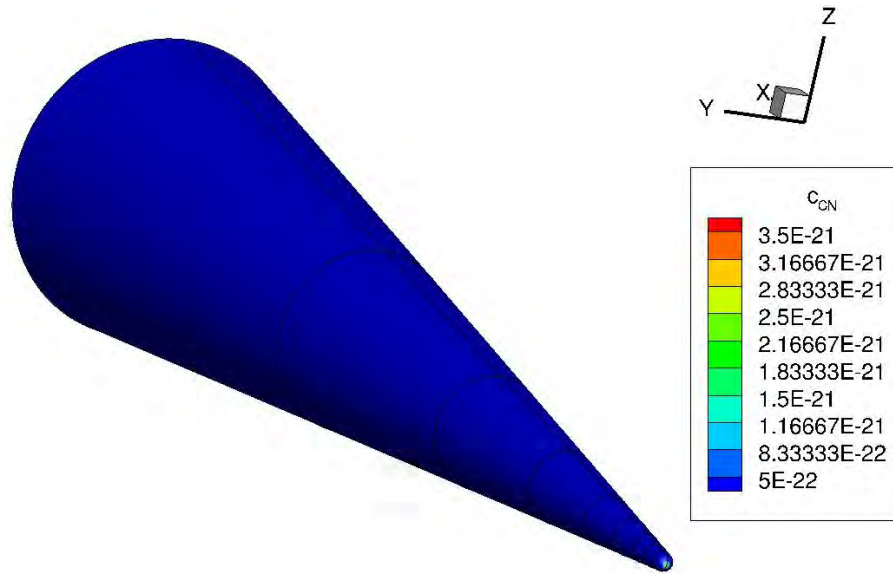Figure 57. Mass Fraction of Triatomic Carbon on the Nose of the Body

Figure 58. Mass Fraction of Bonded Carbon and Nitrogen on the Surface of the Body

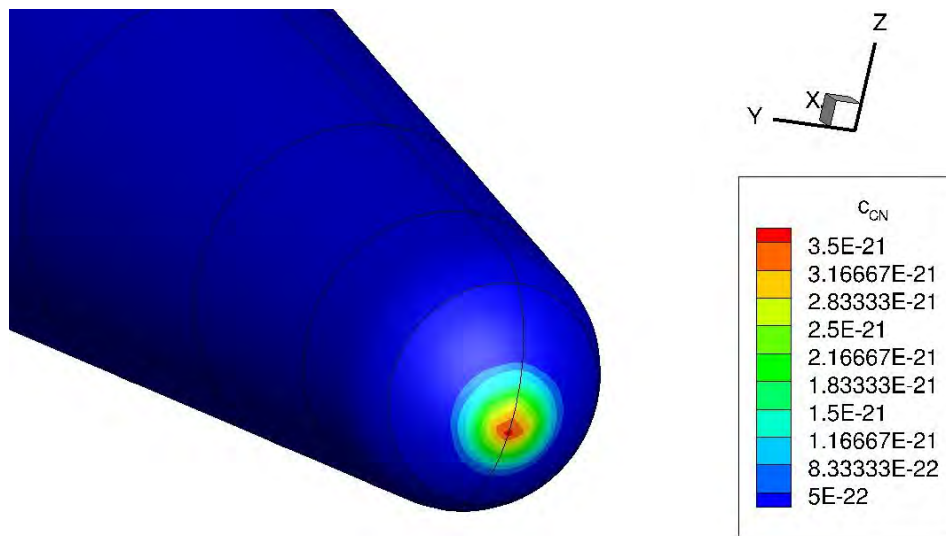Figure 59. Mass Fraction of Bonded Carbon and Nitrogen on the Nose of the Body

The final species analyzed were Carbon Dioxide (CO_2) and Carbon Monoxide (CO). Carbon Dioxide is formed from a Monatomic Oxygen atom combines with ablated Carbon from the surface of the body forming Carbon Monoxide. This molecule leaves the surface and bonds with another Monatomic Oxygen forming Carbon Dioxide. This

molecule is forming over the entire nose region and down into the body. However, is the second most common product in the simulation, only to Nitric Oxide, but is the most common ablative species present and will therefore be important to track in the wake. The concentration of Carbon Dioxide is depicted in Figure 60 and Figure 61. Carbon Monoxide is only formed when there is not enough Monatomic Oxygen to form Carbon Dioxide as discussed in the formation of Carbon Dioxide. Since there is an abundance of Monatomic Oxygen in comparison to the amount of Carbon present, there is very little Carbon Monoxide that was formed. The concentration of Carbon Monoxide is depicted in Figure 62 and Figure 63.
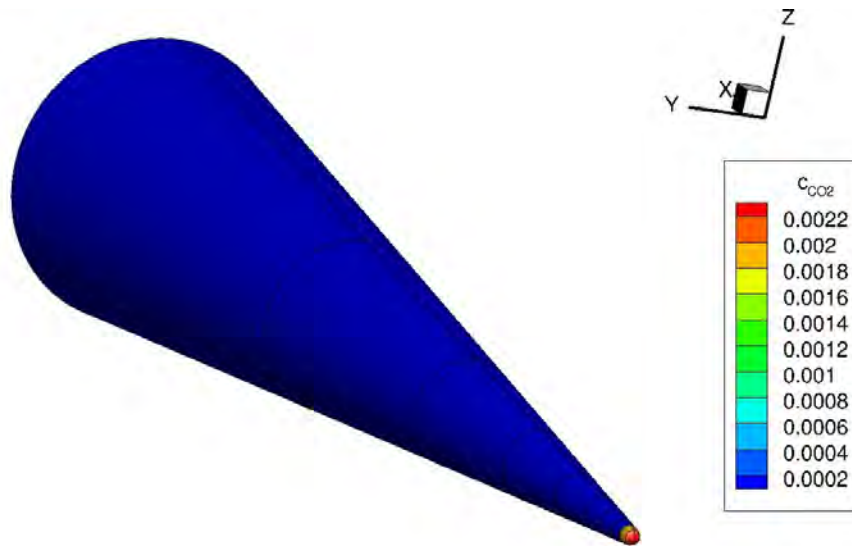

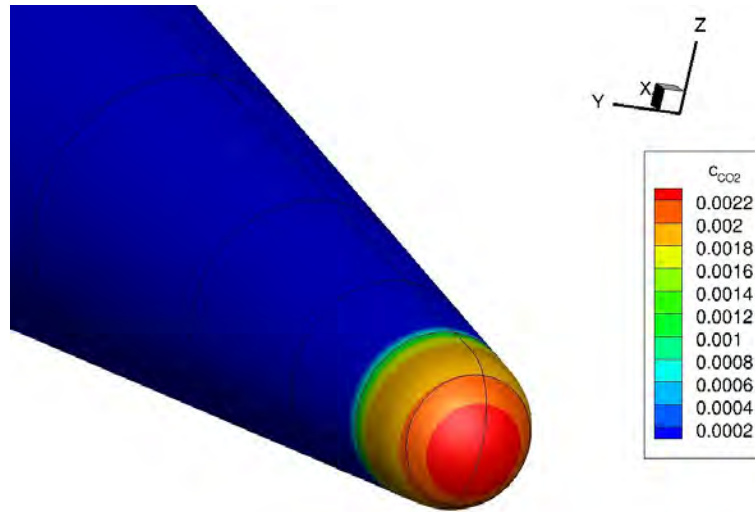Figure 60. Mass Fraction of Carbon Dioxide on the Surface of the Body

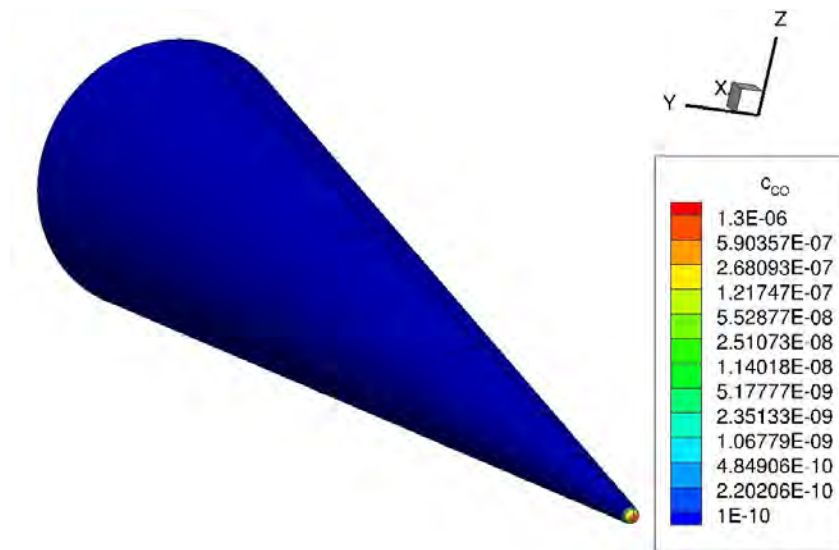Figure 61. Mass Fraction of Carbon Dioxide on the Nose of the Body

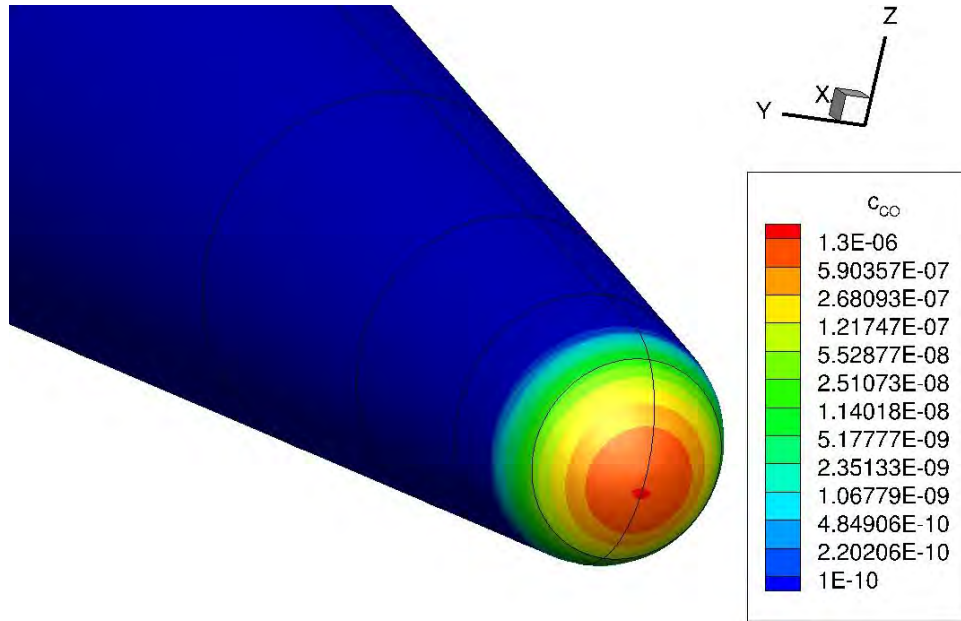Figure 62. Mass Fraction of Carbon Monoxide on the Surface of the Body

Figure 63. Mass Fraction of Carbon Monoxide on the Nose of the Body

After analyzing all of the species present on the surface of the body, it was discovered that only Nitric Oxide and Carbon Dioxide were present in any substantial quantity. The low quantity of the other species was due to the relatively low temperatures present at the surface of the body. These temperatures were not high enough to cause significant disassociation of Diatomic Nitrogen or Diatomic Oxygen other than in the nose region. Along with the low amount of disassociation, there was minimal ablation and no sublimation present with the carbon thermal protection shield. All of the Carbon that ablated from the surface was used in the formation of Carbon Monoxide and Carbon Dioxide as previously seen. Similarly, all of the dissociated Nitrogen was used in the formation of Nitric Oxide. Due to these facts, the main species of interest when looking at the flowfield will be Nitric Oxide and Carbon Dioxide. Free electrons will also be of interest due to electron effects on radar cross sections.

4.3. Flowfield Results

With the surface results analyzed it was time to move to analyzing the flowfield. The non-ablating results of velocity streamlines, temperature, density, and vibrational energy were analyzed first. The first step was to look at the results from the simulations for agreement with the hypersonic wake phenomena discussed in Section 2.5. As a reminder to the reader, there were five phenomena that characterized the wake region including: a flow expansion over the shoulder of the body, recirculating flow in the base region of the body, a neck-stagnation point, a flow expansion from the neck, and a weak neck recompression shock. In order to help analyze these phenomena, velocity streamlines were plotted over the entire flowfield and are depicted in Figure 64 and Figure 65. The first two phenomena, flow expansion over the shoulder of the body and recirculating flow in the base region of the body, are clearly presented by the velocity streamlines. The expansion was depicted by the streamlines being very compact until reaching the shoulder of the body then expanding once they passed the shoulder. The recirculating flow was shown by the streamlines curling in on themselves in the base region. Since this is not a steady state effect, the result will change with every iteration of the simulation. Regardless of this fact, recirculating flow was clearly present. Unfortunately, the other three phenomena, a neck-stagnation point, a flow expansion from the neck, and a weak neck recompression shock, were not captured in this simulation. Park stated that the neck stagnation point is normally located about two or three body diameters downstream of the shoulder [16]. However, this was for a sphere which has a slenderness ratio of one. Since a blunted cone, which has a much higher slenderness ratio, was used for this study, the effects in the wake were not as dramatic.

84

These less dramatic effects in the wake do not mean the other three phenomena are not present; it is theorized that they are just further down from the body than was included in this research and is supported by once again looking at the velocity streamlines. After the expansion region over the shoulder of the body, the streamlines are beginning to reconverge and compress into the neck region. If the wake region had been extended further the last three phenomena would more than likely be present. Additionally, it was seen that there was a discontinuity down then center of the wake. This discontinuity was due to a pole grid being used and was expected. The discontinuity did not significantly impact the results since it only applies on either side of the pole grid and does not extend into the wake region.
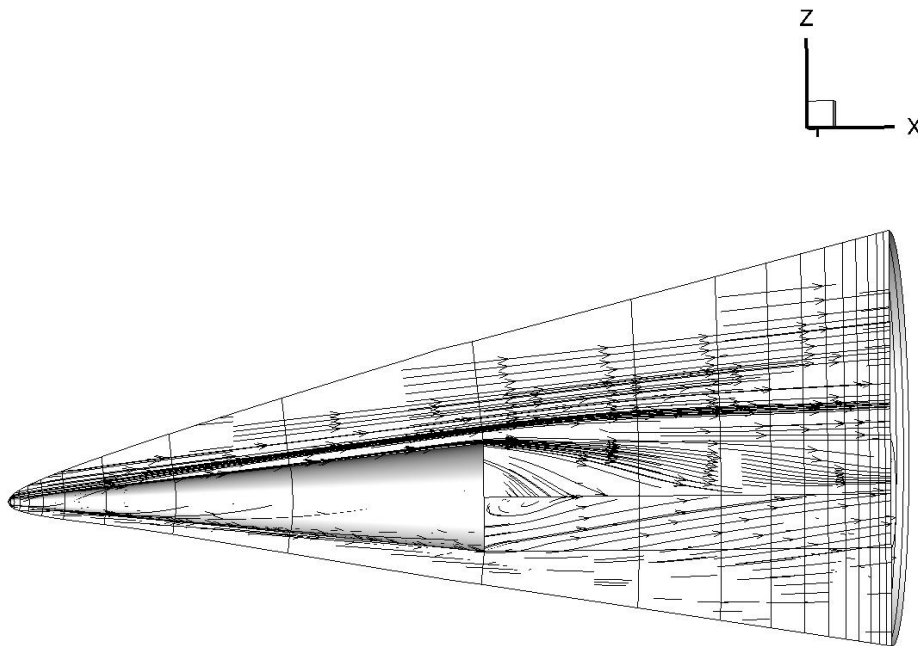

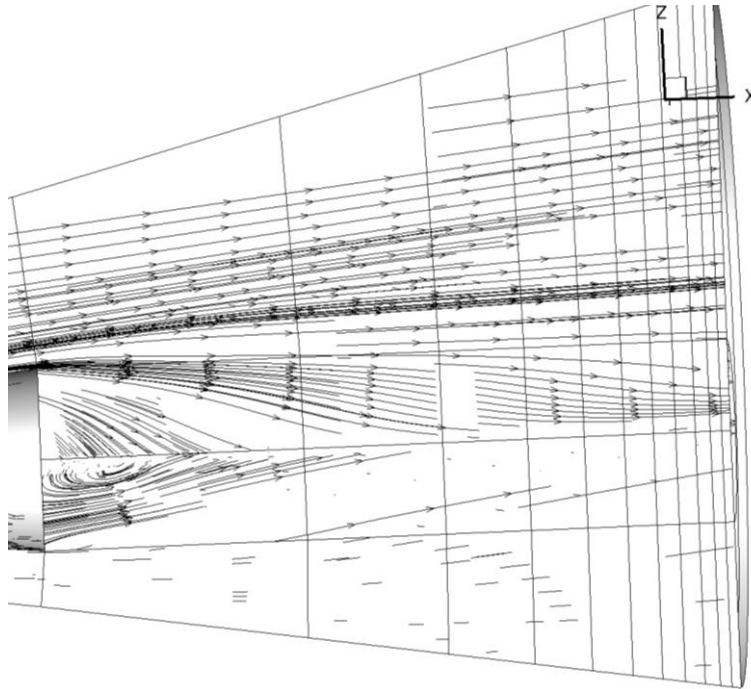Figure 64. Velocity Streamlines in the Flowfield

Figure 65. Velocity Streamlines in the Wake

The temperature profiles were examined next and are depicted in Figure 66 through Figure 68. As expected, the highest temperatures were present at the nose of the body in the region of the normal shock, which agrees with the surface temperature profile. However, there were three interesting observations that need to be addressed, the first being the cool region at the base of the body. Park had stated that the recirculating flow in this region was almost as hot as the stagnation point, but clearly that was not the case with these results [16]. The lack of a higher temperature recirculating flow was due to two facts: the high slenderness ratio and the relatively low hypersonic Mach number. The high slenderness ratio meant there was not a dramatic expansion at the shoulder pulling the hot gasses into the recirculating region. The relatively low hypersonic Mach number caused the flow to be on the cooler end of other hypersonic flows. This lower Mach number meant the gases that were being pulled in could not heat the surrounding

86

area as much, causing the entire area to be significantly cooler. The second observation that needed to be addressed was the cool region under the core wake flow. This area of cool flow is an area of expanding flow and agrees with Park's results. The third and final area that needed addressed was that of increasing temperature in the core wake flow. This temperature increase was due the recompression of the gasses as the streamlines begin to converge. As seen in Figure 68, the temperatures in the core of the wake are approaching 1,600 K which is only an 11% difference from the temperature of the stagnation point at the nose. This high temperature could cause a massive amount of energy to be put into the gases at this point in the wake possibly releasing radiation that could be detected and tracked. If the wake region was extended, it is assumed the temperature would continue to rise as it approached a neck-stagnation point. As a note to the reader, the voided areas in the slices in Figure 68 are where the body is located; this fact remains the same for all figures with slices.
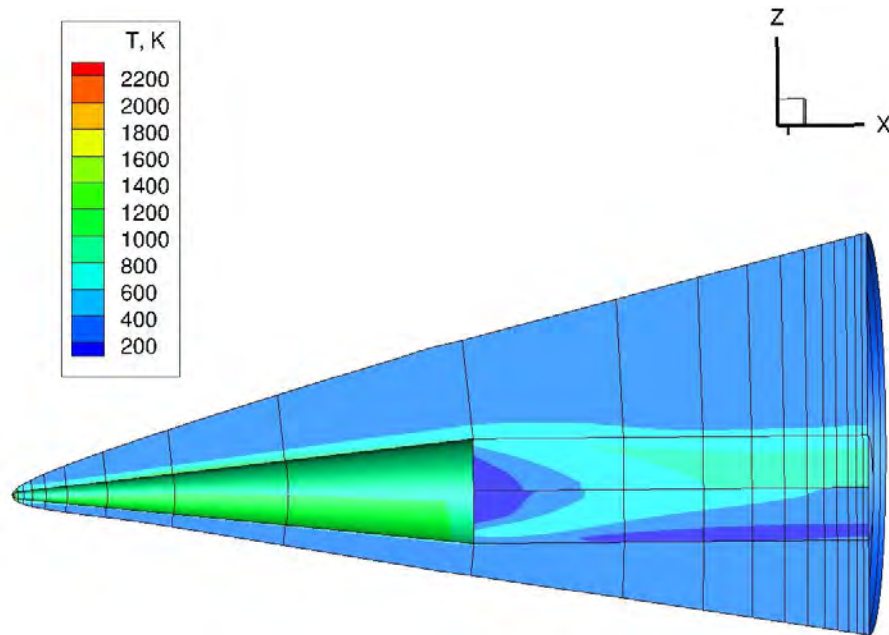

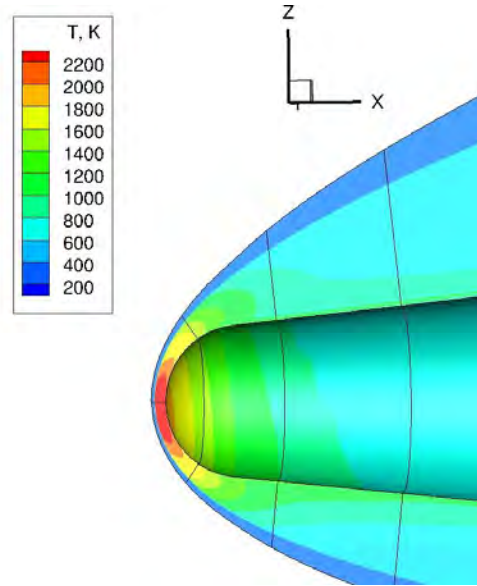Figure 66. Temperature Profile in the Flowfield

Figure 67. Temperature Profile at the Nose
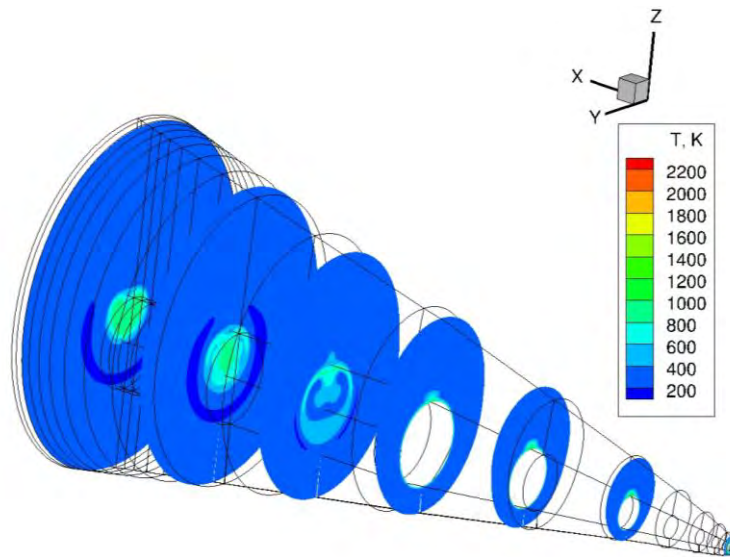
Figure 68. Temperature Profile throughout the Flowfield

The density results, also as expected, showed the highest density at the nose and on the windward side of the body as depicted in Figure 69 though Figure 71. The density presented in these figures is a non-dimensionalized representation of the local density divided by the freestream density. The higher density region at the base of the body is caused by the recirculating flow in this region. The low density flow outside of the

recirculating area is caused by the flow expanding as it passes over the shoulder of the body. However, this region of low density is becoming smaller the further it travels into the wake where the streamlines begin to converge, approaching the neck of the wake.
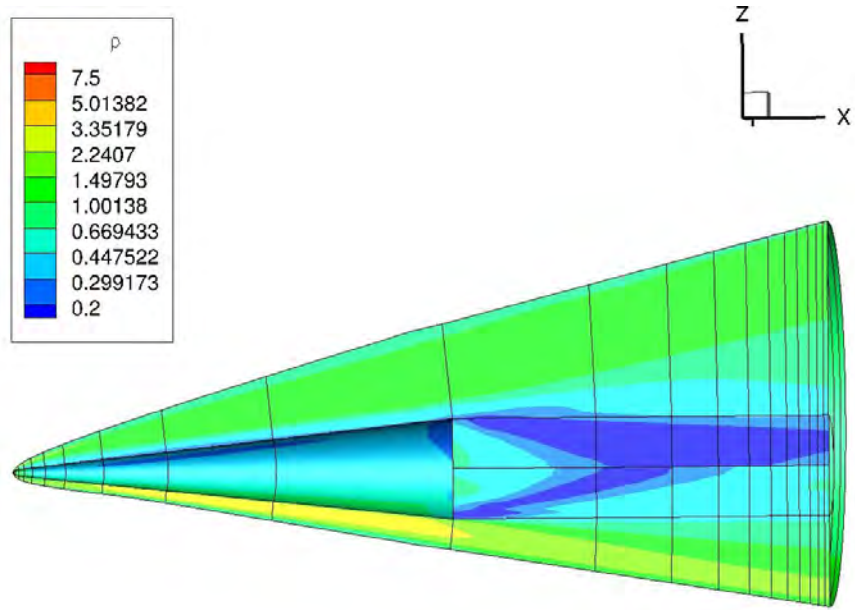

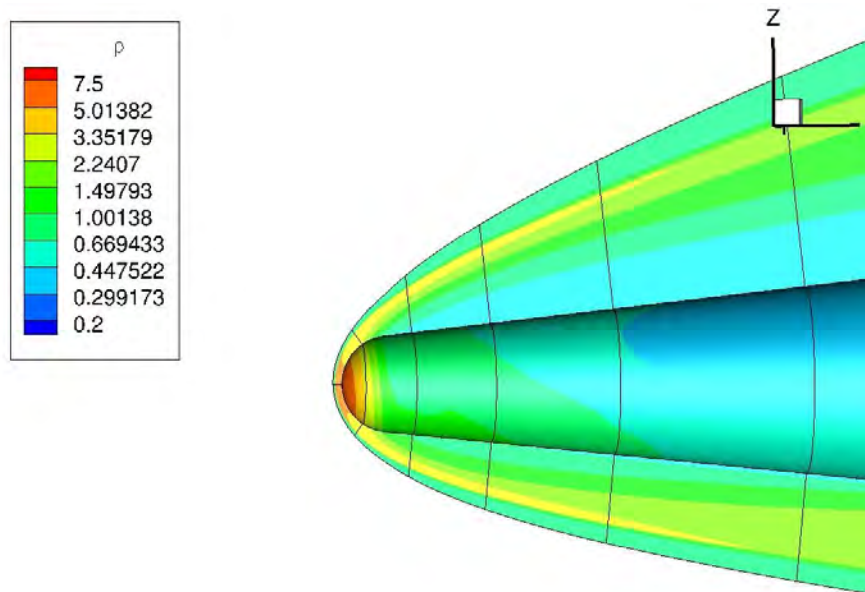Figure 69. Density Profile in the Flowfield

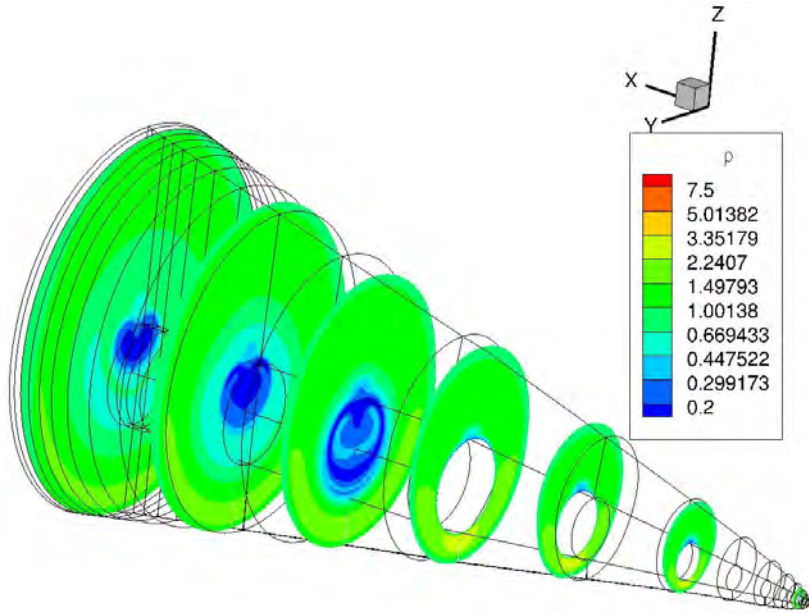Figure 70. Density Profile at the Nose

Figure 71. Density Profile throughout the Flowfield

The final thermodynamic property analyzed was the vibrational temperature. Vibrational temperature represents the excitation of the vibrational modes of a molecule and is an important property when dealing with statistical thermodynamics. Vibrational temperatures of molecules have a direct correlation to this research because of their emissivity. The emissivity of a molecule's vibrational mode can be seen in the infra-red spectrum. The profile of the vibrational temperature in the flowfield is depicted in Figure 72 and Figure 73. The vibrational mode becomes very excited at the nose due to the high temperatures in this area, but the energy decreases as the flow moves out of this area, and the excited molecules begin to collide. As the molecules collide, they begin to lose their vibrational energy. While this was expected, there was an unforeseen result when comparing the vibrational temperature with temperature of the flowfield. In the first 1.5 body diameters of the core flow, the local vibrational temperature was higher than local the temperature of the flowfield, 800 K and 600 K respectively. This higher temperature

is depicted in Figure 74 and is important to note because the higher energy in the vibrational mode could be a possible source of detection in the infra-red band but this would only be true within a few body diameters where the vibrational mode is in a higher state of excitement.
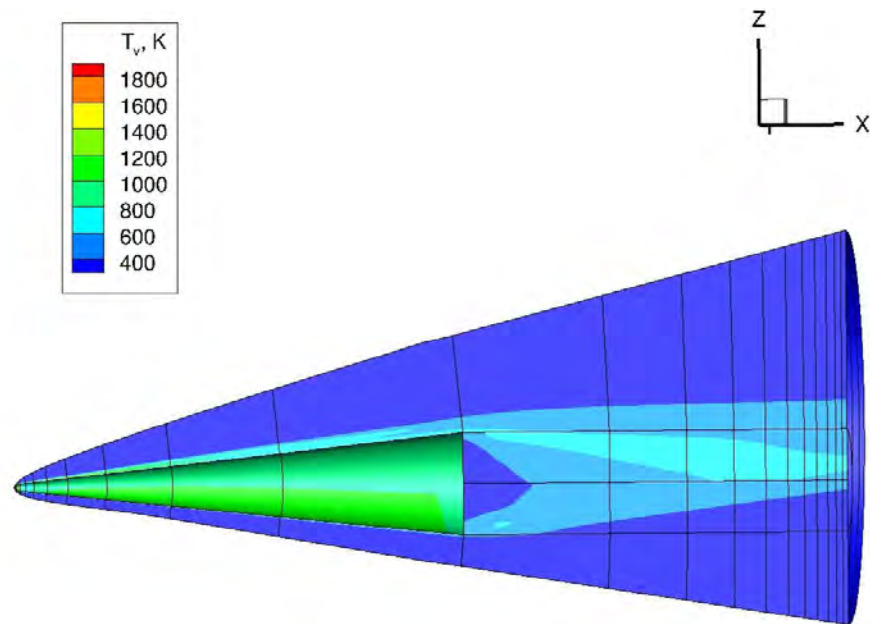
Figure 72. Vibrational Temperature Profile throughout the Flowfield
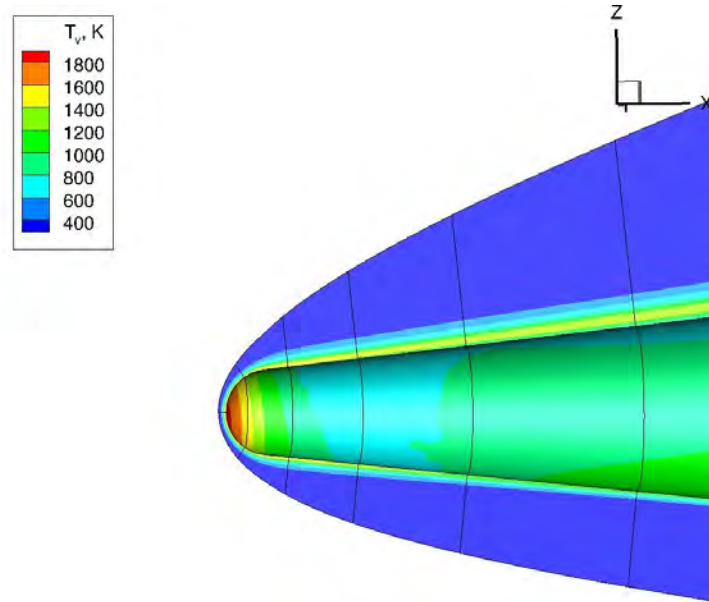
Figure 73. Vibrational Temperature Profile at the Nose
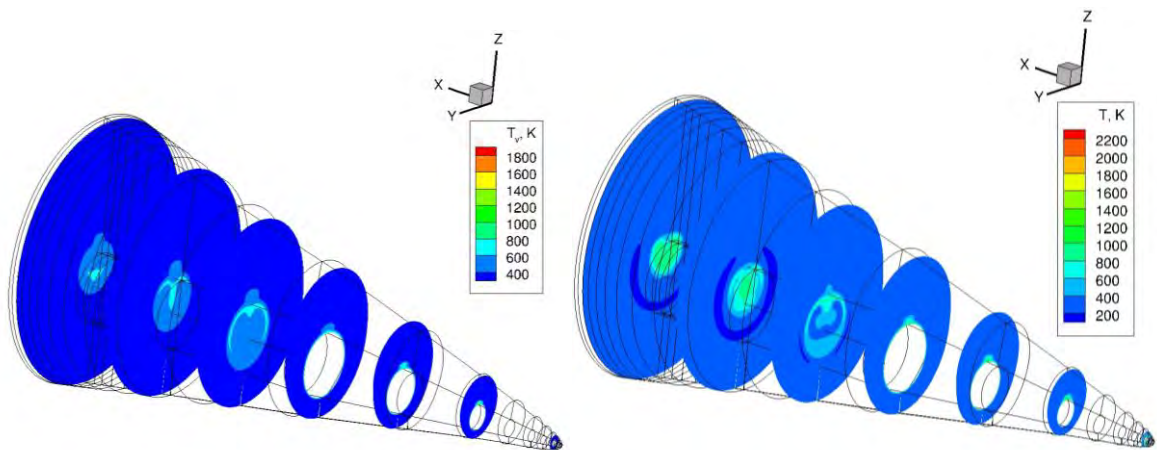
Figure 74. Vibrational Temperature Profile (left) Compared to Flowfield Temperature (right) in the Flowfield

After analyzing the thermodynamic properties, the results from chemical reactions in the flowfield needed to be analyzed. As mentioned earlier, Nitric Oxide, Carbon Dioxide and electron density will be of greatest interest to this study. All of the other chemical species are presented in Appendix B.

Nitric Oxide is the most common product of chemical reactions seen anywhere in the flowfield as depicted in Figure 75 though Figure 77. This high concentration is of particular interest to this research. Nitric Oxide was in its highest concentration at the nose which was expected since that was the location it was forming. The concentrations decreased as the flow moved down the body but the concentrations stayed significantly higher than the freestream. The concentration particularly in the wake core was roughly $2.5*10^{-5}$ while the freestream was $3.7*10^{-9}$. Nitric Oxide was in a higher concentration on the leeward side of the body. These high concentrations extended into the wake region and maintained that concentration until the flowfield stopped. Nitric Oxide is detectable in the viable light spectrum; however, the quantities of Nitric Oxide might not be large enough to enable detection.
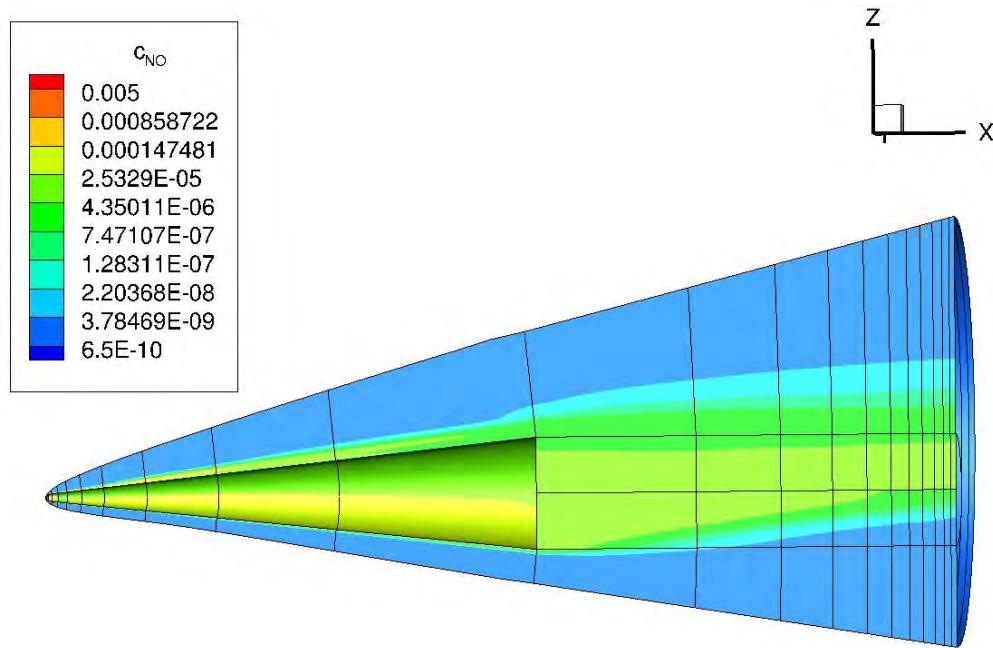

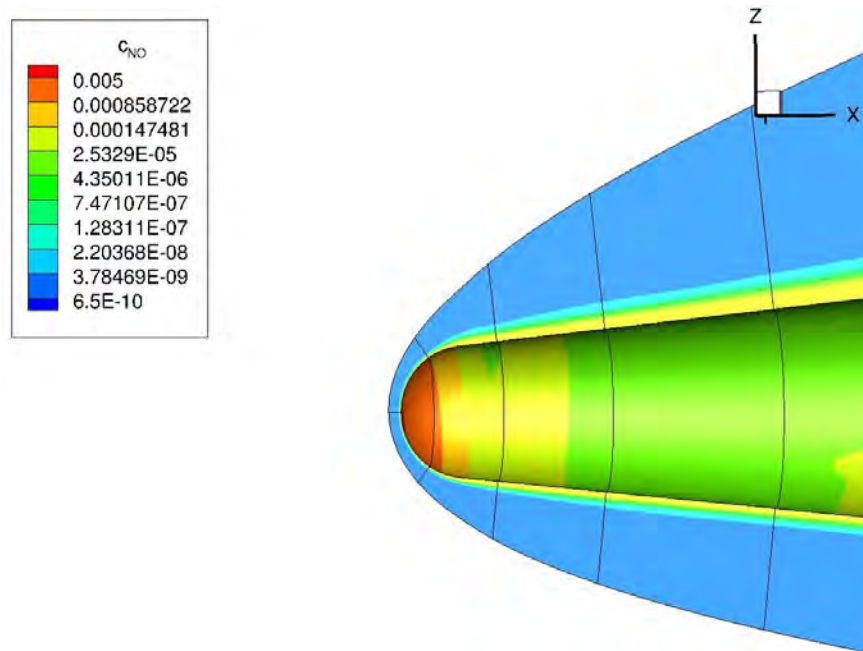Figure 75. Mass Fraction of Nitric Oxide throughout the Flowfield

Figure 76. Mass Fraction of Nitric Oxide at the Nose
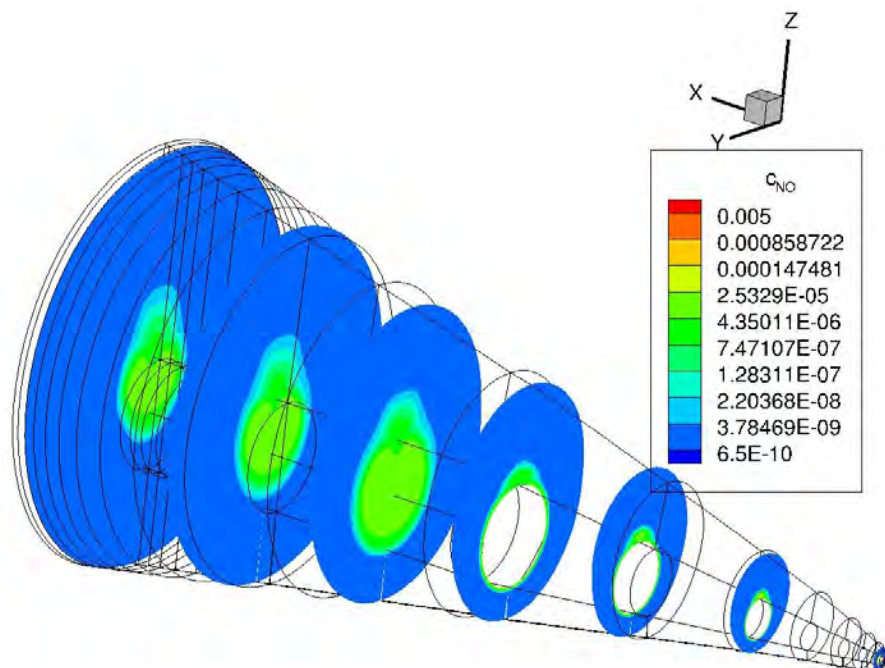
Figure 77. Mass Fraction of Nitric Oxide in the Flowfield

While examining Nitric Oxide there were two other phenomena noticed that hold true for all of the flowfield results. The first is a small inconsistency on the top of the flowfield near the wake region which caused a small jump in all of the contours and can be seen on the boundary of the flowfield. This inconsistency was caused by the LAURA *movegrd* subroutine and was not noticed until post processing of the data. It is not believed that this inconsistency caused any significant impact on the results of this study and was therefore not corrected. The second phenomenon noticed was the concentration of the chemical species was higher on the top of the body than the bottom. This higher concentration can be accounted for by looking at the streamlines at the nose as depicted in Figure 78. Upon inspection it was seen that the velocity streamlines are wrapping around the body from the bottom to the top. This wrapping caused a higher concentration of all species to be present on the top of the body. Examples of this could be seen in every chemical species present in the simulation.
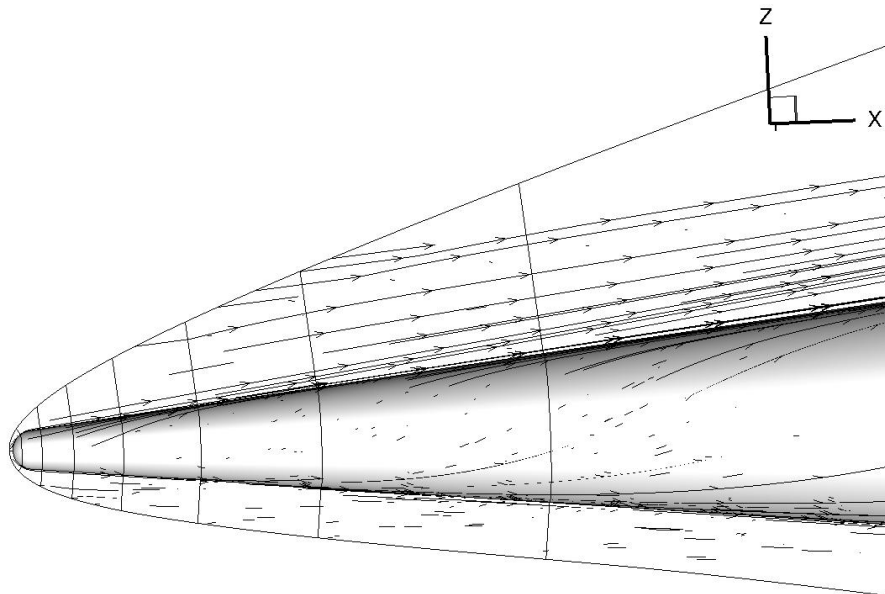
Figure 78. Velocity Streamlines at the Nose of the Body

Carbon Dioxide was the only other species in the wake that had any substantial quantity present, as depicted in Figure 79 though Figure 81. While the nose has significantly more Carbon Dioxide present than anywhere else in the flowfield, there is a considerable amount present in the wake when compared to the freestream, $3.4*10^{-9}$ and $5.4*10^{-24}$ respectively. The Carbon Dioxide that is present in the wake also extends in this relatively high concentration for several body diameters and looks to still be growing. This high concentration may also provide a trail from the body that could be detectable. Similarly to Nitric Oxide, Carbon Dioxide is detectable in the visible light spectrum so efforts would need to be focused there for an attempt at detection.

Figure 79. Mass Fraction of Carbon Dioxide throughout the Flowfield

Figure 80. Mass Fraction of Carbon Dioxide at the Nose

Figure 81. Mass Fraction of Carbon Dioxide in the Flowfield

The final species of interest is electron concentration. The election concentration is depicted in Figure 82 through Figure 84 and the number density is depicted in Figure 85 through Figure 87. High electron number density can be detected with the use of

microwave beams. While mass fraction present in the wake was not necessarily high, $2.2*10^{-22}$, due to the low mass of electrons, it was significantly higher than the freestream surrounding the wake 2.8*10-28. The electron number density in wake was significantly higher than the electron number density in freestream, $2.1*10^7$ and 12 respectively. This higher number density may lead to a possible source of detection in the microwave band but unfortunately is not in a high density compared to the total molecule density of 10^{24}. Keeping in line with Nitric Oxide and Carbon Dioxide the electrons were in greater number on the leeward side of the body and maintained that concentration into the wake region until the flow field stopped. Tracking electron concentrations in a flowfield with hot recirculating flow in the base region, as well as a neck recompression shock, is of particular interest. Both of these areas could produce temperatures that are hot enough to ionize molecules producing more electrons and increasing the signature in the microwave band.
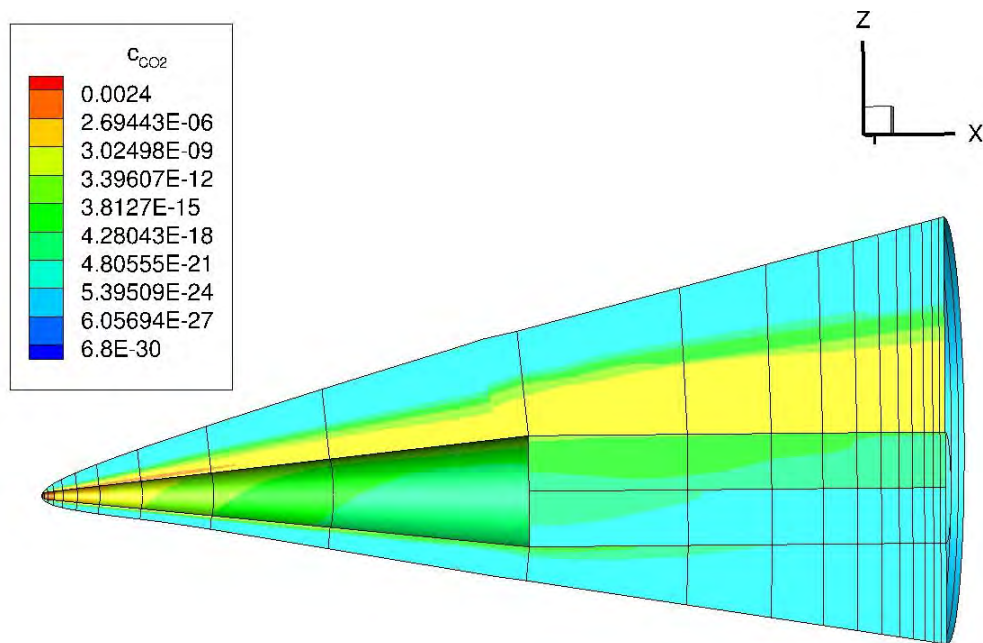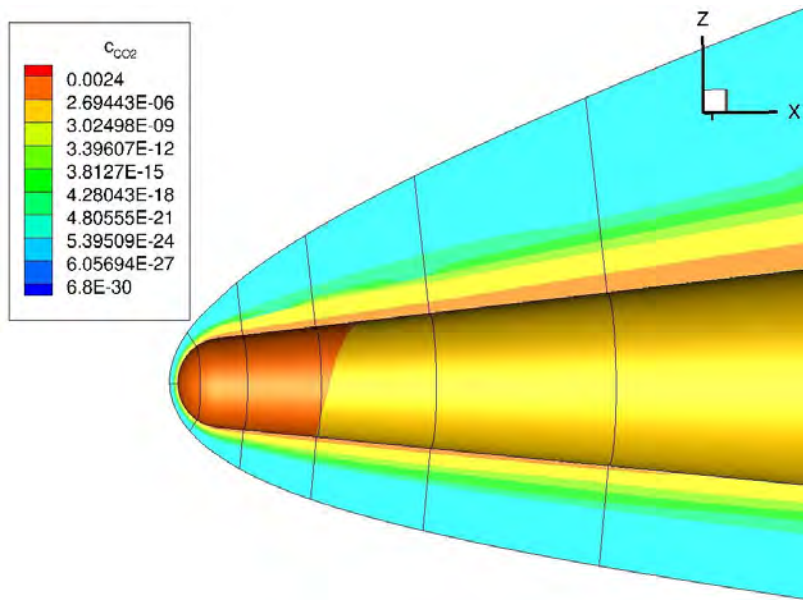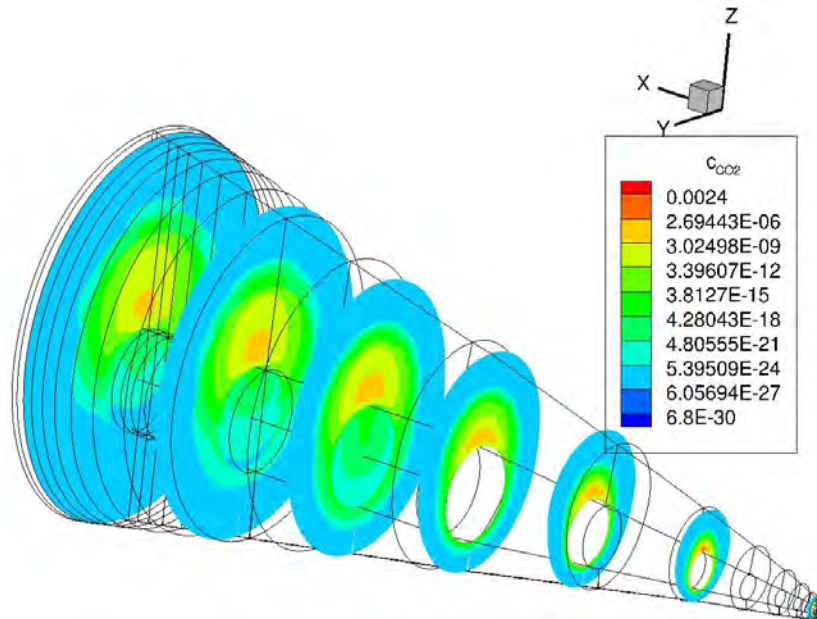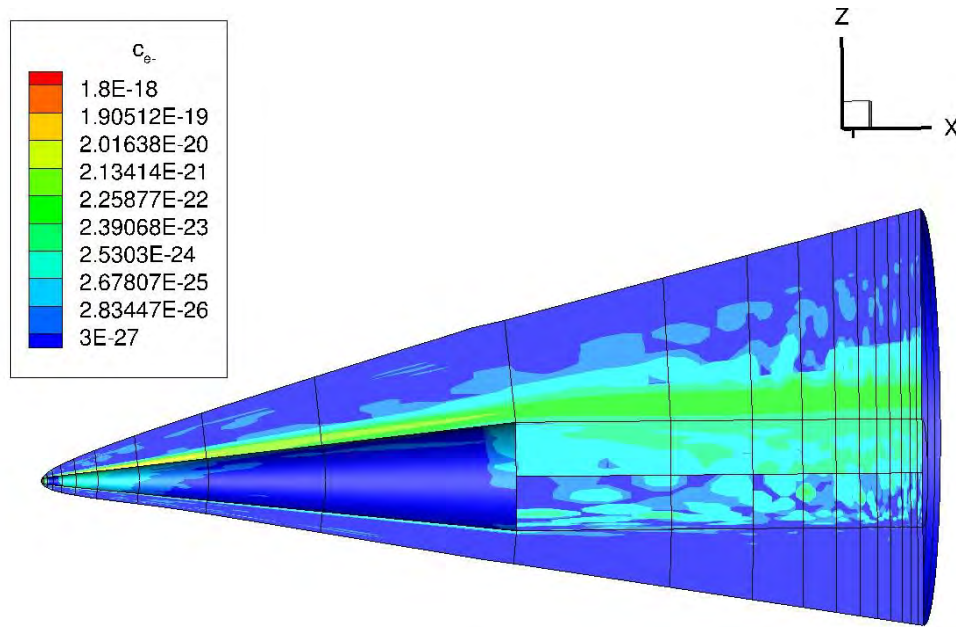

Figure 82. Mass Fraction of Electrons throughout the Flowfield
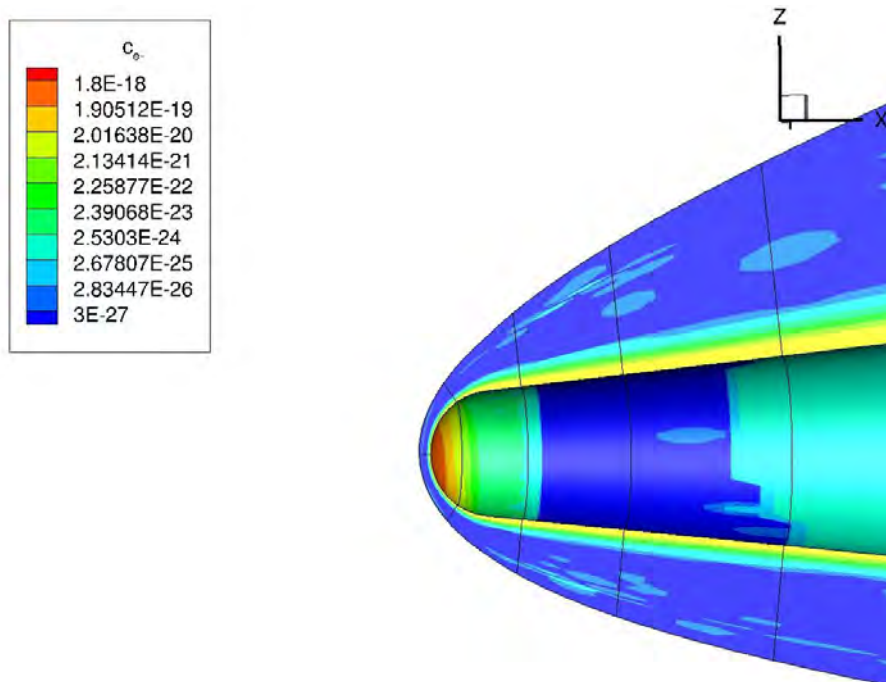
Figure 83. Mass Fraction of Electrons at the Nose
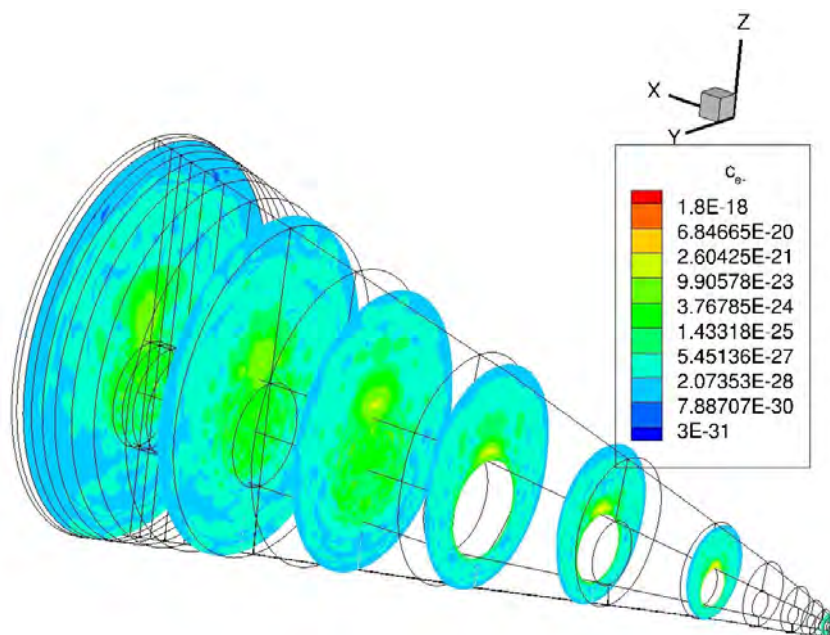
Figure 84. Mass Fraction of Electrons in the Flowfield
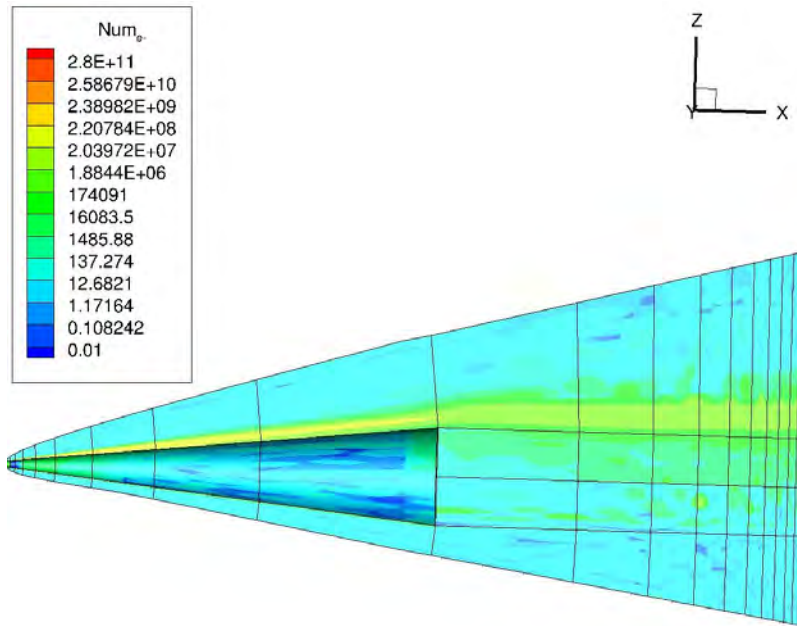
Figure 85. Number Density of Electrons throughout the Flowfield
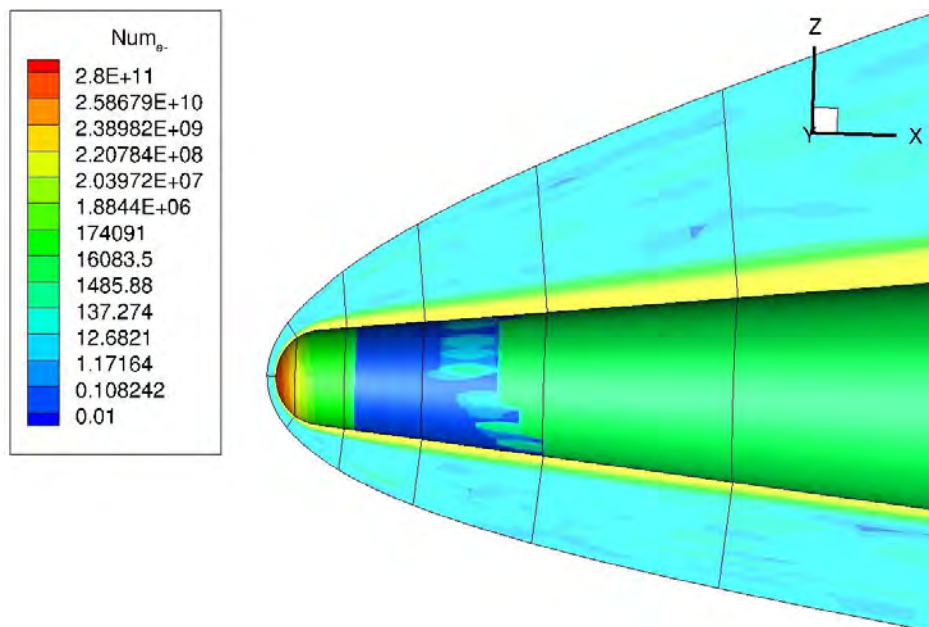
Figure 86. Number Density of Electrons at the Nose
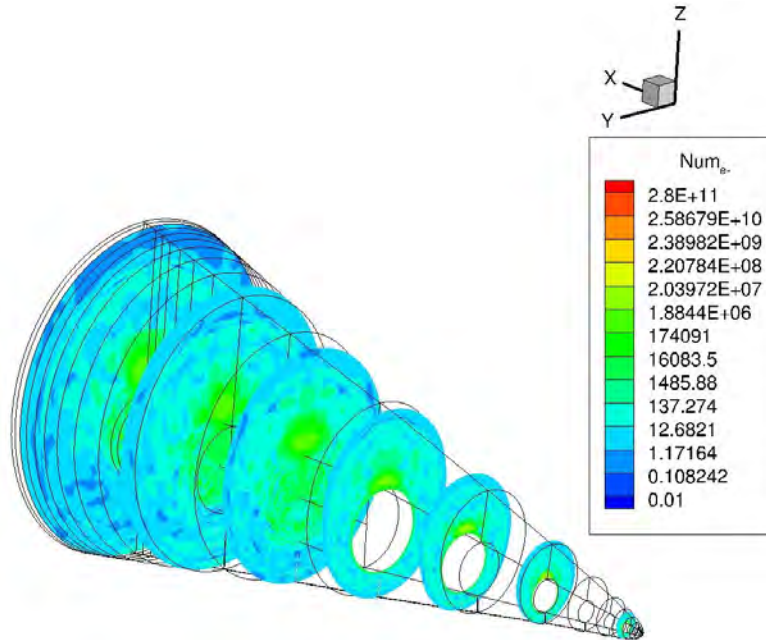
Figure 87. Number Density of Electrons in the Flowfield

As seen in the previous section there were several possible sources of detection in the wake that were discovered. The first source of detection would be the neck region of the wake where the temperatures were approaching the body stagnation point temperature. These high temperatures would be giving the gases in this area a massive amount of energy that may produce detectable radiation. Detection efforts in this area should be focused in the viable light spectrum. Both Nitric Oxide and Carbon Dioxide, the two most common species present, are both detectable in the visible light spectrum. Lastly, electrons are in a high number density in the wake region which may increase the radar cross section of the body. However, all of these possible sources of detection will be dependent on the technology level of the equipment being used.

V.   Discussion

5.1. Chapter Overview

The following chapter will summarize all results and draw any conclusions that were realized during the course of this research. Additionally, during this research there were several recommendations that were discovered and will be presented here.

5.2. Conclusion

The research presented in this paper was a study of the wake region of a hypersonic conic body. As mentioned earlier, previous studies conducted by NASA terminated in the 1960's. Therefore, this study was one of the first efforts in this area with a high fidelity simulation. The goal of this research was to characterize the wake by the aerothermal phenomena and the chemical species present while looking for possible sources of detection.

A converged solution was obtained for a simulation running with turbulence and ablation. Pointwise® and LAURA were used for grid creation and running the simulation, respectively. The simulation was setup to mimic real world conditions as closely as possible to ensure the accuracy of the results. Since wake region studies are just recently becoming an area of renewed interest in the aerodynamic community, there is no published data to compare these results to for accuracy. A grid independence study would verify the accuracy of the results or if the results obtained were solely dependent upon the grid that was used. However, a grid independence study was not performed for three reasons. The first reason was that the results obtained were in agreement with aerodynamic theory. The second reason was there have been published results, on similar bodies, that also used 64 cells in the body normal direction and achieved accurate

solutions. Lastly, a grid independence study was not performed due to time constraints. A grid independence study with LAURA is normally done using the *coarsen* function to coarsen the grid in the body normal direction. This new grid is then run until convergence and the results are compared. Unfortunately, due to the wake region, the *coarsen* function could not be used which meant that if a grid independence study were to be attempted it would have to be started from scratch and time did not allow for that process. Additionally, only one set of flight conditions was studied which meant that there was no data to compare the results to. The flight conditions that were picked were a typical glide during a boost-glide profile. By the time a converged solution was obtained, there was not enough time to start a new simulation with different flight conditions from scratch.

At the selected flight conditions, the aerothermal phenomena occurring differed from previously published results. Even though there was an expansion over the shoulder of the body and recirculating flow in the base, the recirculating flow was much cooler than expected. This cooler flow meant that there was no heating of the base region of the body and therefore no optical radiation due to radiative heating would be present. Consequently, efforts would need to be focused on the nose if detection via optical radiation from the surface of the body is to be attempted at the given flight conditions. The other major differences noted in this study were the lack of a neck stagnation point and neck recompression shock. These shocks have been seen in other studies between two and three body diameters. The lack of presence of these two phenomena was due to a relatively low Mach number and high slenderness ratio of the body. The convergence of streamlines was present in the neck of the wake and there was a significant increase in temperature, only 11% lower than the stagnation point. Unfortunately, the flowfield was

not extended far enough to capture the neck stagnation point and neck recompression shock. Since this shock is forming further downstream in the wake, it is most likely not a strong shock and may not always be present.

Analyzing the chemical species present led to some interesting results. The first was that all chemical species were in a higher concentration on the leeward side of the body and wake. Higher temperatures would lead one to suspect that there was a higher concentration of the chemical species in these areas. However, when streamlines were plotted, they were clearly wrapping around the body from the windward to the leeward side. These streamlines carried higher concentrations of all chemical species to the leeward side of the body. Therefore, if detection is attempted via radiation from the chemical species present, there would be a better chance of success looking down on the body and wake as opposed to looking up.

If an attempt is made to track a conic body via the chemical species present at these flight conditions, efforts should be focused on Nitric Oxide, Carbon Dioxide, and electron number density. Nitric Oxide and Carbon Dioxide are visible by optical radiation and were in relatively high concentrations in the wake. Using microwave beams to detect higher electron number density may also be a method of detection. While electron concentrations in the wake were not high, they were higher than the surrounding freestream conditions. Additionally, the number density of electrons in the wake was significantly higher than the freestream which may lead to a large radar cross section signature in the wake. Detecting a hypersonic body at these flight conditions will be dependent on the technology level of the equipment being used. As the equipment

becomes more sophisticated, it will be able to detect smaller and smaller sources of radiation and smaller concentrations of electrons.

This research lends itself to an immediate follow on project of modeling the radiation from the wake region. Ultimately, the radiation is what satellites are observing and is of significant importance to all tracking efforts. Using the data presented in the research, follow on research could be done on extracting a radiation signature from the wake and comparing that to the radiation from the body itself.

5.3. Recommendations

During the course of this research it was discovered that several improvements could be made to increase the accuracy of the results. The following section will cover what improvements could be used in follow on research including a radiation study, case selection, grid recommendations, and simulation recommendations.

The first recommendation for follow on efforts is research that focuses on line of sight radiation models. These models would determine the effects the wake region phenomena have in the different spectrums discussed. This research would be of the utmost importance since radiation is what is used in all tracking efforts.

Secondly, a hypersonic body that has been flight tested should be used for the simulation. A flight tested body would provide real world data that the results from the simulations would be compared to for accuracy. This comparison was not necessary for this research since the goal was to model the thermophysical phenomena that were occurring in the wake behind a hypersonic conic body.

Recommendations for grid improvements fall into five specific areas. The first grid improvement is to remove all of the pole boundaries. Due to the simplicity of the

body, a pole grid could be used. But using a pole grid on the body meant that a pole grid had to be used for the wake. While the pole grid of the body did not cause an issue since the stagnation point at the nose was not an area of interest for this research, it may have caused potential errors to be introduced into the wake region because information exchanges cannot occur across pole boundaries. A pole boundary running down the center of the wake may have caused errors to be present. The second grid improvement is to create a viscous spaced grid off the tail of the body and into the recirculation zone. Viscous spacing off the tail of the body was not incorporated due to time constraints. Increasing the number of cells in this area may cause the simulation to match Park's characterization of a hot recirculating zone directly behind the body. The third improvement to the grid is in the wake region, in the area of the shock. Once the location of the shock is determined, the grid spacing in that area should match that of the shock forward of the body. Decreasing the grid spacing in the region of the shock would allow LAURA to increase the fidelity and accuracy of the shock phenomena and the shocks effects on the flow. The fourth improvement, also in the wake region, is to extend the wake region to a minimum of ten body diameters. Extending the flowfield to ten body diameters should be enough to capture all phenomena in the wake, particularly the neck stagnation point and the recompression shock. The final improvement to the grid is to increase the cells in the body normal direction to 128. While this increase in the number of grid cells would cause a significant increase in the computation run time, it could possibly increase the accuracy of the result, especially when running the simulation with ablation. The only way to know for sure would be to conduct a grid independence study with a converged solution with 128 cells in the body normal direction.

106

Recommendations for improving simulations fall into five distinct areas. The first improvement is changing the sweep direction in LAURA. Breaking the grid up into 32 blocks was a temporary solution for when the change in the sweep direction failed. However, this is not the way LAURA is designed to be used. The second improvement for the simulation is with the transition to turbulent flow being assigned to the nose of the body. While this is most likely a fair assumption due to the loss of ablated material at the nose that would cause turbulent flow immediately, it is only an assumption and may not be an accurate model of the actual conditions. The third recommendation is to utilize the *shape_change* flag. This flag uses a geometry shape change algorithm due to ablation. This shape change would provide a more accurate body simulation due to of material lost from ablation. The fourth recommendation is to include Nitrogen Dioxide in the *tdata* file to facilitate the tracking of Nitrogen Dioxide in the solution. Nitrogen Dioxide has the possibility to be a large source of optical radiation and could be easily observed. After a Nitrogen Dioxide atom is formed and becomes excited, it returns to its ground state by emitting optical radiation. However, Nitrogen Dioxide's optical radiation is most likely not detectable until ten body diameters [16]. Since the flowfield did not extend that far in this study, Nitrogen Dioxide was not a tracked species. The final recommendation is to find a way to avoid restarting the simulation from scratch when the wake region is added. There are two possible methods to do this. The first of which is using the *assign_task* function of LAURA. If a full body and wake grid could be made before starting any simulations, *assign_task* could be used to deactivate the wake region while solving the flowfield around the body. The second method is to import the solution file from the body into the solution file for the body and the wake. Although no information could be

107

found about the second option in the current version of LAURA, it does exist in previous versions. Either of these methods not only decrease the amount of time needed, but would also increase the accuracy of the solution since the data for the flowfield over the body would not have to converge again after the wake region is added.

While these recommendations are not all encompassing, these are the major recommendations and changes that were discovered while performing this research. By using the recommendations that were discovered during the course of this research an even higher fidelity solution could be obtained; thus increasing this area of study even further.

Appendix A: LAURA Namelist for Simulations

The following figures are examples of the final LAURA Namelist files used for various simulations. These figures are for reference only and used to help show the methodology that was used throughout the simulations.

```
&laura_namelist
velocity_ref = 2115. ! reference velocity, m/s
density_ref  = 1.841e-2 ! reference density, kg/m^3
tref         = 226.5 ! reference temperature, K
alpha        = 5.0   ! pitch angle, degrees
yaw          = 0.    ! yaw angle, degree
twall_bc     = 500.  ! wall temperature, K
chem_flag  = 1 ! 0 chemically frozen, 1 chemical source on
therm_flag = 1 ! 0 thermally frozen,  1 thermal source on
turb_model_type = 0 ! 0 laminar, see turb_gen_module options
turb_int_inf     = 0.001 ! farfield turbulent intensity
turb_vis_ratio_inf = 0.01 ! farfield ratio turb to lam visc
prandtl_turb = 0.9 ! turbulent prandtl number
schmidt_turb = 0.9 ! turbulent schmidt number
xtr = 0. ! transition location for algebraic model along x
ivisc = 2  ! 2 if viscous, 0 if inviscid
irest  = 1 ! 0 for fresh start, 1 for restart
ncyc  = 10000 ! global steps
jupdate = 20 ! steps between update of jacobian
ntran  = 20 ! steps between update of transport properties
nitfo =  0 ! number of 1st-order relaxation steps
cfl1  = 5.e+00 ! initial value of cfl number
cfl2  = 5.e+00 ! value of cfl after iramp steps
iramp = 200 ! number of steps to ramp from cfl1 to cfl2
iterwrt = 200 ! steps between saves of intermediate solution
rmstol  = 1.e-10 ! tolerance on residual for stopping
itime  = 0 ! 0 for local time stepping, 1 for time accurate
dt      = 0.1 ! dimensionless time step
subiters = 1 ! subiterations for temporal accuracy
rf_inv = 3.0 ! inviscid relaxation parameter
rf_vis = 1.0 ! viscous relaxation parameter
epsa   = .25 ! eigenvalue limiter, rhs
hrs  = 10000.0 ! maximum wall time hours to run simulation
movegrd = 10000 ! number of steps between calls to align_shock
maxmoves =  0 ! maximum number of calls to align_shock
ep0_grd = 5.
kmax_error = 0.50 ! error norm for doubling grid in k-dir.
kmax_final = 64    ! max number cells in k dir after all doubling
nexch     = 1 ! steps between exchange of info in mpi
navier_stokes = .true.
nordbc = 1 ! boundary condition order
frac_line_implicit = 0.7 ! fraction of line by block tri-dia
surface_temperature_type_0 = 'radiative equilibrium'
catalysis_model_0 = 'equilibrium-catalytic'
emiss_a_0 = 0.90
ept = 0.001 ! relaxation factor on read eq wall bc
fsh = 0.8
dimensionality = '3D'
xmc =   2.3333
ymc = 0.
zmc =  0.0000
grid_conversion_factor =      1.0
sref =   0.47876
cref =     3.50000
/
```

Figure 88. Final LAURA Namelist File for Body

110

```
&laura_namelist
velocity_ref = 2115. ! reference velocity, m/s
density_ref  = 1.841e-2 ! reference density, kg/m^3
tref         = 226.5 ! reference temperature, K
alpha        = 5.0   ! pitch angle, degrees
yaw          = 0.    ! yaw angle, degree
twall_bc     = 500.  ! wall temperature, K
chem_flag  = 1 ! 0 chemically frozen, 1 chemical source on
therm_flag = 1 ! 0 thermally frozen,  1 thermal source on
turb_model_type = -1 ! 0 laminar, see turb_gen_module options
turb_int_inf     = 0.001 ! farfield turbulent intensity
turb_vis_ratio_inf = 0.01 ! farfield ratio turb to lam visc
prandtl_turb = 0.9 ! turbulent prandtl number
schmidt_turb = 0.9 ! turbulent schmidt number
xtr = 0. ! transition location for algebraic model along x
ivisc = 2  ! 2 if viscous, 0 if inviscid
irest  = 1 ! 0 for fresh start, 1 for restart
ncyc  = 10000 ! global steps
jupdate = 20 ! steps between update of jacobian
ntran   = 20 ! steps between update of transport properties
nitfo =  0 ! number of 1st-order relaxation steps
cfl1  = 5.e+00 ! initial value of cfl number
cfl2  = 5.e+00 ! value of cfl after iramp steps
iramp = 200 ! number of steps to ramp from cfl1 to cfl2
iterwrt = 200 ! steps between saves of intermediate solution
rmstol  = 1.e-10 ! tolerance on residual for stopping
itime  = 0 ! 0 for local time stepping, 1 for time accurate
dt     = 0.1 ! dimensionless time step
subiters = 1 ! subiterations for temporal accuracy
rf_inv = 3.0 ! inviscid relaxation parameter
rf_vis = 1.0 ! viscous relaxation parameter
epsa   = .25 ! eigenvalue limiter, rhs
hrs  = 10000.0 ! maximum wall time hours to run simulation
movegrd = 10000 ! number of steps between calls to align_shock
maxmoves =  0 ! maximum number of calls to align_shock
ep0_grd = 5.
kmax_error = 0.50 ! error norm for doubling grid in k-dir.
kmax_final = 64    ! max number cells in k dir after all doubling
nexch    = 1 ! steps between exchange of info in mpi
navier_stokes = .true.
nordbc = 1 ! boundary condition order
frac_line_implicit = 0.7 ! fraction of line by block tri-dia
surface_temperature_type_0 = 'radiative equilibrium'
catalysis_model_0 = 'equilibrium-catalytic'
emiss_a_0 = 0.90
ept = 0.001 ! relaxation factor on read eq wall bc
fsh = 0.8
dimensionality = '3D'
xmc =   2.3333
ymc = 0.
zmc =  0.0000
grid_conversion_factor =      1.0
sref =    0.47876
cref =     3.50000
/
```

Figure 89. Final LAURA Namelist File for Body with Turbulence

```
&laura_namelist
velocity_ref = 2115. ! reference velocity, m/s
density_ref  = 1.841e-2 ! reference density, kg/m^3
tref         = 226.5 ! reference temperature, K
alpha        = 5.0   ! pitch angle, degrees
yaw          = 0.    ! yaw angle, degree
twall_bc     = 500.  ! wall temperature, K
chem_flag  = 1 ! 0 chemically frozen, 1 chemical source on
therm_flag = 1 ! 0 thermally frozen,  1 thermal source on
turb_model_type = 0 ! 0 laminar, see turb_gen_module options
turb_int_inf    = 0.001 ! farfield turbulent intensity
turb_vis_ratio_inf = 0.01 ! farfield ratio turb to lam visc
prandtl_turb = 0.9 ! turbulent prandtl number
schmidt_turb = 0.9 ! turbulent schmidt number
xtr = 0. ! transition location for algebraic model along x
ivisc = 2  ! 2 if viscous, 0 if inviscid
irest  = 0 ! 0 for fresh start, 1 for restart
ncyc  = 80000 ! global steps
jupdate = 20 ! steps between update of jacobian
ntran  = 20 ! steps between update of transport properties
nitfo =  500 ! number of 1st-order relaxation steps
cfl1  = 5.e+00 ! initial value of cfl number
cfl2  = 5.e+00 ! value of cfl after iramp steps
iramp = 200 ! number of steps to ramp from cfl1 to cfl2
iterwrt = 200 ! steps between saves of intermediate solution
rmstol  = 1.e-10 ! tolerance on residual for stopping
itime   = 0 ! 0 for local time stepping, 1 for time accurate
dt       = 0.1 ! dimensionless time step
subiters = 1 ! subiterations for temporal accuracy
rf_inv = 3.0 ! inviscid relaxation parameter
rf_vis = 1.0 ! viscous relaxation parameter
epsa    = .25 ! eigenvalue limiter, rhs
hrs  = 100000000.0 ! maximum wall time hours to run simulation
movegrd = 0 ! number of steps between calls to align_shock
maxmoves =  0 ! maximum number of calls to align_shock
ep0_grd = 5.
kmax_error = 0.50 ! error norm for doubling grid in k-dir.
kmax_final = 0    ! max number cells in k dir after all doubling
nexch    = 1 ! steps between exchange of info in mpi
navier_stokes = .true.
nordbc = 1 ! boundary condition order
frac_line_implicit = 0.7 ! fraction of line by block tri-dia
surface_temperature_type_0 = 'radiative equilibrium'
catalysis_model_0 = 'equilibrium-catalytic'
emiss_a_0 = 0.90
ept = 0.005 ! relaxation factor on read eq wall bc
fsh = 0.8
dimensionality = '3D'
xmc =    2.3333
ymc = 0.
zmc =  0.0000
grid_conversion_factor =      1.0
sref =    0.47876
cref =    3.50000
/
```

Figure 90. Final LAURA Namelist File for Body and Wake

112

```
&laura_namelist
velocity_ref = 2115. ! reference velocity, m/s
density_ref  = 1.841e-2 ! reference density, kg/m^3
tref         = 226.5 ! reference temperature, K
alpha        = 5.0   ! pitch angle, degrees
yaw          = 0.    ! yaw angle, degree
twall_bc     = 500.  ! wall temperature, K
chem_flag  = 1 ! 0 chemically frozen, 1 chemical source on
therm_flag = 1 ! 0 thermally frozen,  1 thermal source on
turb_model_type = 6 ! 0 laminar, see turb_gen_module options
turb_int_inf    = 0.001 ! farfield turbulent intensity
turb_vis_ratio_inf = 0.01 ! farfield ratio turb to lam visc
prandtl_turb = 0.9 ! turbulent prandtl number
schmidt_turb = 0.9 ! turbulent schmidt number
xtr = 0. ! transition location for algebraic model along x
ivisc = 2  ! 2 if viscous, 0 if inviscid
irest  = 1 ! 0 for fresh start, 1 for restart
ncyc  = 200000 ! global steps
jupdate = 20 ! steps between update of jacobian
ntran   = 20 ! steps between update of transport properties
nitfo =  500 ! number of 1st-order relaxation steps
cfl1  = 5.e+00 ! initial value of cfl number
cfl2  = 5.e+00 ! value of cfl after iramp steps
iramp = 200 ! number of steps to ramp from cfl1 to cfl2
iterwrt = 200 ! steps between saves of intermediate solution
rmstol  = 1.e-10 ! tolerance on residual for stopping
itime   = 0 ! 0 for local time stepping, 1 for time accurate
dt      = 0.1 ! dimensionless time step
subiters = 1 ! subiterations for temporal accuracy
rf_inv = 3.0 ! inviscid relaxation parameter
rf_vis = 1.0 ! viscous relaxation parameter
epsa   = .25 ! eigenvalue limiter, rhs
hrs  = 100000000.0 ! maximum wall time hours to run simulation
movegrd = 0 ! number of steps between calls to align_shock
maxmoves =  0 ! maximum number of calls to align_shock
ep0_grd = 5.
kmax_error = 0.50 ! error norm for doubling grid in k-dir.
kmax_final = 0    ! max number cells in k dir after all doubling
nexch    = 1 ! steps between exchange of info in mpi
navier_stokes = .true.
nordbc = 1 ! boundary condition order
frac_line_implicit = 0.7 ! fraction of line by block tri-dia
surface_temperature_type_0 = 'radiative equilibrium'
catalysis_model_0 = 'equilibrium-catalytic'
emiss_a_0 = 0.90
ept = 0.001 ! relaxation factor on read eq wall bc
fsh = 0.8
dimensionality = '3D'
xmc =   2.3333
ymc = 0.
zmc =  0.0000
grid_conversion_factor =      1.0
sref =   0.47876
cref =     3.50000
/
```

Figure 91. Final LAURA Namelist File for Body and Wake with Turbulence

113

```
&laura_namelist
velocity_ref = 2115. ! reference velocity, m/s
density_ref  = 1.841e-2 ! reference density, kg/m^3
tref         = 226.5 ! reference temperature, K
alpha        = 5.0   ! pitch angle, degrees
yaw          = 0.    ! yaw angle, degree
twall_bc     = 500.  ! wall temperature, K
chem_flag  = 1 ! 0 chemically frozen, 1 chemical source on
therm_flag = 1 ! 0 thermally frozen,  1 thermal source on
turb_model_type = 6 ! 0 laminar, see turb_gen_module options
turb_int_inf    = 0.001 ! farfield turbulent intensity
turb_vis_ratio_inf = 0.01 ! farfield ratio turb to lam visc
prandtl_turb = 0.9 ! turbulent prandtl number
schmidt_turb = 0.9 ! turbulent schmidt number
xtr = 0. ! transition location for algebraic model along x
ivisc = 2  ! 2 if viscous, 0 if inviscid
irest   = 1 ! 0 for fresh start, 1 for restart
ncyc  = 200000 ! global steps
jupdate = 20 ! steps between update of jacobian
ntran   = 20 ! steps between update of transport properties
nitfo =  500 ! number of 1st-order relaxation steps
cfl1  = 5.e+00 ! initial value of cfl number
cfl2  = 5.e+00 ! value of cfl after iramp steps
iramp = 200 ! number of steps to ramp from cfl1 to cfl2
iterwrt = 200 ! steps between saves of intermediate solution
rmstol  = 1.e-10 ! tolerance on residual for stopping
itime   = 0 ! 0 for local time stepping, 1 for time accurate
subiters = 1 ! subiterations for temporal accuracy
rf_inv = 3.0 ! inviscid relaxation parameter
rf_vis = 1.0 ! viscous relaxation parameter
epsa   = .25 ! eigenvalue limiter, rhs
hrs  = 100000000.0 ! maximum wall time hours to run simulation
ep0_grd = 5.
kmax_error = 0.50 ! error norm for doubling grid in k-dir.
kmax_final = 0     ! max number cells in k dir after all doubling
nexch     = 1 ! steps between exchange of info in mpi
navier_stokes = .true.
nordbc = 1 ! boundary condition order
frac_line_implicit = 0.7 ! fraction of line by block tri-dia
catalysis_model_0 = 'equilibrium-catalytic'
emiss_a_0 = 0.90
ept = 0.001 ! relaxation factor on read eq wall bc
fsh = 0.8
dimensionality = '3D'
xmc =   2.3333
ymc = 0.
zmc =  0.0000
grid_conversion_factor =       1.0
sref =   0.47876
cref =    3.50000
surface_temperature_type_0 = 'surface energy balance'
blowing_model_0 = 'equil_char_quasi_steady'
freq_wall = 10000
bprime_flag = 1
compute_mdot_initial = 1
ablation_option = 0
/
```

Figure 92. Final LAURA Namelist File for Body and Wake with Turbulence and Ablation

Appendix B: Supplemental Results

The following is a presentation of all of the data that was obtained during the course of this research that was supplemental and was not required to be presented in the results of this research. The data is being included for the sake of completion.

Figure 93 and Figure 94 depict the concentration of Diatomic Oxygen on the surface. Diatomic Oxygen was close to freestream concentrations since it was only be dissociated at the nose.
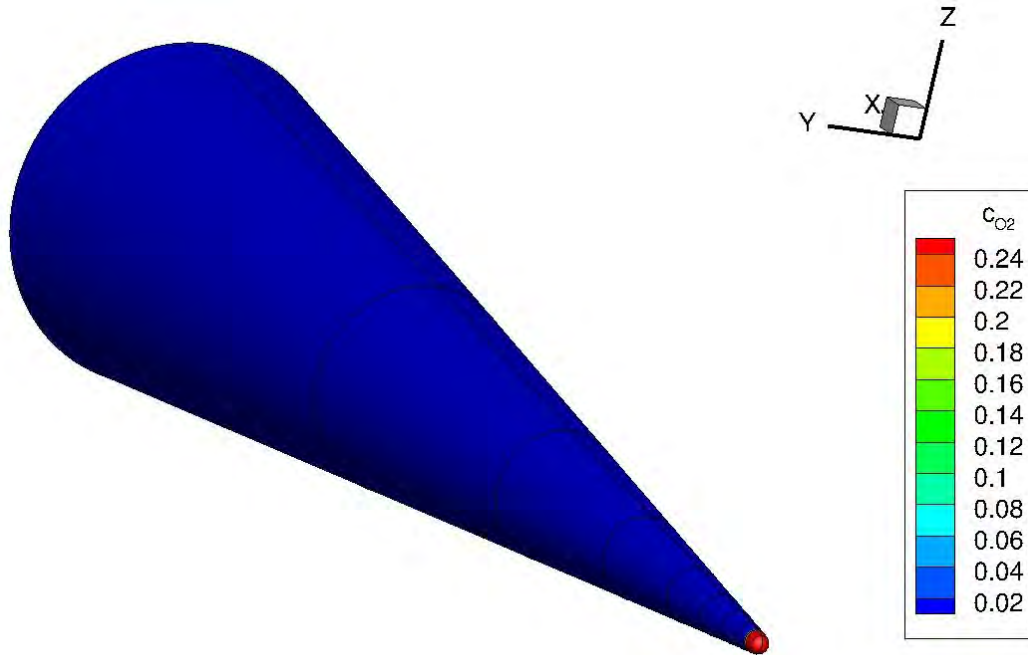

Figure 93. Mass Fraction of Diatomic Oxygen on the Surface of the Body
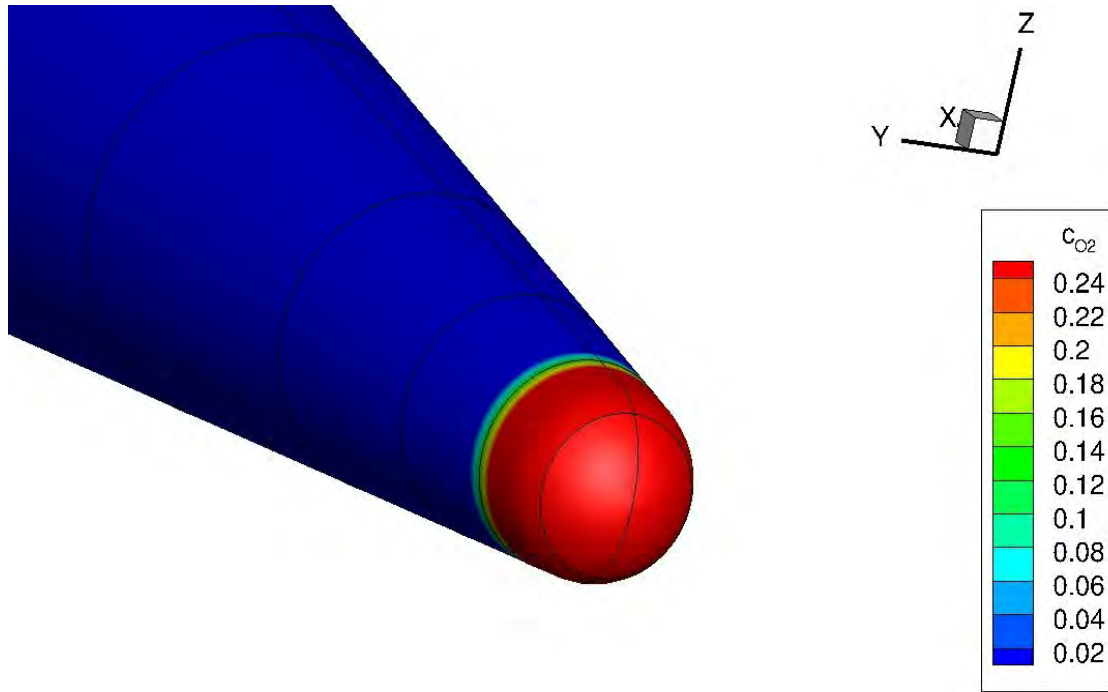
Figure 94. Mass Fraction of Diatomic Oxygen on the Nose of the Body

Figure 95 and Figure 96 depict the concentration of Monatomic Oxygen on the surface. Monatomic Oxygen formed at the nose where temperatures where hot enough to cause dissociation.
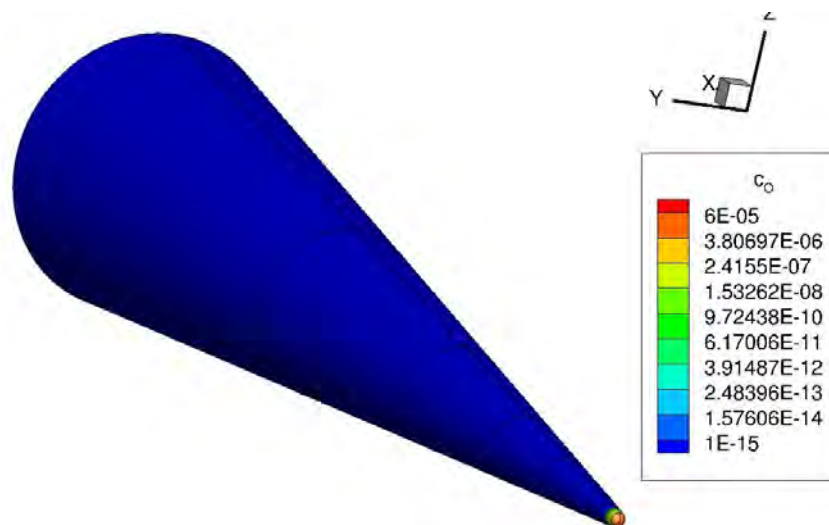
Figure 95. Mass Fraction of Monatomic Oxygen on the Surface of the Body
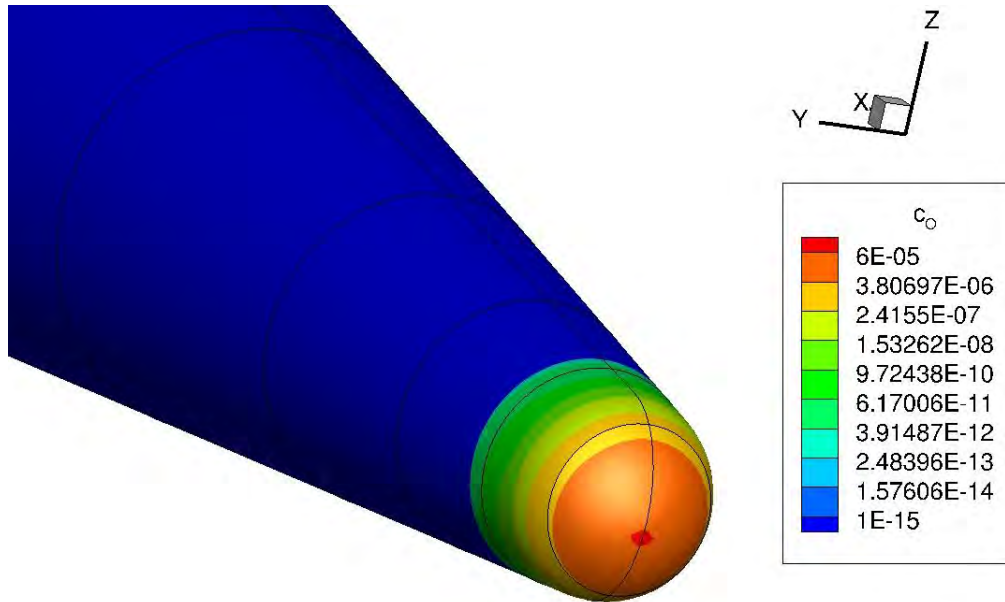
Figure 96. Mass Fraction of Monatomic Oxygen on the Nose of the Body

Figure 97 and Figure 98 depict the concentration of electrons on the surface. Free electrons were only present due to the formation of Nitrosonium.
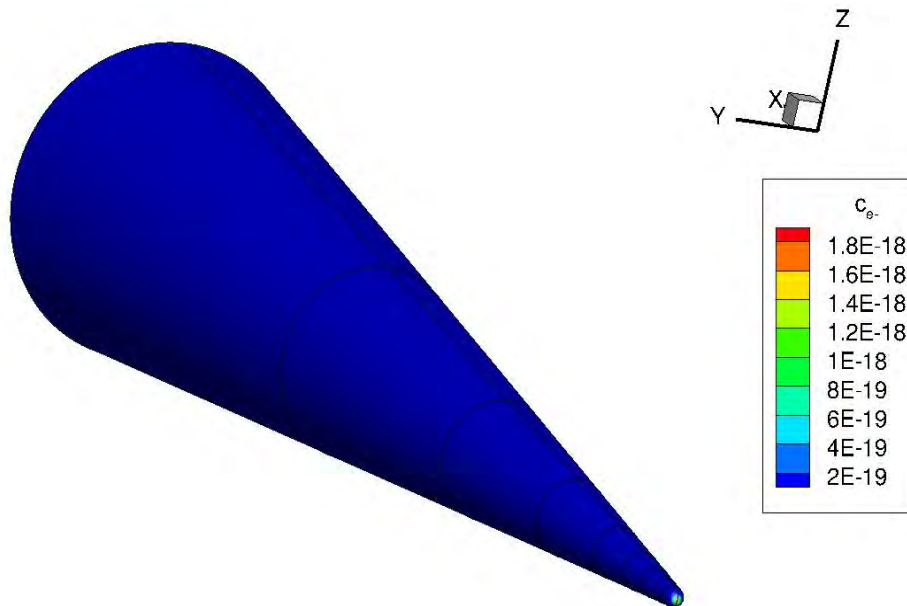
Figure 97. Mass Fraction of Electrons on the Surface of the Body
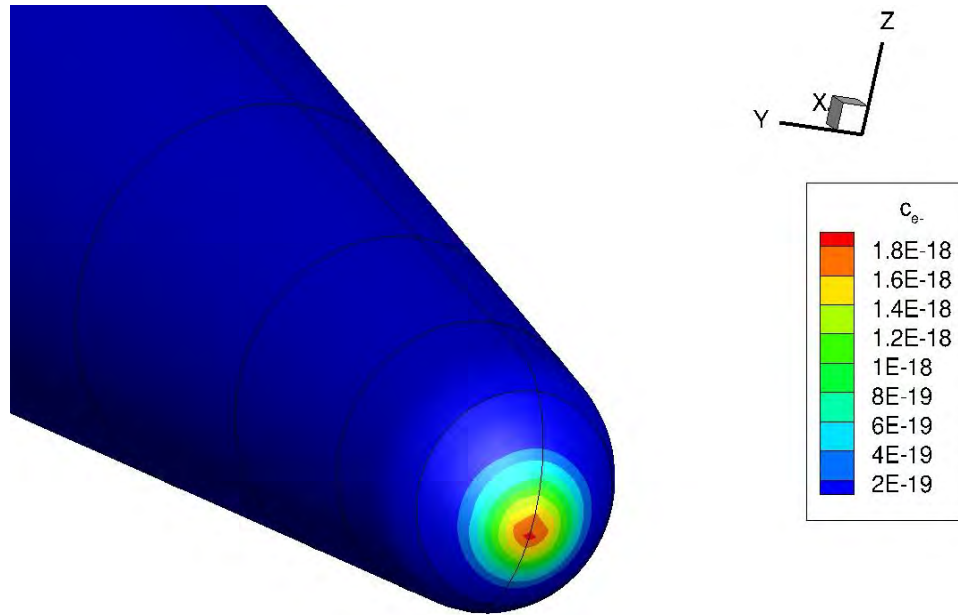
Figure 98. Mass Fraction of Electrons on the Nose of the Body

Figure 99 through Figure 102 depicts the concentration of Monatomic Carbon and Diatomic Carbon on the surface. Pure carbon species were in very low concentrations due to the relatively low temperatures on the surface of the body.
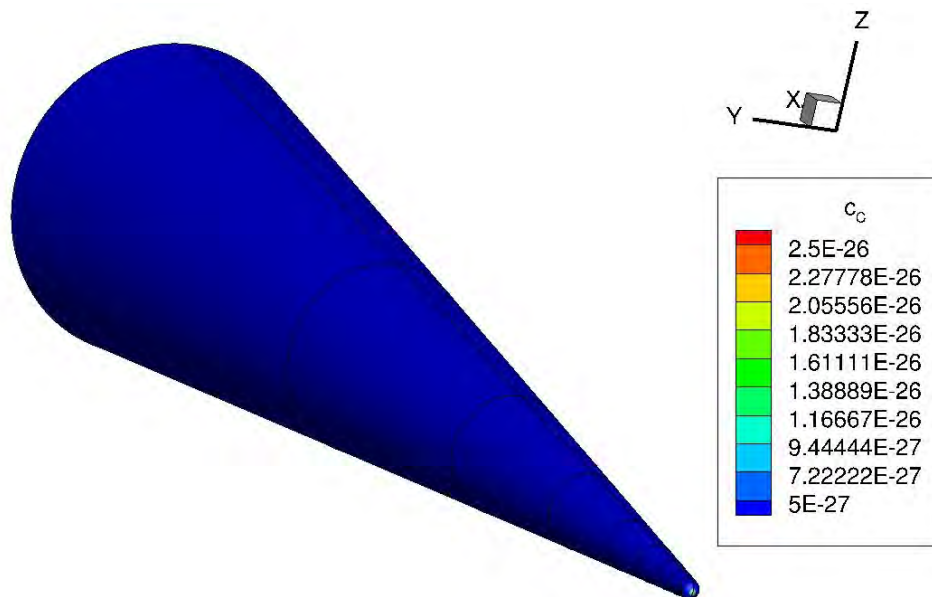
Figure 99. Mass Fraction of Carbon on the Surface
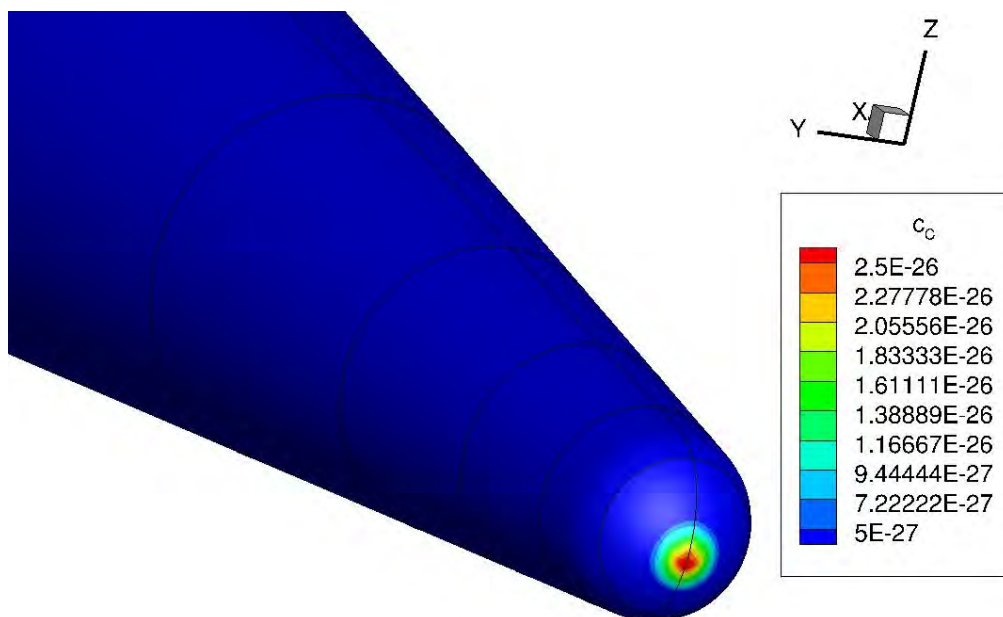
Figure 100. Mass Fraction of Carbon on the Nose of the Body
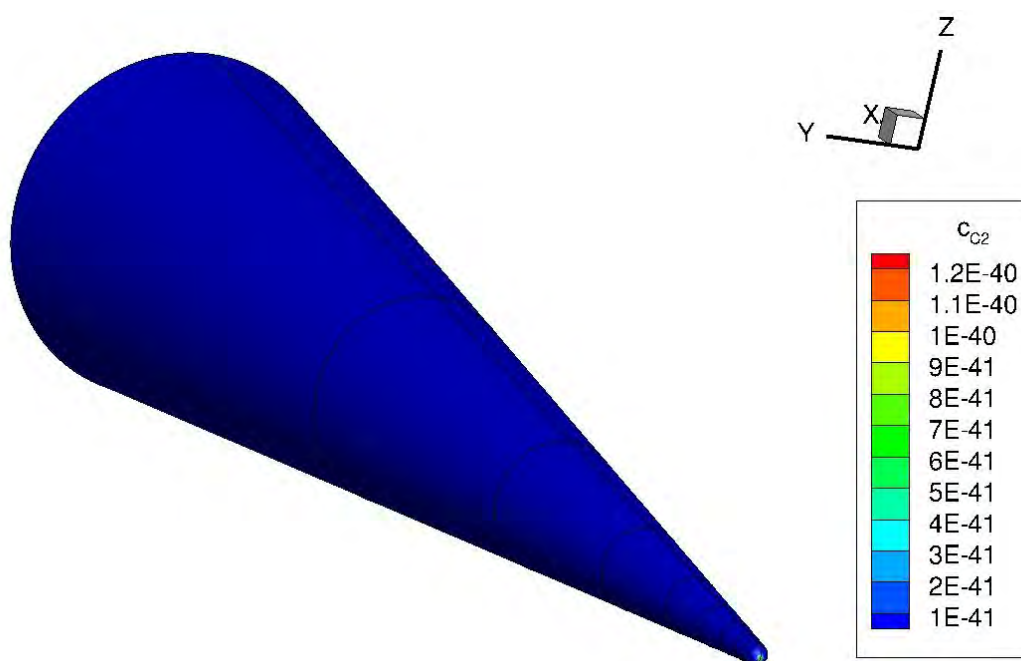
Figure 101. Mass Fraction of Diatomic Carbon on the Surface
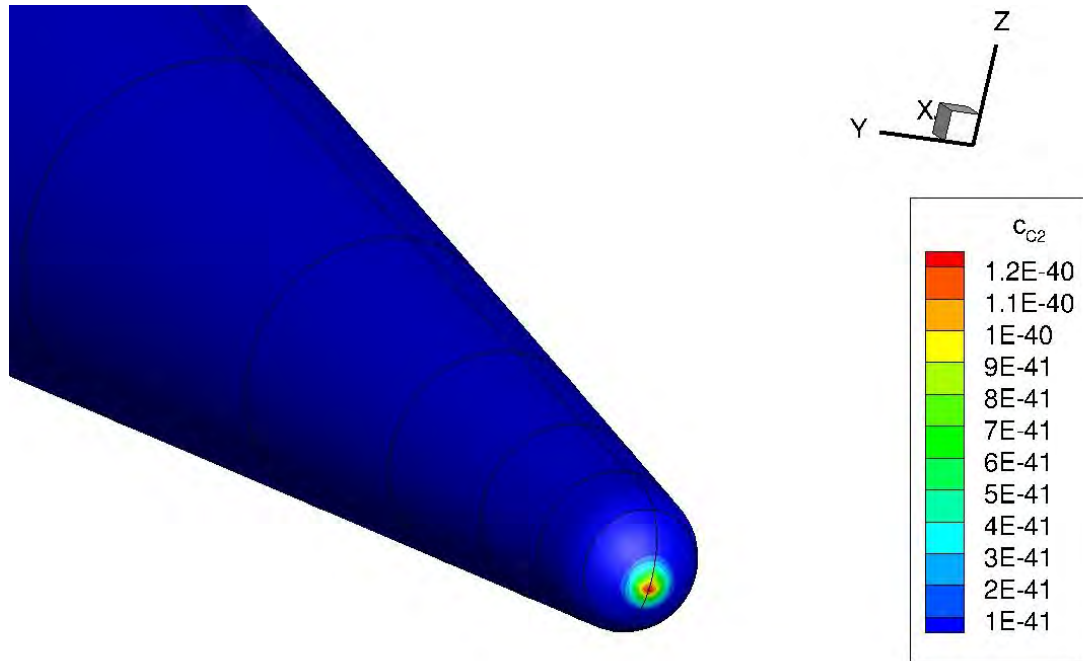
Figure 102. Mass Fraction of Diatomic Carbon on the Nose of the Body

Figure 103 through Figure 108 depicts the concentration of Diatomic Nitrogen, Diatomic Oxygen, Monatomic Nitrogen and Monatomic Oxygen throughout the flowfield. Diatomic Nitrogen and Oxygen were close to freestream concentrations since they were only dissociated at the nose. Consequently the highest concentration of Monatomic Nitrogen and Oxygen were in the highest concentration at the nose.
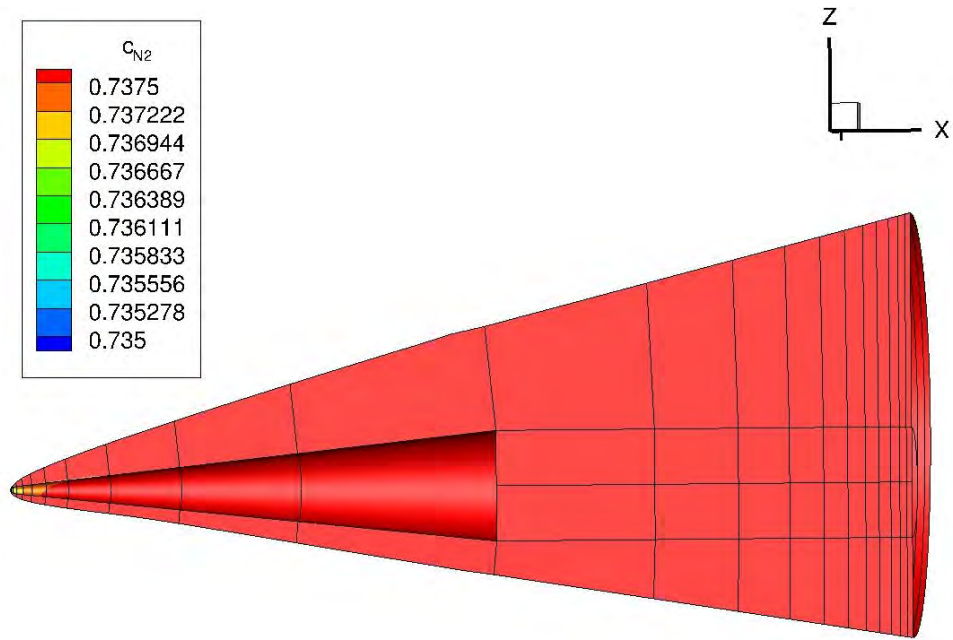
Figure 103. Mass Fraction of Diatomic Nitrogen throughout the Flowfield
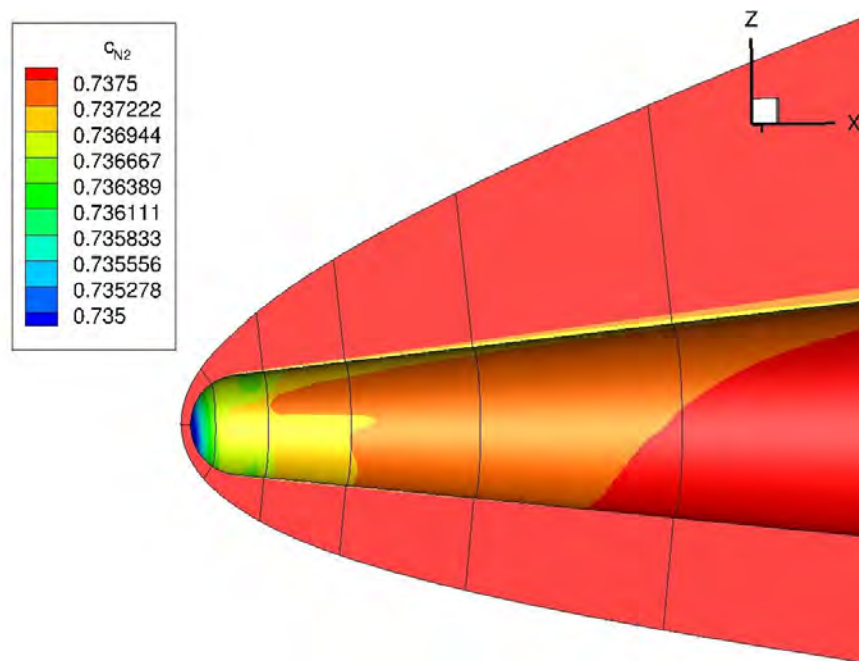
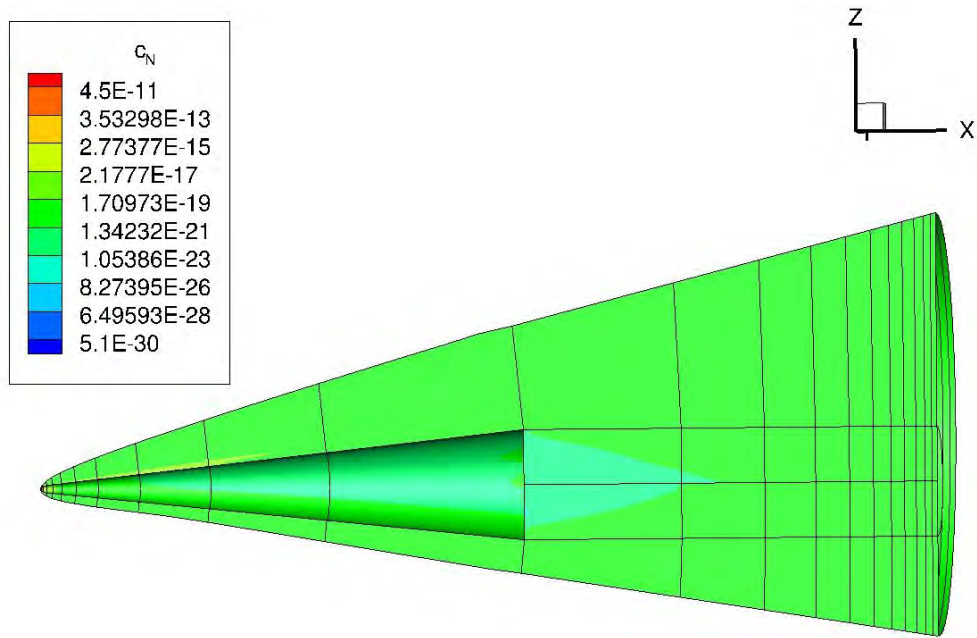Figure 104. Mass Fraction of Diatomic Nitrogen at the Nose

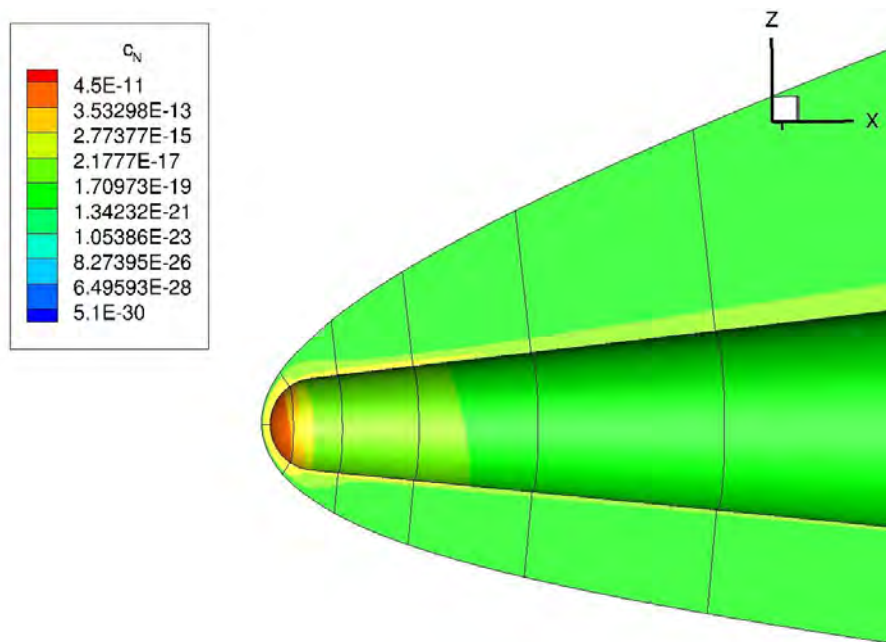Figure 105. Mass Fraction of Monatomic Nitrogen throughout the Flowfield

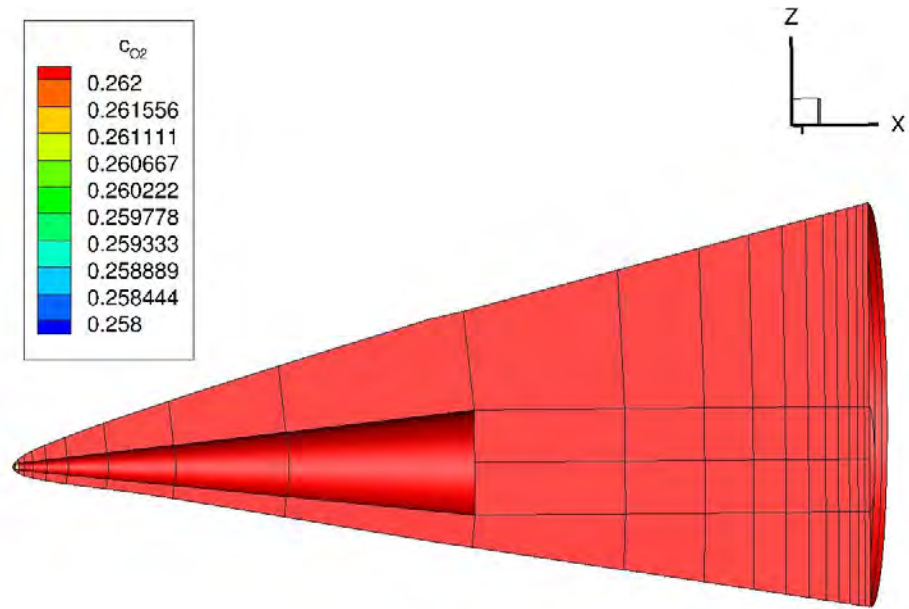Figure 106. Mass Fraction of Monatomic Nitrogen throughout the Flowfield

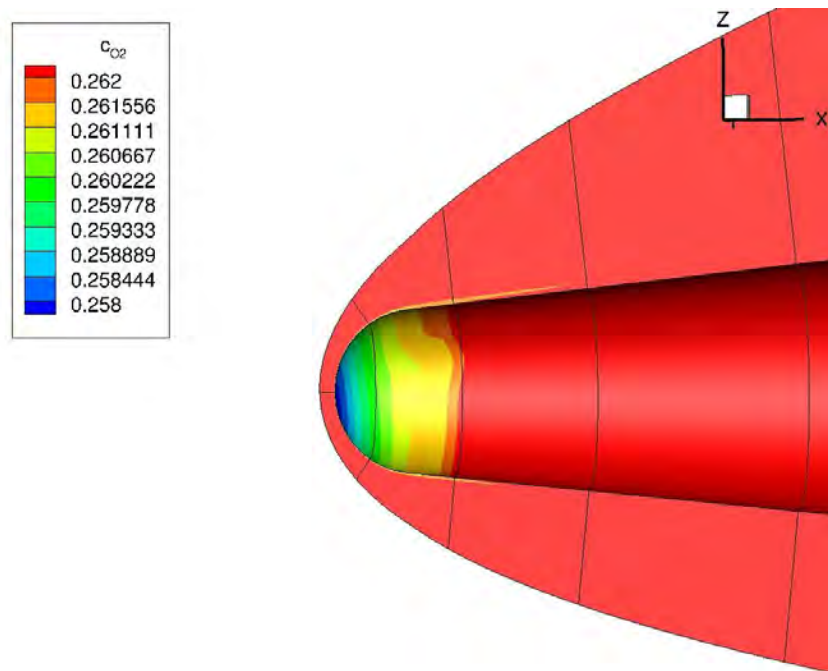Figure 107. Mass Fraction of Diatomic Oxygen throughout the Flowfield

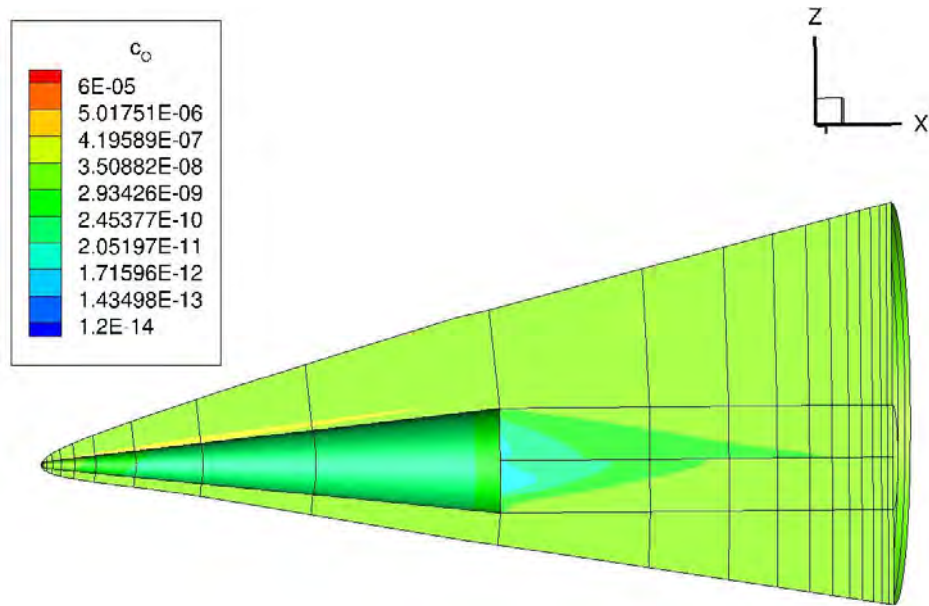Figure 108. Mass Fraction of Diatomic Oxygen at the Nose

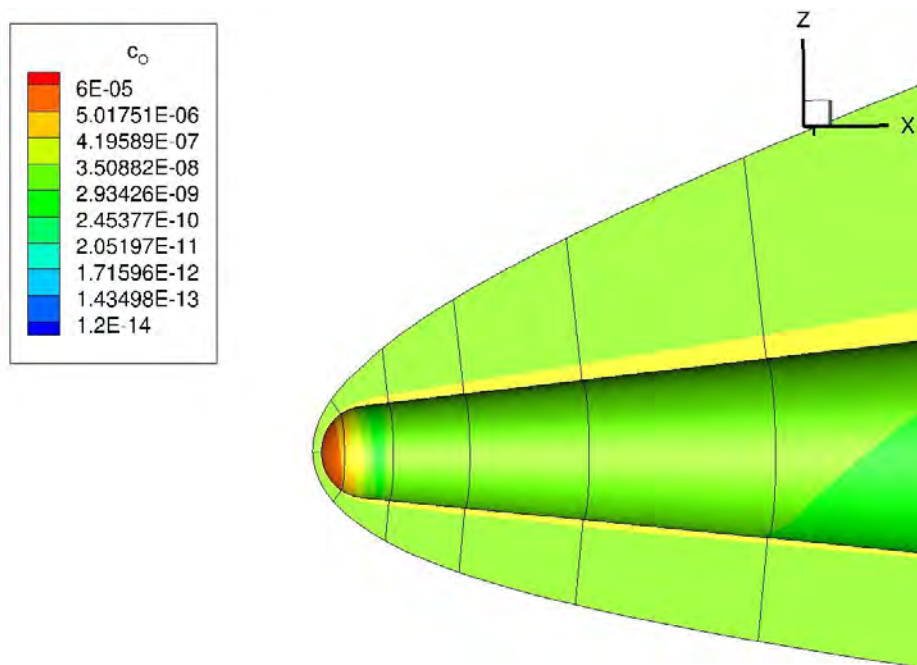Figure 109. Mass Fraction of Oxygen throughout the Flowfield

Figure 110. Mass Fraction of Oxygen at the Nose

124

Figure 111 and Figure 112 depict the concentration of Nitrosonium throughout the flowfield. Nitrosonium only formed at the nose where temperatures were hot enough to facilitate formation. While the wake concentration is higher than the flowfield concentration it was determined these concentrations were too low for detection.
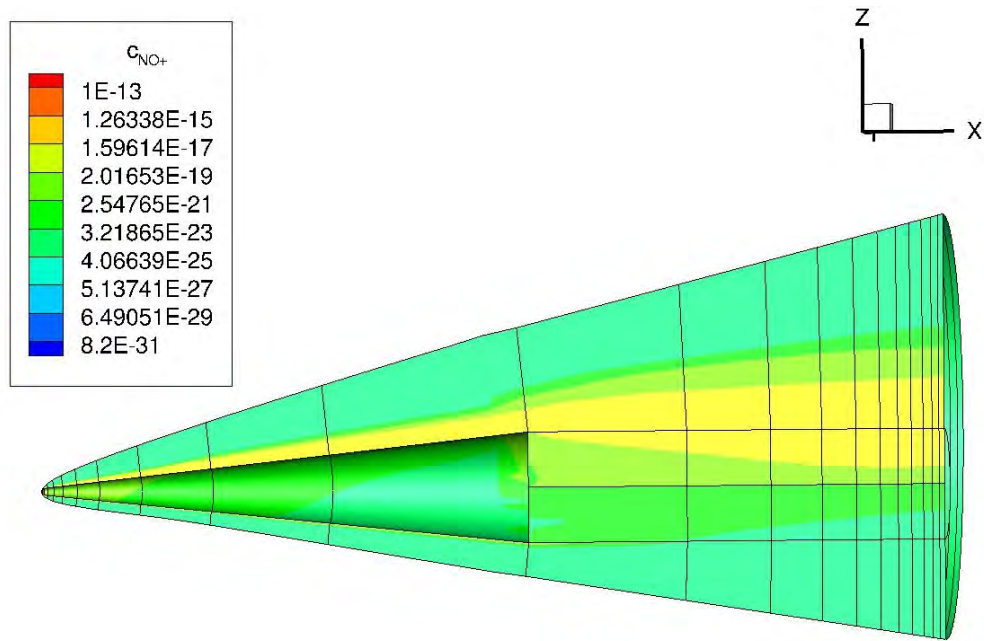

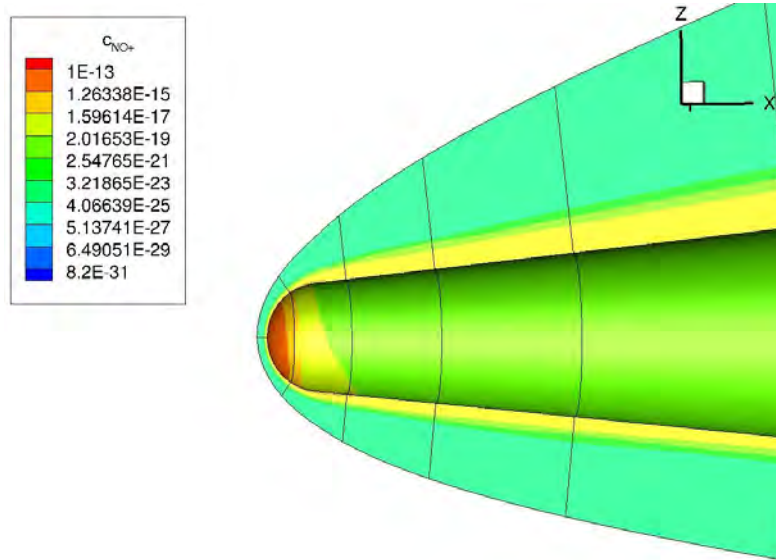Figure 111. Mass Fraction of Nitrosonium throughout the Flowfield

Figure 112. Mass Fraction of Nitrosonium at the Nose

Figure 113 and Figure 114 depict the concentration of Carbon Monoxide throughout the flowfield. Carbon Monoxide only formed when there was not enough Monatomic Oxygen to form Carbon Dioxide. While the wake concentration is higher than the flowfield concentration it was determined these concentrations were too low for detection.
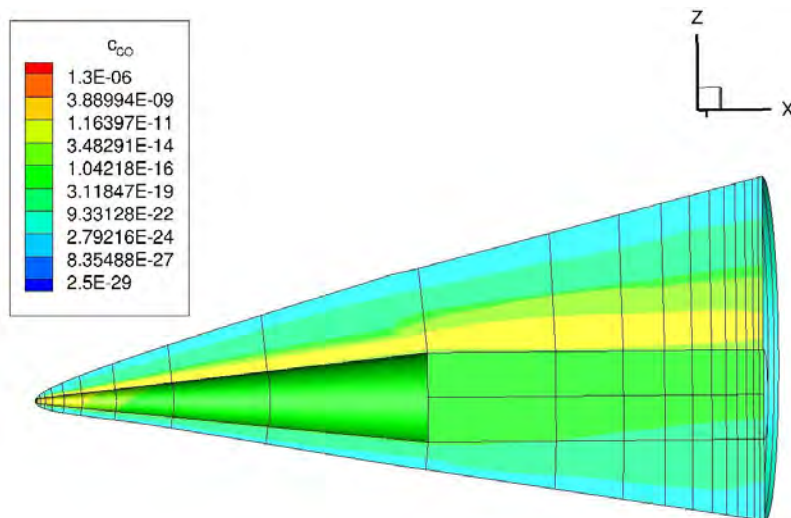

Figure 113. Mass Fraction of Carbon Monoxide throughout the Flowfield
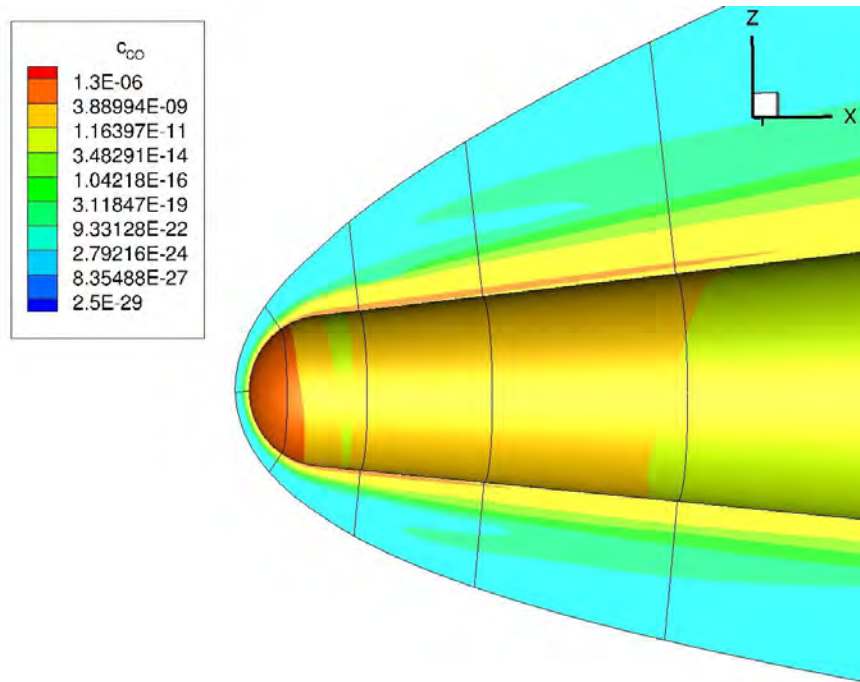
Figure 114. Mass Fraction of Carbon Monoxide at the Nose

Figure 115 through Figure 120 depicts the concentration of pure carbon species throughout the flowfield. Pure carbon species are formed when sublimation occurs at 3,000. Surface temperatures only reached 1,800 K therefore there was no sublimation that occurred resulting in no pure carbon species being present. Any Monatomic Carbon formed was used in the formation of other molecules.

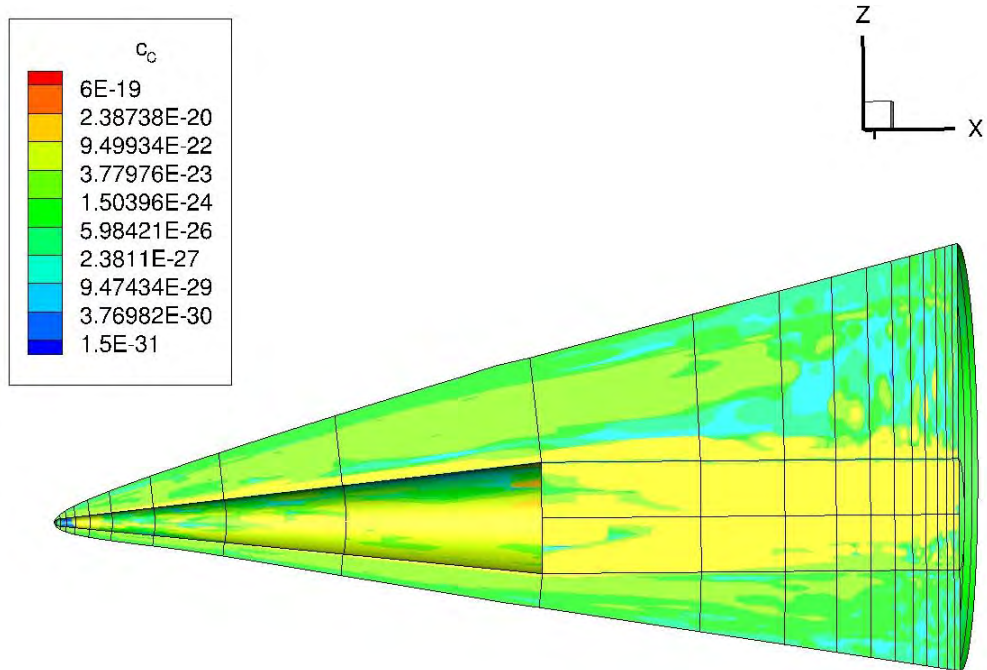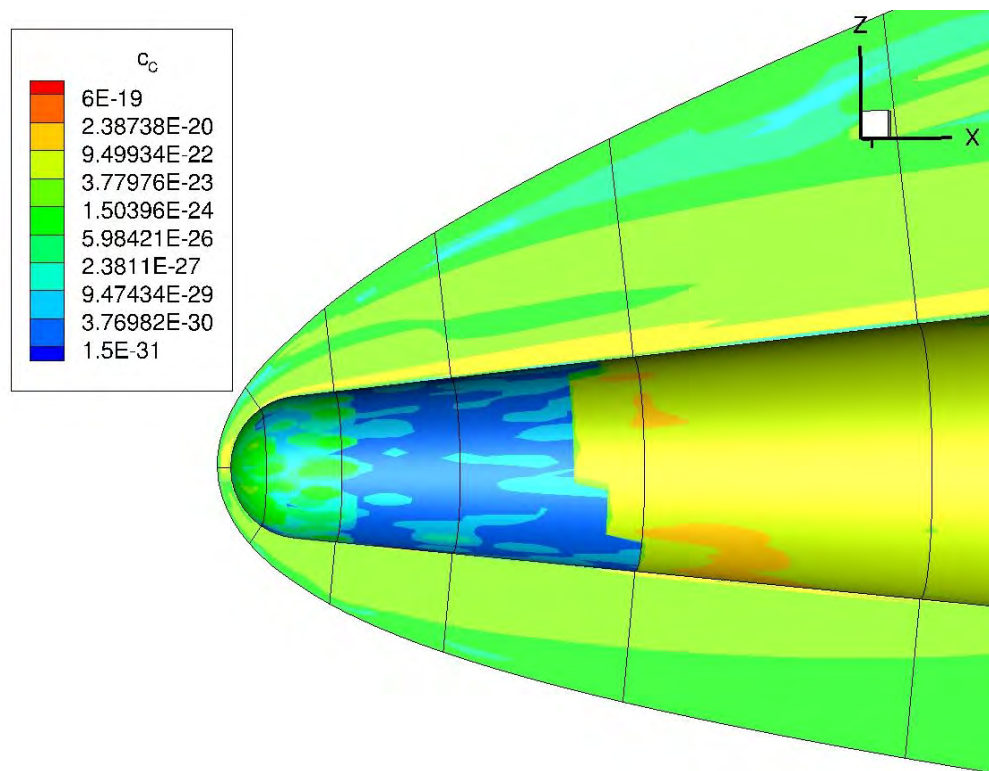Figure 115. Mass Fraction of Monatomic Carbon throughout the Flowfield

Figure 116. Mass Fraction of Monatomic Carbon at the Nose
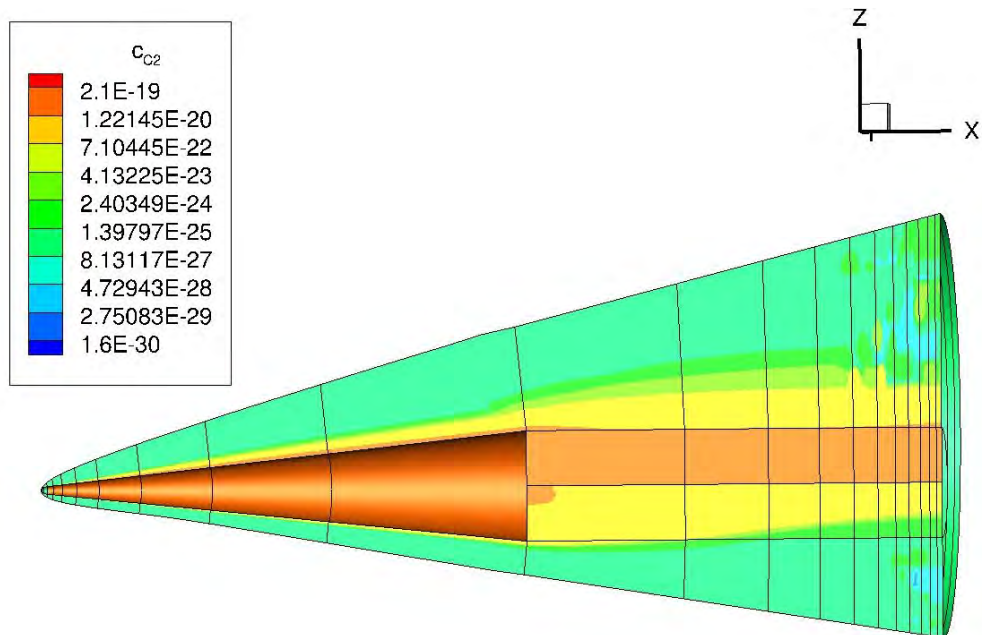
Figure 117. Mass Fraction of Diatomic Carbon throughout the Flowfield
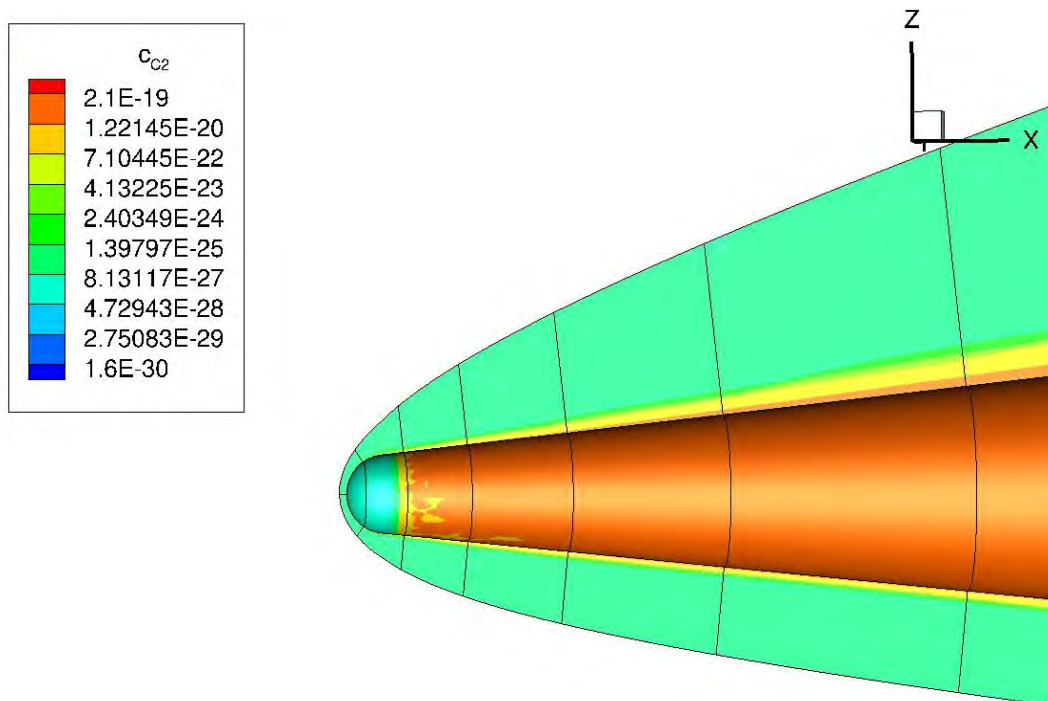
Figure 118. Mass Fraction of Diatomic Carbon at the Nose

129
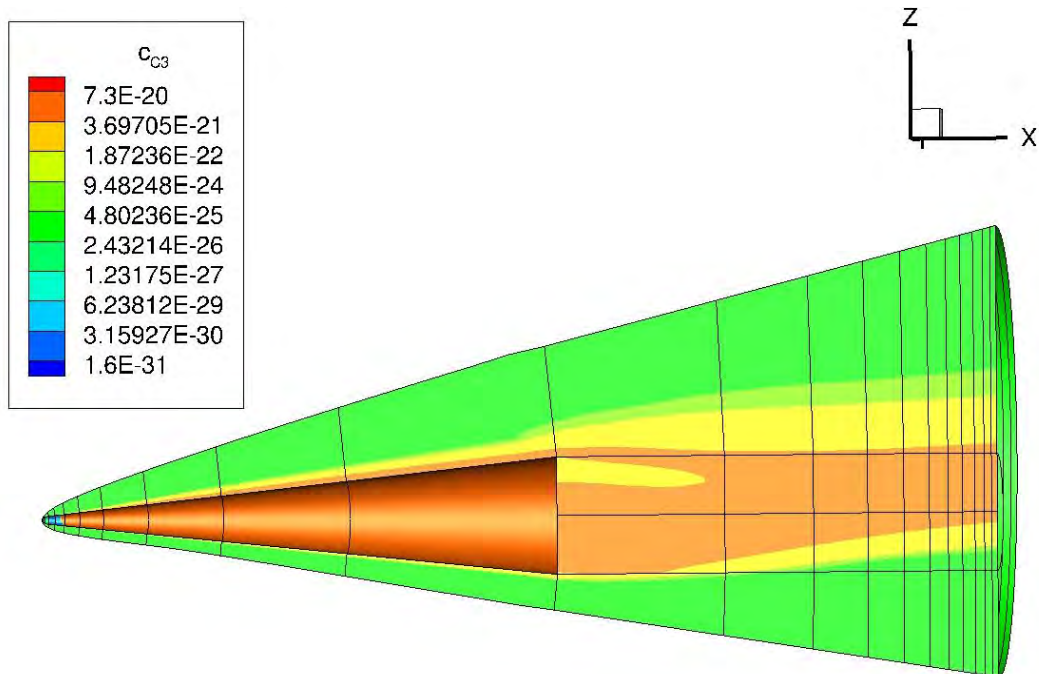
Figure 119. Mass Fraction of Triatomic Carbon throughout the Flowfield
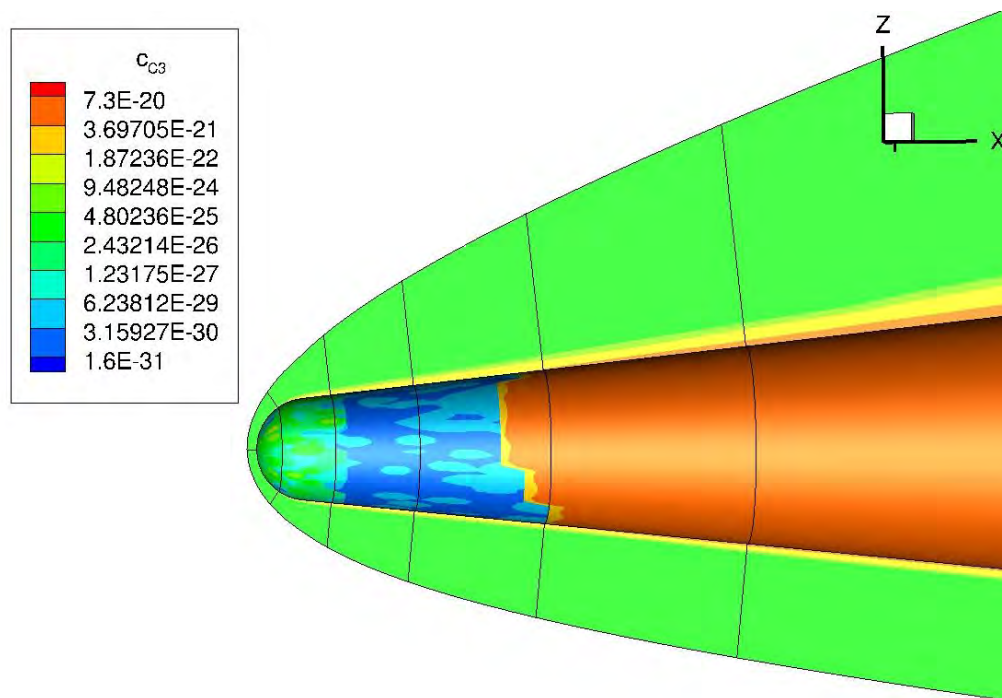
Figure 120. Mass Fraction of Triatomic Carbon at the Nose

Figure 121 and Figure 122 depict the concentration of Cyanide throughout the flowfield. The highest concentration of Cyanide is at the nose where temperatures where hot enough to facilitate on the formation of Monatomic Carbon and Nitrogen. While the wake concentration is higher than the flowfield concentration it was determined these concentrations were too low for detection.
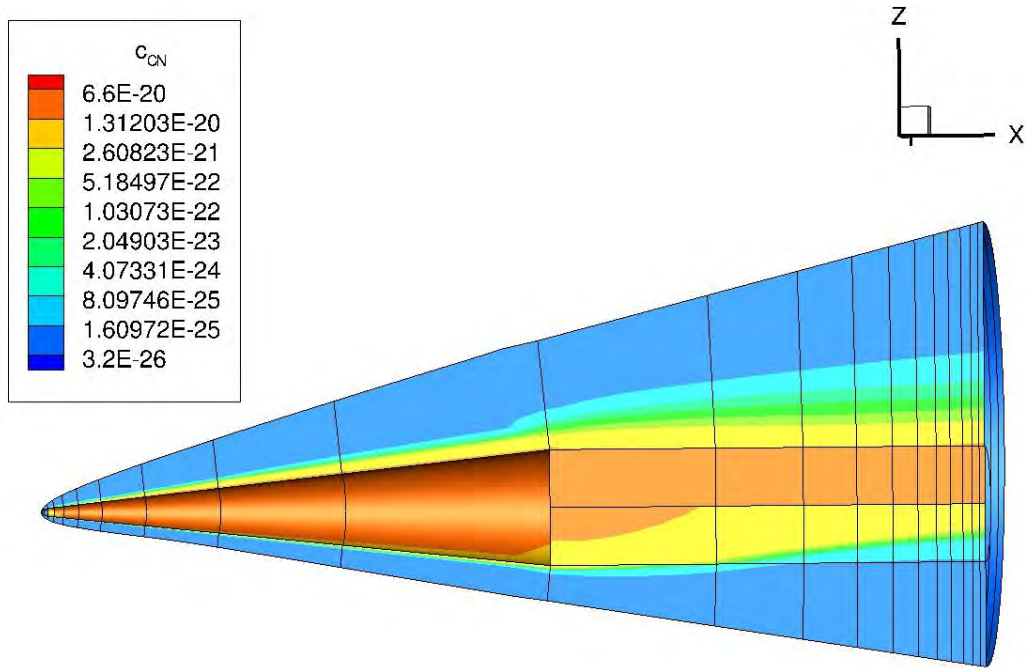
Figure 121. Mass Fraction of Cyanide throughout the Flowfield
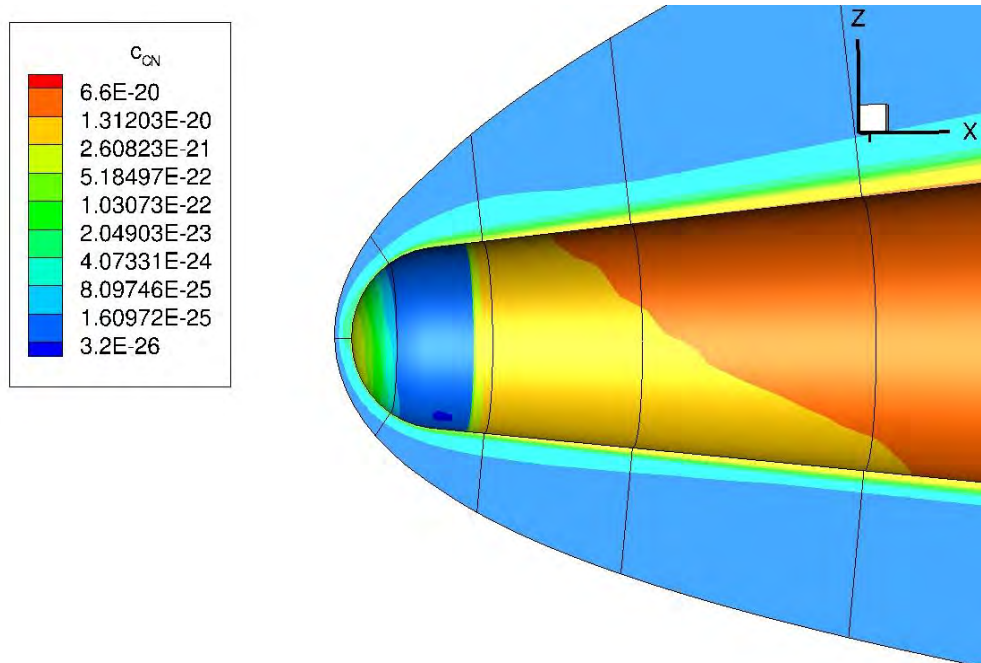
Figure 122. Mass Fraction of Cyanide at the Nose

Bibliography

[1] J. Cirincione, "Brief History of Ballisitc Missile Defense and Current Programs in the United States," 1 February 2000. [Online]. Available: http://carnegieendowment.org/2000/02/01/brief-history-of-ballistic-missile-defense-and-current-programs-in-united-states. [Accessed 30 September 2014].

[2] Oxford Dictionaries, "Oxford Dictionary: Language Matters - Ballistic Missile," Oxford University Press, 2014. [Online]. Available: http://www.oxforddictionaries.com/us/definition/american_english/ballistic-missile. [Accessed 16 October 2014].

[3] J. Gibson and K. Kemmerly, "Interconintental Ballisitc Missiles," in *AU-18 Space Primer: Air Command and Staff College Space Research Electives Seminars*, Maxwell Airforce Base, Air University Press, 2009, pp. 235-247.

[4] National Air and Space Intelligence Center, "Ballistic and Cruise Missile Threat," Wright-Patterson Air Force Base, 2009.

[5] George C. Marchall Institute, "The Stages of a Ballistic Missile's Flight," [Online]. Available: http://missilethreat.com/the-stages-of-a-ballistic-missiles-flight/. [Accessed 16 October 2014].

[6] G. N. Lewis and P. T. A., "Future Challanges to Ballistic Missile Defense," *IEEE Spectrum,* no. September, pp. 60-68, 1997.

[7] J. Novak, "Strouhal Number of a Prism as a Function of the Number of Edges and Strouhal Number of a Cone," *Acta Technica CSAV,* vol. 20, no. 5, pp. 556-563, 1975.

[8] A. Roshko, "Experiments on the Flow Past a Circular Cylinder at Very High Reynolds Number," California Institute of Techology, Pasadena, California, 1960.

[9] J. D. Anderson, Hypersonic and High-Temperature Gas Dynamics Second Edition, Reston, VA: American Institute of Aeronatuics and Astronautics, 2006.

[10] J. D. Anderson, Modern Compressible Flow Third Edition, New York, NY: McGraw-Hill, 2003.

[11] P. A. Gnoffo, "Computational Fluid Dynamics Technology for Hypersonic Applications," NASA Langle Research Center, Hampton, VA.

[12] J. D. Anderson, Computational Fluid Dynamics: The Basics with Applications, New York: McGraw-Hill, 1995.

[13] R. A. Thompson and P. A. Gnoffo, "Application of the LAURA Code for Slender-Vehicle Aerothermodynamics," *Journal of Spacecraft and Rockets,* vol. 29, no. 1, pp. 16-23, 1992.

[14] C. J. Riley and F. M. Cheatwood, "Distributed-Memory Computing With the Langley Aerothermodynamic Upwind Relaxation Algorithm," in *4th NASA National Symposium on Lage-Scale Analysis and Design on High-Performance Computers and Workstations*, Williamsburgh, VA, 1997.

[15] P. A. Gnoffo, "Upwind-Biased, Point-Implicit Relaxation Startegies for Viscous, Hypersonic Flows," NASA Langley Research Center, Hampton, VA, 1989.

[16] C. Park, Nonequilibrium Hypersonic Aerothermodynamics, Washington, D.C.: John Wiley & Sons, Inc., 1990.

[17] A. Mazaheri, P. Gnoffo, C. Johnston and B. Kleb, LAURA Users Manual: 5.5-65135, Hampton, VA: Langley Research Center, 2013.

[18] R. MacDermott, "An Aerothermal Analysis of Maneuverable Reentry Vehicle," Air Force Institute of Technology, Wright-Patterson AFB, OH, February 2012 (Limited Distrobution).

[19] M. Satchell, "Air Radiation Modeling for Hypersonic Vehicles," Air Force Institute of Technology (AU), Wright-Patterson AFB, OH, February 2013 (Limited Distrobution).

[20] D. C. Wilcox, "Formulation of the k-ω Turbulence Model Revisited," *AIAA Journal,* vol. 46, no. 11, pp. 2823-2838, 2008.

[21] F. M. Cheatwood and R. A. Thompson, "The Addition of Algebraic Turbulence Modeling to Program LAURA," Langley Research Center, Hampton, VA, April 1993.

[22] B. Wilkerson III, "Development of Air Radiation Modeling for Hypersonic Vehicles," Air Force Institute of Technology (AU), Wright-Patterson AFB, OH, September 2012 (Limited Distrobution).

[23] C. O. Johnston, P. A. Gnoffo and A. Mazaheri, "A Study of Ablation-Flowfield Coupling Releveant to the Orion Heatsheild," 22 June 2009. [Online]. Available: http://ntrs.nasa.gov/archive/nasa/casi.ntrs.nasa.gov/20090025449.pdf. [Accessed 25 June 2015].

REPORT DOCUMENTATION PAGE			*Form Approved* *OMB No. 0704–0188*		
The public reporting burden for this collection of information is estimated to average 1 hour per response, including the time for reviewing instructions, searching existing data sources, gathering and maintaining the data needed, and completing and reviewing the collection of information. Send comments regarding this burden estimate or any other aspect of this collection of information, including suggestions for reducing this burden to Department of Defense, Washington Headquarters Services, Directorate for Information Operations and Reports (0704–0188), 1215 Jefferson Davis Highway, Suite 1204, Arlington, VA 22202–4302. Respondents should be aware that notwithstanding any other provision of law, no person shall be subject to any penalty for failing to comply with a collection of information if it does not display a currently valid OMB control number. PLEASE DO NOT RETURN YOUR FORM TO THE ABOVE ADDRESS.					
1. REPORT DATE (DD–MM–YYYY) 17-10-2015		2. REPORT TYPE Master's Thesis		3. DATES COVERED (From — To) September 2013-Spetember 2015	
4. TITLE AND SUBTITLE Analysis of Hypersonic Vehicle Wakes			5a. CONTRACT NUMBER		
			5b. GRANT NUMBER		
			5c. PROGRAM ELEMENT NUMBER		
6. AUTHOR(S) Kania, Matthew A. LT, USN			5d. PROJECT NUMBER		
			5e. TASK NUMBER		
			5f. WORK UNIT NUMBER		
7. PERFORMING ORGANIZATION NAME(S) AND ADDRESS(ES) Air Force Institute of Technology Graduate School of 2950 Hobson Way WPAFB OH 45433-7765			8. PERFORMING ORGANIZATION REPORT NUMBER AFIT-ENY-15-S-063		
9. SPONSORING / MONITORING AGENCY NAME(S) AND ADDRESS(ES) National Air and Space Intelligence Center Allison Schauer Bldg 859, Area A 4180 Watson Way. Wright-Patterson AFB, OH 45433. allison.schauer@us.af.mil			10. SPONSOR/MONITOR'S ACRONYM(S) NASIC/GSPM		
			11. SPONSOR/MONITOR'S REPORT NUMBER(S)		
12. DISTRIBUTION / AVAILABILITY STATEMENT DISTRIBUTION STATEMENT A. APPROVED FOR PUBLIC RELEASE; DISTRIBUTION UNLIMITED.					
13. SUPPLEMENTARY NOTES This work is declared a work of the U.S. Government and is not subject to copyright protection in the United States.					

14. ABSTRACT
        As advancements are made with ballistic missiles, particularly in the area of hypersonic bodies, there is a growing need to advance the methods of tracking these new ballistic weapons. As a result, the National Air and Space Intelligence Center has asked the Air Force Institute of Technology to examine the wake region behind hypersonic bodies. A thorough understanding of the aerothermal phenomena and the chemical reactions occurring in the wake region will enable an advancement of tracking hypersonic bodies. This research examined the wake region behind a hypersonic body using computational fluid dynamics.
        This study used Pointwise® to develop a three-dimensional grid of the flowfield around a conic hypersonic body and extending into the wake region. The Langley Aerothermodynamic Upwind Relaxation Algorithm was used to solve the flowfield, including the wake, and all surface properties. The results from the simulation were used to characterize the wake region behind the hypersonic body and compare that to the flowfield surrounding the body.
        Although no flight test data was available and no published results could be found in this area of interest, the results had good agreement with previous hypersonic aerodynamic wake studies. Along with that, several interesting phenomena were discovered dealing with the aerothermal environment and chemical species present in the wake that could lead to advancements in the efforts of tracking hypersonic bodies.					

15. SUBJECT TERMS Hypersonic, Wake, Missiles, Tracking, Signatures					

16. SECURITY CLASSIFICATION OF:			17. LIMITATION OF ABSTRACT	18. NUMBER OF PAGES	19a. NAME OF RESPONSIBLE PERSON Dr. Robert Greendyke
a. REPORT U	b. ABSTRACT U	c. THIS PAGE U	UU	153	19b. TELEPHONE NUMBER (Include Area Code) (937)255-4567 Robert.greendyke@afit.edu

135